ABSTRACT

Title of Document: THE HILBERT-HUANG TRANSFORM FOR DAMAGE DETECTION IN PLATE STRUCTURES

Arnaud I. Zemmour, Master of Science, 2006

Directed By: Professor Darryll Pines
Department of Aerospace Engineering

This thesis investigates the detection of structural damage in plate structures using the empirical mode decomposition method along with the Hilbert spectral analysis. In recent years there have been an extensive amount of research associated with the development of health monitoring methods for aerospace systems, such as aging aircraft and Health and Usage Monitoring Systems (HUMS) for rotorcraft. The method developed here exploits a new time-frequency signal processing analysis tool, the Hilbert-Huang transform, along with the Lamb wave propagation for thin plates. With the use of the wave reflections from discontinuities, damage identification methods were developed to determine the presence, location and extent of damage in isotropic and composite plate structures.

The ability of the empirical mode decomposition to extract embedded oscillations, to reveal hidden reflections in the data and to provide a high-resolution energy-time-frequency spectrum is used to describe the Lamb waves interactions with various damaged regions.

THE HILBERT-HUANG TRANSFORM FOR DAMAGE DETECTION IN PLATE STRUCTURES

By

Arnaud I. Zemmour

Thesis submitted to the Faculty of the Graduate School of the
University of Maryland, College Park, in partial fulfillment
of the requirements for the degree of
Master of Science
2006

Advisory Committee:
Professor Darryll Pines, Chair
Professor Sung Lee
Professor Norman Wereley

Dedication

To my parents and my brother Nicolas

Acknowledgements

First of all, I would like to express my thanks to my advisor, Dr Darryll Pines, for his support, instruction, patience and precious insights. I am also indebted to my “second advisor”, Dr Ashish Purekar, for all his advices and technical assistance. I could not have accomplished this work without his help. I would like to acknowledge my family members for their endless love, support and understanding. I am also very grateful to all my friends with a special mention to Julie and Salim for their friendship and support overseas. Last but not least, I would like to thank my fellow aerospace friend, Maxime Ransan, for making these two years at the University of Maryland a wonderful and unforgettable experience.

Table of Contents

List of Tables

List of Figures

Chapter 1
Introduction

1.1 Motivation

Structural Health Monitoring (SHM) and continuous on-line monitoring of structural integrity are of primary concern in many engineering field as aerospace, automotive, large civil structures and other industrial applications [1]. The replacement of present day manual inspection techniques with more advanced sensitive and automatic health monitoring system would substantially reduce the maintenance and the related life-cycle costs of these structures. Considerable research effort in that direction are being made in universities, research centers and corporations all around the world. Currently, the health monitoring of aircraft structures is conducted off-line and techniques such as ultrasonic inspection, acoustic emission, C-scan or X-rays are commonly used. These techniques do not provide early warning for preventive maintenance of the structures and lead to increased operation and maintenance costs. Hence, it is highly desirable to have a means of continuously monitoring the integrity of the structure in order to improve performance and reduce costs. The introduction and the significant use of composite materials has increased the need of a robust in-situ health monitoring system. While in-service inspection of metallic structures requires mostly the detection of fatigue cracks and corrosion, composites structures require the detection accidental damage such as delaminations and impact damage.

The situation suggests that different health monitoring philosophies should be applied to the two different families of structural components.

A real time in-situ monitoring of a structure suggests the use of smart sensors and actuators. Adaptive material solutions to structural health and usage monitoring relates to systems including smart sensors for damage detection combined with advanced signal processing method. The use of small and conformable transducers that could continuously interrogate the structure is mandatory for an online monitoring system. Various sensor technologies such as optical fiber sensors or piezoelectric sensors are currently available and can be integrated into a structure to be monitored. Recently, piezoelectric materials have become available in the form of ceramic elements that can also become an integral part of a monitored structure. The sensor technology and the associated signal analysis and interpretation algorithm is the key factor in the development of a successful health monitoring solution. The key to reliable and high-resolution damage detection is a good signal interpretation. Signal processing and computation are crucial elements in the implementation and operation of any damage detection system. This system requires the availability of appropriate signal processing technology to extract features from different types of sensors and translate this information into a diagnosis of location and severity of damage [2].

1.2 Structural Health Monitoring Overview

1.2.1 Challenge and Goals of Structural Health Monitoring

Structural Health Monitoring (SHM) involves real-time monitoring of structures by means of sensors embedded or mounted externally to the structure. Speckmann [4] introduced the idea of SHM as a system similar to the human nervous system as described in the Figure 1.1. The human body actually contains sensors (that are the nerves), which inform the brain (SHM system) of the intensity of the pain. Actions such as going to the doctor or take medicine can therefore be taken. In the case of an aircraft, the sensors must be right at the place where an area is to be monitored to ensure the structural integrity. In case of damage, the sensors directly identify the location and possible preventive actions be taken.

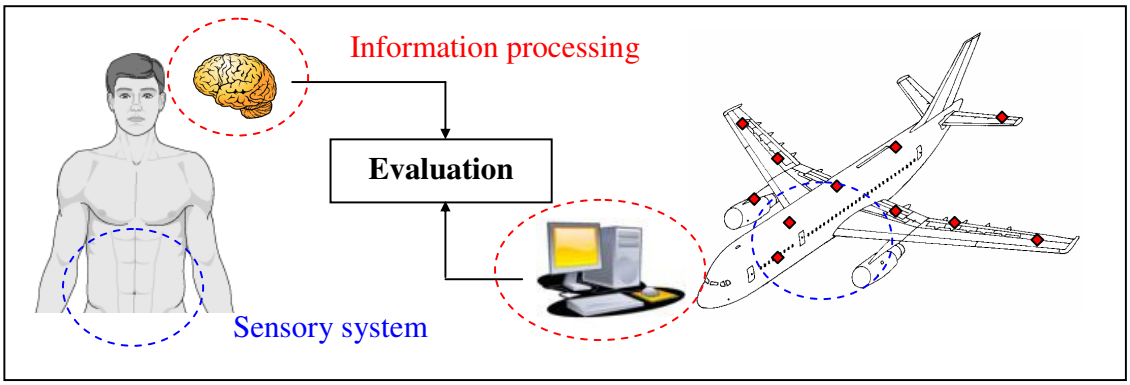

Figure 1.1: Idea of a structural health monitoring system

Continuous on-line monitoring of structural integrity are of primary concern in many engineering field as aerospace, automotive, large civil structures and other industrial applications. Of all these possible applications, the aerospace industry has one of the

highest payoffs. Indeed damage can lead to catastrophic failures and costly inspections. The continued growth in air traffic has therefore placed an increasing demand on the aerospace industry to manufacture aircraft at lower costs, while ensuring that products are sure, efficient and friendly to the environment. New large capacity aircraft are being developed and will be used widely in the future. Many of these structures will make greater use of composite materials. For instance the new Boeing 7E7 will be built with 50% of composites materials whereas the world's largest aircraft, the Airbus A380 is composed of 25% of composites materials and 22% of carbon fiber reinforced plastic [5]. At the same time the current aircraft fleet is ageing continually. All these developments represent a major challenge to inspection and maintenance.

1.2.2 Safety Issue

Maintenance and continuous health monitoring of air, land and sea structures is one of the most important concerns in many industries including transportation and civil engineering. In high performance transportation such as aerospace, high-speed trains and also automobiles, where structural failures may lead to fatal accidents, safety of operation is a prime consideration. Cracks in metallics and impact damage in composite materials are the major cause of failure in aerospace structures. To ensure structural integrity and hence maintain safety, in-service health and usage monitoring techniques must be employed. In this context structural health monitoring is used to ensure safe and reliable systems.

1.2.3 Cost Issue

Structural repairs increase the cost of transportation in at least two ways. First, the design and implementation of repairs implies direct costs. Second, the execution of repairs generally requires the transportation system to be temporarily taken out of service and this induces indirect costs due to the loss of production volume or as a result of leasing a substitute system. To reduce repair and maintenance costs an attempt to repair can be undertaken at a very early stage of damage development to limit direct costs. Alternatively, it might be decided to postpone repair until the transportation system has to be taken out of service for scheduled major overhauls to reduce indirect costs. In this context structural health monitoring becomes an issue of cost savings [6]. A recent study on inspection requirements for a modem fighter aircraft (featuring both metal and composite structure) revealed that an estimated 40% plus could be saved on inspection time by utilizing smart monitoring systems. More than 70 millions hours per year, equivalent to US$ 10.5 billion, is invested in civil aircraft maintenance. A typical Boeing 747 aircraft is inspected every 12 to 17 months specifically for signs of fatigue damage [6].

1.2.4 Performance Issue

Different types of damage (cracks, corrosion or delaminations) can be found thanks to appropriate inspection technique. The established inspection techniques vary from visual inspection by the naked eye to passing the structure through a fully automated inspection gantry. In an indirect approach structural performance or rather structural behavior is measured and compared with the supposedly known global response characteristics of the undamaged structure.

Obviously in both the direct and indirect approaches the sensitivity and the reliability of inspection are important quantitative performance measures. They are determined on the one hand by the laws of physics but on the other in practice also by the hardware and software quality of the inspection equipment, and last but not least, by the equipment operator: the inspector. In this connection human factors such as the loss of alertness in case of rare occurrences of damage and inspector fatigue in case of long and tedious inspections are important reasons to consider an autonomous solution to inspection as an element of structural health monitoring [6]. The replacement of present day manual inspection techniques with more advanced sensitive and automatic health monitoring system would reduce substantially the maintenance and the related life-cycle costs of these structures. Thus, the basic approach is to make non-destructive testing technology an integral part of the aircraft structure itself. By using an in-situ structural health monitoring system to continuously monitor the structure, components would remain in operation without regularly scheduled maintenance until the SHM system reported that damage was present and a repair was necessary.

1.2.5 Summary

Safety, life-cycle costs and performance issues are key drivers that motivate an integrated vehicle health management solution for aircraft systems.

The attractive potential of autonomous monitoring systems arises from a number of elements such as: reduced life cycle costs, reduced inspection/maintenance effort, improved performance, improved high rate operator availability, extended life of structures and improved safety. This leads to more efficient and economically

attractive aircraft. All these elements are important to both manufacturers and operators of civil and military aircrafts.

1.3 Signal Processing in SHM

In general, the development of successful health monitoring methods depends on two key factors: sensor technology and the associated signal analysis and interpretation algorithms. Intelligent signal processing is the key element, which builds the bridge between the sensor signal and the structural integrity interpretation [7]. There are a number of intelligent signal processing methods available for damage detection which could be integrated with aircraft structures and play an important role in aircraft maintenance. The past fifteen years have led to the development of numerous techniques such as Neural Networks, Genetic Algorithms and Time-Frequency methods.

1.3.1 Signal Processing

Processing a signal consists of extracting important feature from sensors measurements to reach a desire goal. For instance, if we are interested in reducing the noise in a signal, the best representation would be the one in which the signal and the noise are separated. The signal processing covers a lot of different applications: each time one uses a sensor to measure data, one has to process the corresponding signal. A relatively common diagram describing a signal processing system is given in the Figure 1.2.

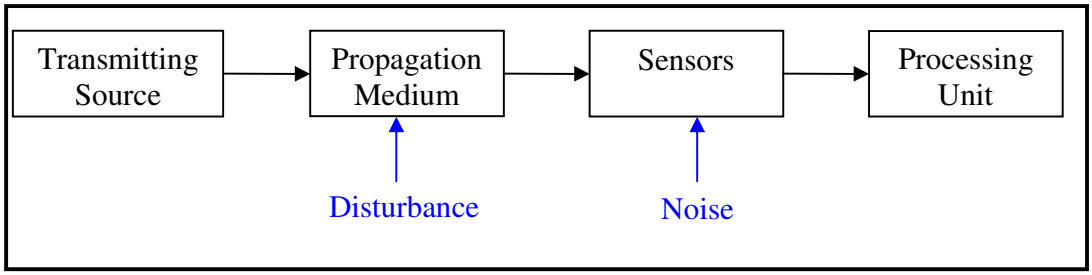

Figure 1.2: A common signal processing system

The sensors translate a physical phenomenon from one or many sources in temporal variations or in spatial variations. These sources are emitting signals which can transmit through a medium in the form of a wave (electromagnetic, acoustic, etc...). These waves, containing the source information, can be disturbed, spread out in time, delayed, reflected, etc…

Moreover, sensed signals are often polluted by measurement noise. This noise makes the signal much more complicated to analyze. Therefore, the complexity of the physical phenomenon along with the disturbances due to the propagating medium and the noise due to the measurement devices do not allow the extraction of the most useful data. Thus, signal processing consists of transforming a signal in a certain manner in order to get specified information. Various linear and nonlinear transforms are used in practice. In particular, the Fourier transform, the Short-Time-Fourier transform, the Wigner-Ville distribution and the Wavelet transforms has been widely used in structural health monitoring.

1.3.2 Spectral Analysis

Any observed signals, as acquired from measuring sensors in raw form, are in the time-domain. The history of the spectral analysis and time-frequency analysis began with the introduction of the Fourier transform by the French physicist Joseph Fourier

[8] in 1807, defined as $X(f) = \int_{-\infty}^{+\infty} x(t)e^{2\pi ift}dt$. The squared modulus of the Fourier transform, the power spectrum, gives an indication about the energy content of the analyzed signal. Historically, Fourier spectral analysis has provided a general method for examining the global energy-frequency distributions and has been used for damage detection. Melhem, et. al. [9] showed that the Fourier transform can detect the progression of an impact damage in a beam. Nag, et. al. [10] created a spectral finite element model based on the fast Fourier transform to simulate a composite beam with a delamination. The analysis efficiently identified the severity of delaminated configurations through a damage force indicator. Lee, et. al. [11] examined the power spectrum of a Lamb wave signal and observed fluctuations in the dominant frequency due to damage. Loewke, et. al. [12] showed that the 2D FFT can be a useful tool in revealing the relative magnitudes of different spatial wavelengths of a signal in a material. Alleyne, et. al. [13] also examined the 2D FFT and performed both experimental and numerical investigations to show the Lamb wave interactions with defects. The Fourier transform is very useful in many applications, but it had to be modified in order to get information not only in the frequency domain but also in the time domain.

1.3.3 Short-Time Fourier Transform (STFT)

The Hungarian-British 1971 Nobel Prize in physics, Dennis Gabor, first recognized the great importance of localized time and frequency concentrations in signal processing [14]. In order to incorporate both time and frequency localization properties in one single transform function, Gabor introduced the windowed Fourier

transform by using a Gaussian distribution function as a window function. The idea is to use a window function in order to localize the Fourier transform, then shift the window to another position, and so on. The result of this transform would be displayed in a time-frequency representation, commonly referred to as a spectrogram. Ihn, et. al. [15] computed the spectrogram provided by the STFT to select an individual mode for damage detection and maximize signal to noise ratio in sensor signals. A reassigned spectrogram is used by Valle, et. al. [16] to characterize the modal and frequency content of a single ultrasonic signal as a function of time, enabling a procedure to locate flaws in an aluminum plate specimen. Kim, et. al. [17] used the STFT to decompose the piezoelectric sensor signals due to a low-velocity impact damage in composite laminates. The need to describe more accurately non-stationary signals and the poor time-frequency resolution of the STFT pushed the scientists to research a new method able to overcome these drawbacks.

1.3.4 Wavelet Transform

In 1982, Jean Morlet, a French geophysical engineer, discovered the idea of the wavelet transform, providing a new mathematical tool for seismic wave analysis. Morlet first introduced the idea of wavelets as a family of functions constructed from translations and dilatations of a single function called the “mother wavelet”. A lot of researchers (Grossmann, Meyer, Mallat, Daubechies, etc…) developed and enhanced this new signal-processing tool to make it the most efficient and used technique in the structural health-monitoring field. The Wavelet analysis has been one of the most important and fastest evolving mathematical and signal processing tools of the last twenty years. There has been a considerable amount of papers dealing with the use of

Wavelet transform in structural health monitoring. Wait, et. al. [18] used the Morlet wavelet transform to gain insight as to how the intensities of the signal input energy have been shed into sideband frequencies as a result of damage in a composite plate. A damage index relating the ratio of the test signal's kinetic energy to that of the baseline signal was then computed. Paget, et. al. [19] examined the amplitude change of the wavelet coefficients to successfully characterize the interactions of the Lamb waves with damage in a plate. Kessler, et. al. [20] plotted the magnitude of the wavelet coefficient at the peak driving frequency and compared the remaining energy from the input signal for both undamaged and damaged cases of simple structures. Kim, et. al. [21] explored the change of modal properties caused by a damage in a beam structure, which results in the variation of the wavelet coefficients. Lemistre, et. al. [22] used the wavelet transform to extract the shearing mode due to a delamination in a composite plate and then to localize damage with a good accuracy. Ip, et. al. [23] measured the arrivals times of reflected waves from the wavelet coefficients plots to infer the distance of the delamination from the sensor in composite beams. Salehian, et. al. [24] implemented the same analysis on an isotropic aluminum plate and an anisotropic composite plate. Silva, et. al. [25] used the wavelet transform to detect hidden corrosion on the surface of aluminum panel. Wavelet analysis was used to determine the wave speed that is affected by corrosion in the material. Quek, et. al. [26] explored the wavelet transform of dynamic response data as a local non-destructive evaluation technique for locating damage in a beam. Okafor, et. al. [27] observed that the magnitude of the wavelet coefficient at the location of damage increased linearly with the increase in the amount of damage. A review of structural

health monitoring literature from 1996 to 2001 [28] yields more examples of the use of the wavelet transform for damage detection in structures. Despite its extensive use, the wavelet transform suffers of its non-adaptive nature. Once the wavelet basis function is selected, data is correlated with different dilated and scaled versions of their fundamental basis function.

1.3.5 Hilbert-Huang Transform (HHT)

Huang, et. al. [29] introduced a new adaptive method for nonlinear and non-stationary data analysis in 1998. This method consists of the combination of the empirical mode decomposition associated with the Hilbert spectral analysis. Lin, et. al. [30] showed that the Hilbert-Huang Transform can be used to identify the structural parameters of a benchmark building and is quite accurate in detecting structural damage locations and severities. Quek, et. al. [31] illustrated the suitability of the HHT for damage detection problems, such as an aluminum beam with a crack, a sandwiched aluminum beam with an internal delamination, a reinforced concrete slab with different degrees of damage. Crack and delamination in homogeneous beams can be located accurately and damage in the reinforced concrete slab can be identified if it has been previously loaded beyond first crack. Tua, et. al. [32] used the energy peaks in the Hilbert spectrum corresponding to crack-reflected waves to determine accurate flight times and also to estimate the orientation of the crack. Yang, et. al. [33] proposed two damage detection techniques based on the HHT. The first method, based on the empirical mode decomposition (EMD) extracted damage spikes due to a sudden change whereas the second one, based on the EMD and the Hilbert transform was capable of determining the damage time instants and determining the natural

frequencies and damping ratios of the structure before and after damage. Salvino and Pines [34] showed the ability of the empirical mode decomposition to extract phase information from transient signals and use the results to infer damage in a structure. Jha, et. al. [35] investigated the HHT to a multi-level structure. They showed that discontinuity in the IMFs indicated the presence and location of a damaging event in a structure monitored continuously. Bernal, et. al. [36] examined the instantaneous frequency of the intrinsic mode functions (IMF) provided by the EMD as a damage detection tool. Yu, et. al. [37] proposed a method for the fault diagnosis of roller bearings based on the HHT. The local Hilbert marginal spectrum is used to diagnose the faults in a roller bearing and to identify fault patterns.

The HHT is going to become the most used intelligent signal processing for in-situ monitoring of structures in the next few years. The Wavelet transform is still used by some researchers but the HHT offers a huge potential for analyzing non-stationary and nonlinear data. Quek, et. al. [38] compared the results obtained from the wavelet analysis in a previous paper with results from an empirical mode decomposition. The empirical mode decomposition was shown to provide a more direct method of extracting information needed for damage detection purposes.

1.4 Present Study

To increase the safety, affordability and sustainability of long-term exploration missions, diagnosis and prognosis for Integrated Systems Health Management of complex mission-critical spacecraft structures is essential. Currently, there is no comprehensive approach monitoring the health of critical spacecraft structures using in-situ sensors and actuators. Past efforts have involved limited sensing of spacecraft structural components with insufficient data to diagnose the presence, type and extent of structural damage. This project aims to develop robust diagnostic metrics to infer damage presence, type and location through new time frequency signal processing analysis tools.

The Acousto-Ultrasonic approach with in-situ transducers developed by Purekar [39] has shown promising results for wave propagation in thin plates and damage detection. The same approach is followed in this work. The Acousto-ultrasonic technique is based on stress waves introduced into a structure by a probe at one point and sensed by another probe at a different position. The pitch-catch method, which consists of a transducer used to send out an interrogating signal and transducers located at different positions to monitor the dynamics of the plate, is used in the present work and shown in the Figure 1.3. The Lamb waves are excited through a piezoceramic actuator and the response is gathered with an array of sensors. Multi-sensors architectures improves signal to noise ratio and offer better robustness and reliability. Purekar, et. al. [40] used the array of sensor as a directional filter to look in different directions in a plate.

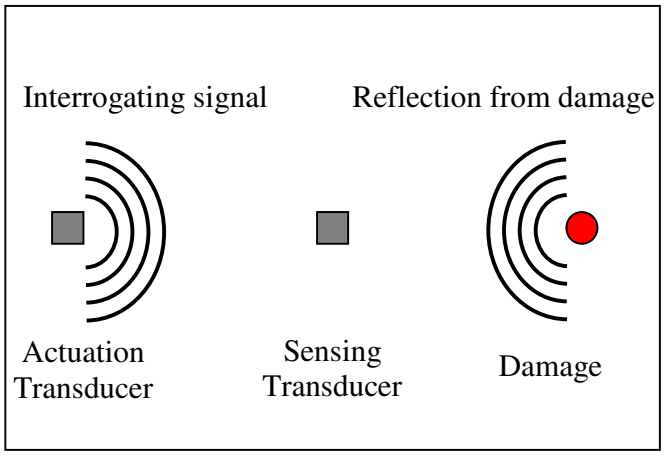

Figure 1.3: Pitch-catch damage detection method

Since Acousto-ultrasonic produce transient signals, a way of interpreting the results needs to be devised. Several methods have been proposed to enhance the interpretation of the measured Lamb wave signals to detect and locate structural damage. They are based on changes in wave attenuations using wavelets, time frequency analysis, wave reflections, and time of arrival information. As mentioned previously, many time-frequency methods have been applied to structural health monitoring methods. The Short-time Fourier Transform and the Wavelet transform are the most commonly used time-frequency analysis tools in the damage detection field. In this work the Hilbert-Huang transform is examined as a damage detection tool. This work demonstrates that the use of empirical mode decomposition coupled with Hilbert spectral analysis is an effective tool for locating damage in a two dimensional structure.

1.5 Organization of the thesis

This thesis explores the use of the empirical mode decomposition along with the Hilbert spectral analysis for damage detection in isotropic and composite plate structures. The primary objective of this research is the implementation of the Hilbert-Huang transform and the investigation of its potential use for damage detection purposes.

A review of the most commonly used time-frequency methods in structural health monitoring is presented in Chapter 2. The Short-time Fourier transform, the Wigner-Ville distribution and the Wavelet transform are described and illustrated through examples to better understand the physics under these transforms. The Chapter 3 details the empirical mode decomposition algorithm and the associated Hilbert spectral analysis. The different issues encountered during the implementation of the method are also discussed. The end of the chapter is dedicated to a comparison of the Hilbert-Huang transform with the time-frequency methods reviewed in Chapter 2.

The investigation of the different potential features that could be used to obtain robust and efficient metrics for damage detection is shown in Chapter 4. A one dimensional finite element model is created and simulated in order to examine the Hilbert phase as a damage detection parameter. Both energy and time resolutions are also explored to give information about the location and the severity of damage. The different metrics developed in Chapter 4 are applied to the damage detection of

isotropic plate structures in Chapter 5. The HHT shows the ability to reveal hidden reflections in data and to quantify the growth of the defect in the case of an aluminum plate with holes. Chapter 6 is dedicated to the damage detection in composite plates. Delaminations, local stiffness changes and low-velocity impact are experimented and processed. The results of the damage metrics on these data are then discussed. Concluding thoughts, including contributions and limitations of the current work and possible future directions for research are highlighted in Chapter 7.

Chapter 2

Time-Frequency Methods For Damage Detection

A transient time-domain signal, together with its Fourier transformed spectrum, does not provide enough information for applications that require an understanding of how a signal's frequency changes as a function of time. The Fourier transform is limited to stationary signals, signals that have the same frequency content for all times. In contrast, nonstationary signals require signal-processing methods that can quantitatively resolve changes in frequency content, as a function of time.

The field of time-frequency signal analysis is one of the recent developments, which provides suitable tools for analyzing nonstationary signals occurring in many fields of engineering, such as telecommunications, vibration analysis, and biomedicine. Ville [41] notes that there are two basic approaches to time-frequency analysis. The first is to divide the signal into slices in time and to analyze the frequency content of each of these slices separately. The second approach is to first filter the signal at different frequency bands and then cut the frequency bands into slices in time to analyze their energy content as a function of time and frequency. The first approach is the basic Short-Time Fourier Transform, also known as spectrogram, and the second one is the Wigner-Ville Transform. Other time-frequency analysis techniques include, but are not limited to, wavelet analysis and empirical mode decomposition combined with the Hilbert spectral analysis.

This chapter briefly reviews the time-frequency methods discussed above except for the empirical mode decomposition, which will be described in detail in the next chapter.

2.1 Short-Time Fourier Transform (STFT)

2.1.1 Description of The Method

When the spectral content of the signal changes in time, neither the time nor the frequency-domain is sufficient to accurately describe the signal properties. Many attempts have been made to overcome this drawback. The analysis in both time and frequency domains using the so-called windowed Fourier transform is the first important development. This analysis makes use of a window function. The idea of the windowed Fourier transform is to analyze the frequency content of a signal within a window that is fixed in size and moves with time along the signal, as depicted in Figure 2.1. Effectively the signal is divided into segments before Fourier analysis is applied. The signal is assumed to be stationary within each segment. Different positions of the window cover the whole time domain. Thus, the windowed signal $x_w(t)$ encodes the window position τ and time t. If the Fourier transform is applied to such a signal the result is a new signal representation $F(t, f)$ that in fact is a function of time and frequency. This analysis leads to the short-time Fourier transform. The biggest limitation of this approach is the comparison between the time and frequency resolution of the analysis. Good time resolution implies a small time window, which results in a poor frequency resolution and vice versa. The optimum,

obtained for a Gaussian window, is called the Gabor transform. While the STFT compromise between time and frequency information can be useful, the drawback is that once you choose a particular size for the time window, that window is the same for all frequencies. Many signals require a more flexible approach, one where we can vary the window size to determine more accurately either time or frequency.

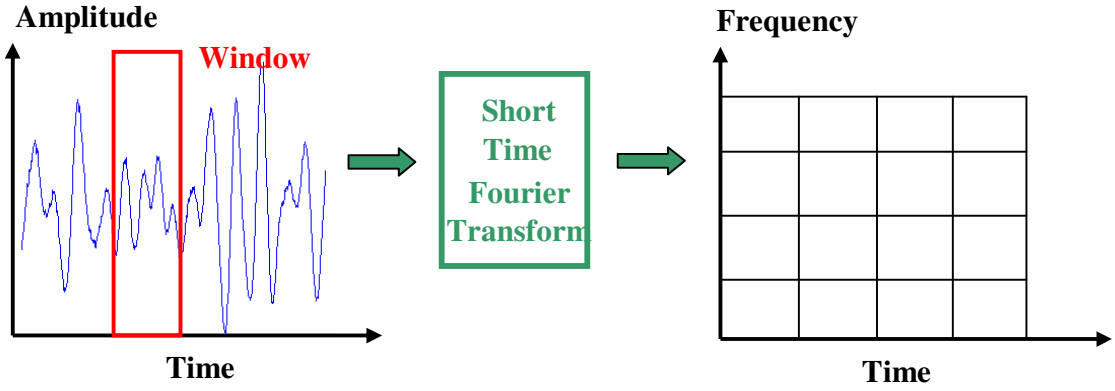

Figure 2.1: Short-time Fourier transform process

As explained above, an intuitive solution to introduce the time-dependency in the Fourier transform consists of windowing the signal x around a particular time t, computing its Fourier transform and doing that for each time instant t. The resulting transform is the Short-Time Fourier Transform and is defined by:

$$F(t,f) = \int_{-\infty}^{+\infty} x(u)h(u-t)e^{-j2\pi fu}du \qquad (2.1)$$

where $h(t)$ is a window centered at time $t=0$. Indeed, multiplying by $h(u-t)$ suppresses the signal outside a neighborhood around the time point $u=t$ and the Fourier transform of this windowed signal gives a local spectrum of the signal x around t.

2.1.2 Example

The Fourier transform analyzes a signal over its whole temporal duration. Hence, it yields information over the complete spectrum of the signal. The frequency spectrum of the signal, given in the Figure 2.2, can be used to determine that two frequencies are present in the signal, but it cannot tell us if these two frequency components overlap in time or not. The Fourier transform projects the signal in the frequency domain but loses completely the link with the time domain.

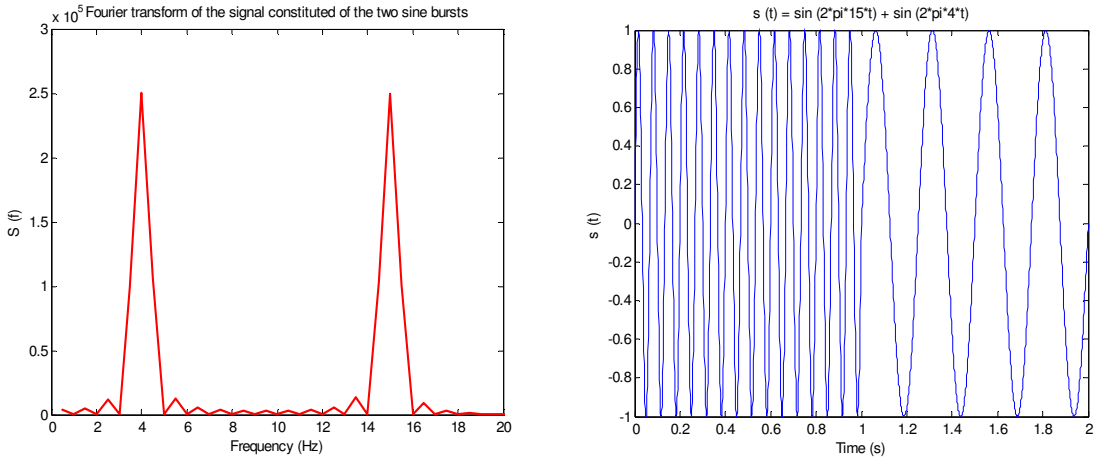

(a) Frequency domain spectrum

(b) Time domain signal

Figure 2.2: STFT application example

Let us now apply the STFT with a Gaussian window and plot the spectrogram of the signal $s(t) = \sin(2\pi f_1 t) + \sin(2\pi f_2 t)$ with $f_1 = 15Hz$ and $f_2 = 4Hz$.

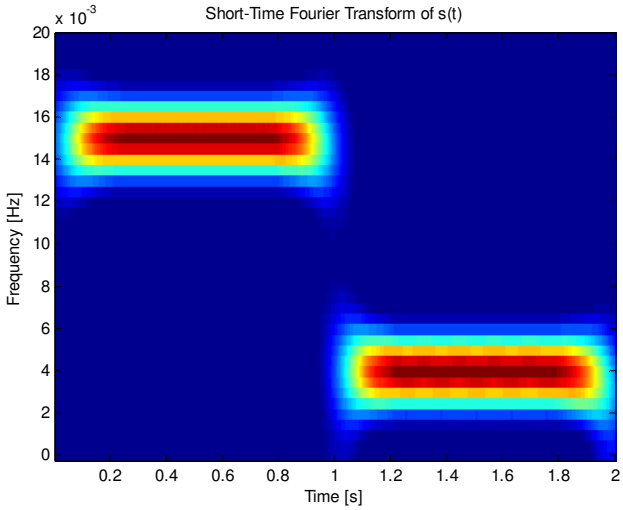

Figure 2.3: Spectrogram of the example signal $s(t)$

From the image density plot in the Figure 2.3, we can easily determine that two harmonic components are present in the signal. These components have a finite duration and we can notice some overlap in time between the components. The reason for this overlap is given by the size of the window $h(t)$. Indeed, the uncertainty principle affects the resolution of our analysis. A simple example shows the influence of the size of the window on the time-frequency resolution of the STFT. If we consider a linear frequency modulation with a Gaussian amplitude modulation and successively apply a Dirac impulse window and a constant window, we obtain the significant results shown in the Figure 2.4.

When the window $h(t)$ is chosen as a Dirac impulse, the STFT is perfectly localized in time but does not provide any frequency resolution. On the other hand, if the constant window is used, the STFT reduces to the Fourier transform and does not provide any time resolution as illustrated in the Figure 2.4. So the frequency

resolution of the STFT is proportional to the effective bandwidth of the analysis window.

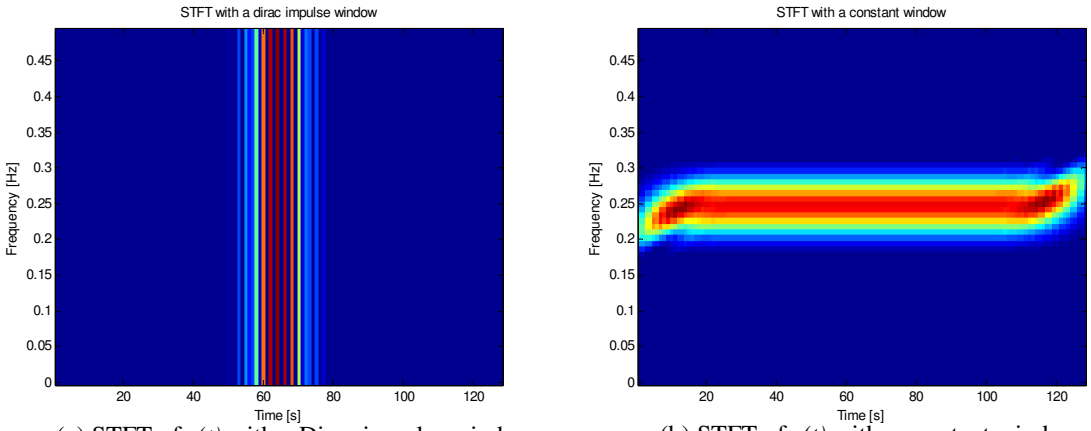

(a) STFT of *s(t)* with a Dirac impulse window (b) STFT of *s(t)* with a constant window

Figure 2.4: Illustration of the influence of the window

The Gaussian window is the optimal choice in order to get a good time-frequency resolution. The same signal is plotted in the Figure 2.5 along with its spectrogram and its frequency spectrum and shows a decent resolution.

.

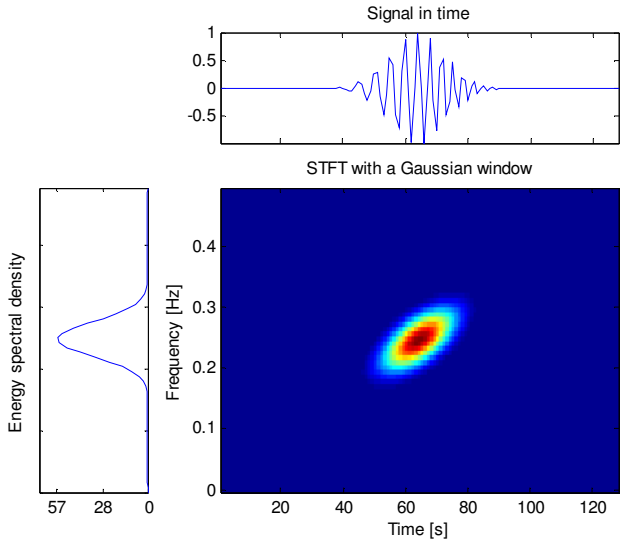

Figure 2.5: STFT of $s(t)$ with a Gaussian window

2.13 Conclusion

Gabor formulated a fundamental method for decomposition of signals in terms of atomic waveforms. His pioneering approach has now become one of the standard models for time-frequency signal analysis. The Short-time Fourier transform (or the Gabor transform, or the windowed Fourier transform) allows the analysis of signals with multiple frequency components, which occur at different and possible overlapping time intervals. However, since this transform relies on the traditional Fourier analysis, we have to assume the data to be piecewise stationary, which is not always justified for non-stationary data. Moreover, we have a trade-off between time and frequency resolutions. On one hand, a good time resolution requires a short window $h(t)$. On the other hand, a good frequency resolution requires a long window $h(t)$. This limitation is a consequence of the Heisenberg-Gabor inequality [42]. We will come back to this concept later in the chapter, since the main difference between the wavelet transform and the windowed Fourier transform is exactly how the uncertainty principle is satisfied.

These limitations render this method of limited usage although easy to implement with the fast Fourier transform.

2.2 The Wavelet Transform

2.2.1 Description of the method

To overcome the drawback of the fixed size window, the wavelet analysis has been introduced as a windowing technique with variable-sized regions. The wavelet analysis represents the next logical step and has been one of the most important and fastest evolving signal processing tools of the last twenty years. Wavelet decomposition introduces the notion of scale as an alternative to frequency, and maps a signal into a time-scale plane as shown in the Figure 2.6. This is equivalent to the time-frequency plane used in the STFT. Each scale in the time-scale plane corresponds to a certain range of frequencies in the time-frequency plane.

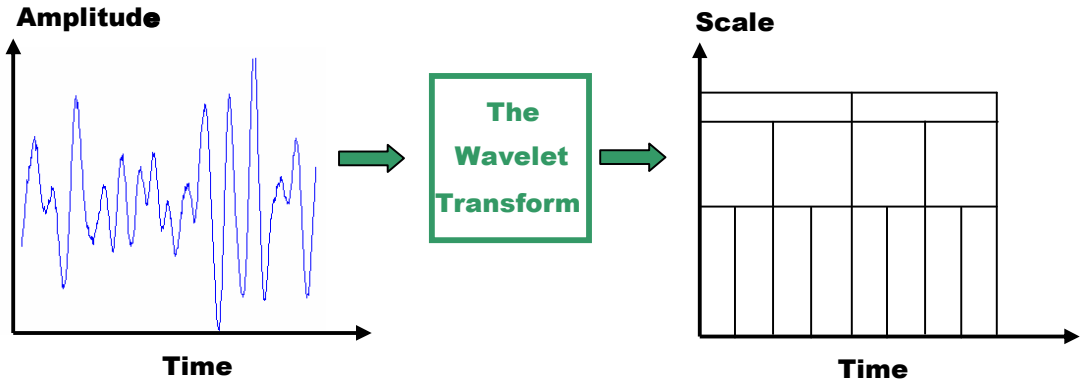

Figure 2.6: The Wavelet transform process

The wavelet transform can be classified as continuous or discrete. In general, continuous wavelets are better for time-frequency analysis and discrete wavelets are more suitable for decomposition and compression. This is the reason why only the continuous wavelet transform will be treated in this chapter.

Wavelet definition

The term wavelet means a small wave. A wavelet is a waveform of limited duration. Wavelets are localized waves that extend for a finite time duration compare to sine waves which extend from minus to plus infinity, as shown in Figure 2.7.

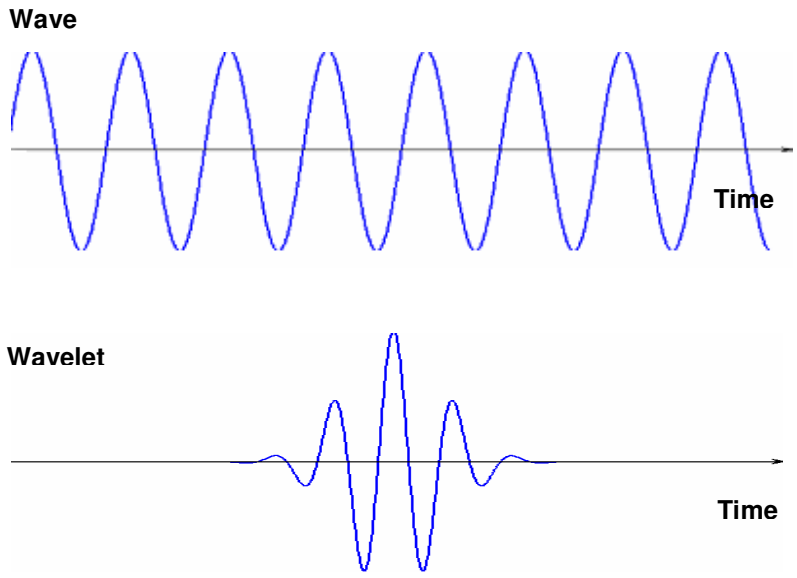

Figure 2.7: Difference between a wave and a wavelet

The comparison with the Fourier analysis is now clear. The wavelet analysis is the decomposition of a signal into shifted and scaled versions of the original wavelet whereas the Fourier analysis is the decomposition of a signal into sine waves of different frequencies.

Mathematically, the continuous wavelet transform of a function $f(t)$ is defined as the integral transform of $f(t)$ with a family of wavelet functions $\psi_{a,b}(t)$ [42]:

$$CWT_x(a,b) = \frac{1}{\sqrt{a}} \int_{-\infty}^{+\infty} f(t) * \psi\left(\frac{t-b}{a}\right) dt \qquad (2.2)$$

In other words, the continuous wavelet transform (CWT) is defined as the sum of the signal multiplied by scaled and shifted versions of the wavelet function ψ:

$$CWT(scale, position) = \int_{-\infty}^{+\infty} f(t) * \psi(scale, position, t) dt \qquad (2.3)$$

The function $\psi(t)$ is commonly called the mother wavelet and the family of functions $\psi_{a,b}(t)$ is called daughter wavelets. The daughter wavelets are derived from scaling and shifting the mother wavelet, as seen in the Figure 2.8. The scale factor a represents the scaling of the function $\psi(t)$, and the shift factor b represents the temporal translation of the function. If $|a| < 1$, the wavelet is the compressed version (smaller support in time-domain) of the mother wavelet and correspond mainly to higher frequencies. On the other hand, when $|a| > 1$, $\psi_{a,b}(t)$ has a larger time-width than $\psi(t)$ and corresponds to lower frequencies.

The normalization constant is chosen such that the norm of each function $\psi_{a,b}(t)$ is constant. The results of the CWT are many wavelet coefficients C, which are function of scale and position.

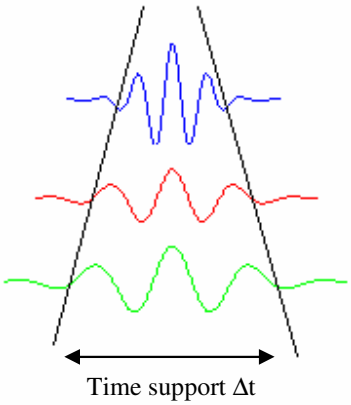

Figure 2.8: Scaling property of the wavelets

Process

The continuous wavelet transform process can be summarized in five steps [43].

(1) The first step consists in choosing a wavelet and to compare it to the start section of the original signal, as depicted in Figure 2.9.

(2) Calculate C, that represents how closely correlated the wavelet is with this section of the signal.

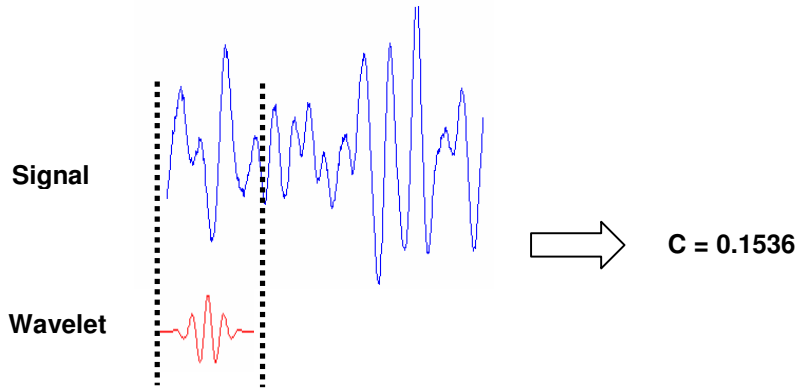

Figure 2.9: Correlation of the wavelet and the start section of the original signal

(3) Shift the wavelet to the right and repeat steps (1) and (2) until the whole signal has been covered. (see Figure 2.10)

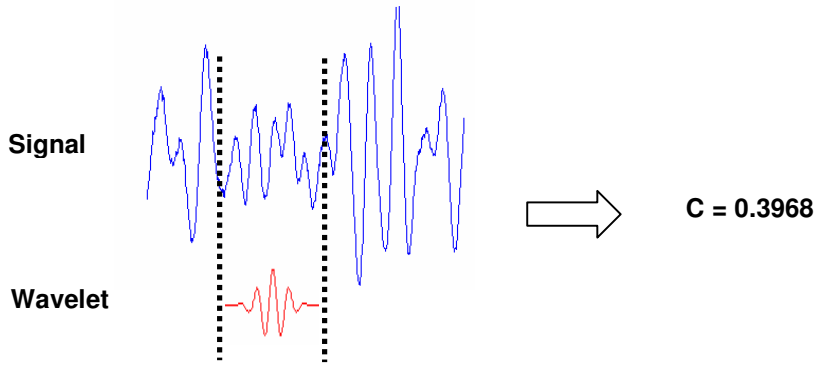

Figure 2.10: Correlation of the wavelet and the second section of the original signal

(4) Scale the wavelet and repeat steps 1 through 3 (see Figure 2.11)

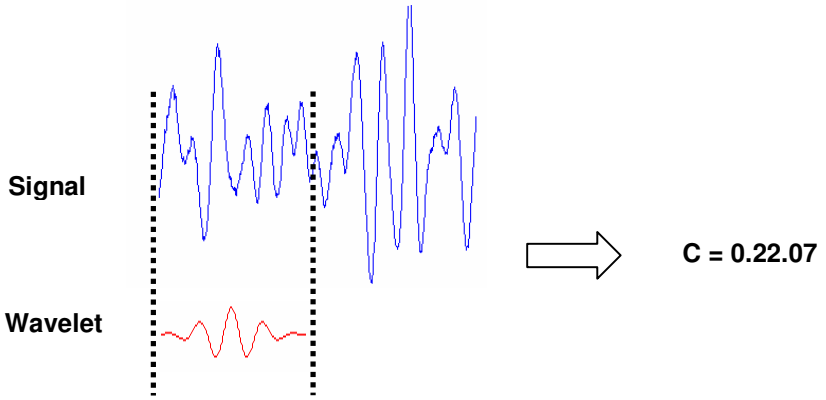

Figure 2.11: Correlation of the shifted wavelet and the start section of the original signal

(5) Repeat steps (1) through (4) for all scales.

Scalogram

A set of coefficients corresponding to the different sections at different scales is therefore created. A 2D plot can be plotted on which the x-axis represents the position along the signal (i.e time), the y-axis represents scale, and the color at each x-y point represents the magnitude of the wavelet coefficient C. It is important to mention that we obtain a time-scale representation with the wavelet transform compare to the STFT where we obtain a time-frequency representation. However each scale in the time-scale plane corresponds to a certain range of frequencies in the time-frequency plane.

2.2.2 Example

Let us consider the signal composed by a cosine at a 500Hz frequency and an impulse at $t = 0.125s$ as shown in the Figure 2.12 and let us apply the continuous wavelet transform to this signal with the Morlet wavelet. The Fourier analysis is first applied and shows its limitations as seen in the frequency spectrum of the Figure 2.12

The scalogram is plotted in the Figure 2.13 and allows a better interpretation of the frequency content of the signal.

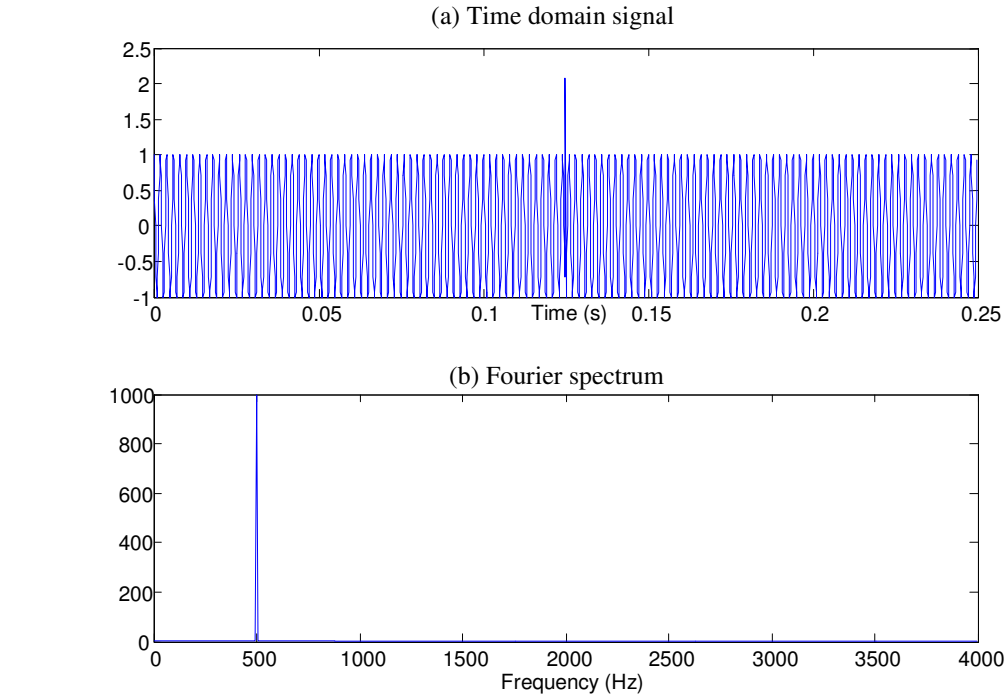

Figure 2.12: Wavelet application example – Signal *s(t)*

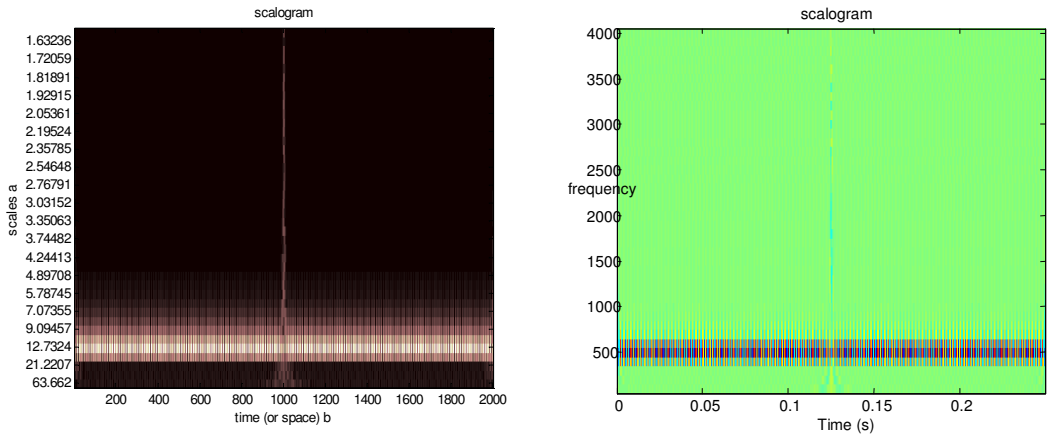

(a) Time-scale representation

(b) Time-frequency representation

Figure 2.13: Scalogram of the example signal *s(t)*

From this time-frequency representation, we can conclude that the 500Hz frequency is present during the whole time and that an impulse occurs at $t = 0.125s$. The resolution turns out to be also very good. A way to obtain a time-frequency representation instead of a time-scale representation is to compute the center frequency F_c of the wavelet and to use this relation: $F_a = \frac{F_c}{a.\Delta}$ where a is the scale, F_a is the pseudo-frequency and Δ the sampling period. The idea is to capture the main wavelet oscillation and to associate a purely periodic signal of frequency F_c. This frequency corresponds to the fast-fourier transform maximum of the wavelet, i.e the dominant frequency. So if F_c is the frequency of the wavelet, then when the wavelet is dilated by a factor a, this center frequency becomes $\frac{F_c}{a}$. If Δ is the sampling period, we naturally obtain this relationship between the scale a and the frequency: $F_a = \frac{F_c}{a.\Delta}$.

The corresponding time-frequency representation of the scalogram is plotted in the Figure 2.13. This type of representation is useful in order to compare the efficiency of the STFT and the wavelet transform in terms of time and frequency resolutions.

2.2.3 Conclusion

In the case of Fourier transform, the set of basis functions were obtained by manipulating a periodic function. Fourier analysis is therefore ideal for periodic functions. In the case of wavelet transform, the basis functions are obtained by shifting and scaling one particular function. This is the main reason for the success of

the wavelets in signal processing and time-frequency analysis. When we look at a wavelet and a sine wave (Figure 2.7), we can intuitively see that signal with sharp changes might be better analyzed with an irregular wavelet than with a smooth sinusoid. The main advantage of the continuous wavelet transforms is to zoom in to discontinuities and sharp transients. The wavelet transform has been the revolutionary signal-processing tool of the last fifty years and has been widely used in damage detection.

2.3 The Wigner-Ville Distribution

2.3.1 Description of The Method

Basically, there are two kinds of time-frequency representations. The short-time Fourier transform and the wavelet transform are linear transforms of the signal. These time frequency representations decompose the signal into elementary components well localized in time and in frequency. One other approach is to develop a joint function of time and frequency, known as a time-frequency distribution that can describe the energy density of a signal simultaneously in both time and frequency. In this case energy time-frequency distributions are obtained and are naturally quadratic transforms of the signal. The Wigner-Ville distribution (WVD) or the Wigner-Ville transform (WVT) plays a major role in the time-frequency analysis and has many desirable properties as a signal-processing tool. The first one is its ability to provide a high-resolution representation in both time and frequency for non-stationary signals. Second of all, it has the special properties of satisfying the time and frequency

marginals in terms of the instantaneous power in time and energy spectrum in frequency and the total energy of the signal in the time and frequency plane. Third, the first conditional moment of frequency at a given time is the derivative of the phase of the signal at that time. The disadvantages of the WVD are that it is nonpositive, it is bilinear and it has cross-terms.

The general class of time-frequency distributions for a given time signal $x(t)$ can be defined as the Cohen distribution [14]:

$$F_C(t,f,\phi) = \int_{-\infty}^{+\infty}\int_{-\infty}^{+\infty}\int_{-\infty}^{+\infty} \phi(\theta,\tau)x^*(u-\frac{\tau}{2})x(u+\frac{\tau}{2}) * e^{-i2\pi(\theta t+f\tau-\theta u)}dud\tau d\theta \qquad (2.4)$$

(2.4)

where $\phi(\theta,\tau)$ is an arbitrary function called the kernel. Different kernels can be chosen to obtain different properties. The best known, the Wigner-Ville distribution has been proposed by Ville in 1948 [41] and can be obtained from Equation (2.4) by taking $\phi(\theta,\tau)=1$, which results in,

$$W_x(t,f) = \int_{-\infty}^{+\infty} x^*(u-\frac{\tau}{2})x(u+\frac{\tau}{2}) * e^{-i2\pi f\tau}d\tau \qquad (2.5)$$

This distribution satisfies a large number of desirable mathematical properties. In particular, the WVD is always real-valued, it preserves time and frequency shifts and satisfies the marginal properties. The goal of this chapter is not to deal with mathematical formulas but more to understand the physic under this time-frequency distribution, the different properties and mathematical formulations of the WVD can be found in Debnath book [14].

2.3.2 Example

Let us consider for this first example the simulated signal showed on the left of the Figure 2.14. Clearly, this is an oscillating signal whose frequency varies with time. However, it is difficult to conclude from this representation what relationship exists between frequency and time. The Figure 2.14 gives an illustration of the Wigner-Ville distribution and show that the signal frequency is modulated linearly.

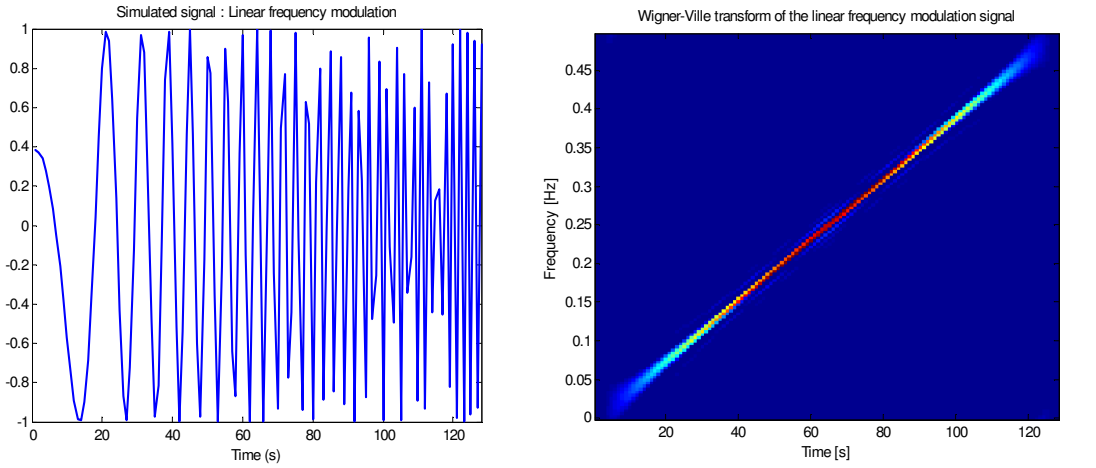

(a) Time domain signal *s(t)*

(b) Wigner-Ville time-frequency representation of *s(t)*

Figure 2.14: Wigner Ville application example

If we choose a 3-dimensional plot to represent it, we can see that the WVD can take negative values, and that the localization obtained in the time-frequency plane for this signal is almost perfect, as shown in the Figure 2.15. This example illustrates perfectly the ability of the Wigner-Ville to provide a high-resolution time-frequency representation. However, interference terms can appear due to the bilinearity of the WVD. Let us consider now a Doppler signal and its WVD distribution in the Figure 2.16.

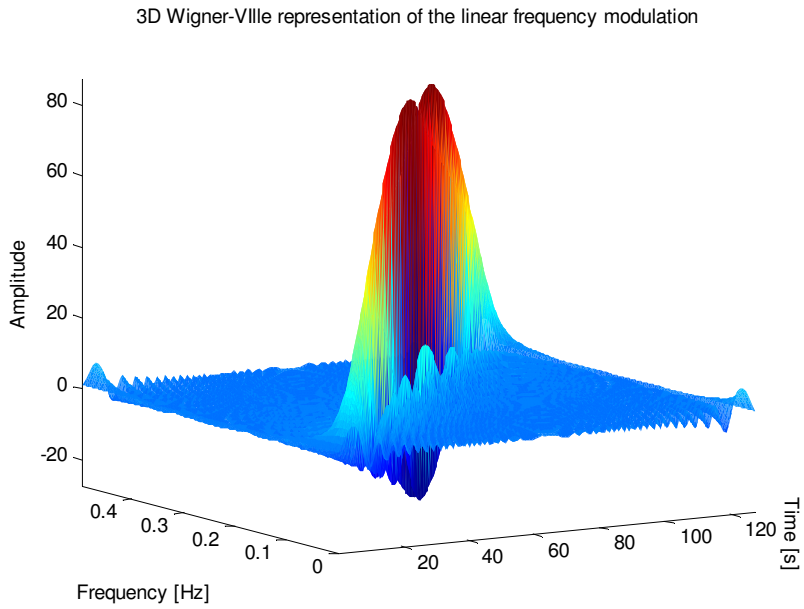

Figure 2.15: 3D Wigner-Ville representation of *s(t)*

When we look at the time-frequency distribution, we notice that the energy is not distributed as we could expect for this signal. Indeed, numerous other terms are present at positions in time and frequency where the energy should be null. The energy spectral density clearly shows that only two frequencies are present in the Doppler signal and the switch between these two frequencies occurs at $t = 125\ s$, as shown in the time-domain signal. These interference terms come from the bilinearity of the WVD. The Wigner-Ville distribution is quadratic in x, so if x is a sum $(a+b)$, the Wigner-Ville distribution of x contains an interference term $2ab$ in addition to the desired quantity (a^2+b^2). These interference terms result in an increased noise level of the Wigner-Ville distribution relative to the spectrogram. They are troublesome since they may overlap with signal terms and thus make it

difficult to visually interpret the WVD image. However, it appears that these terms must be present or the good properties of the WVD cannot be satisfied. Actually, there is a trade-off between the quantity of interferences and the number of good properties.

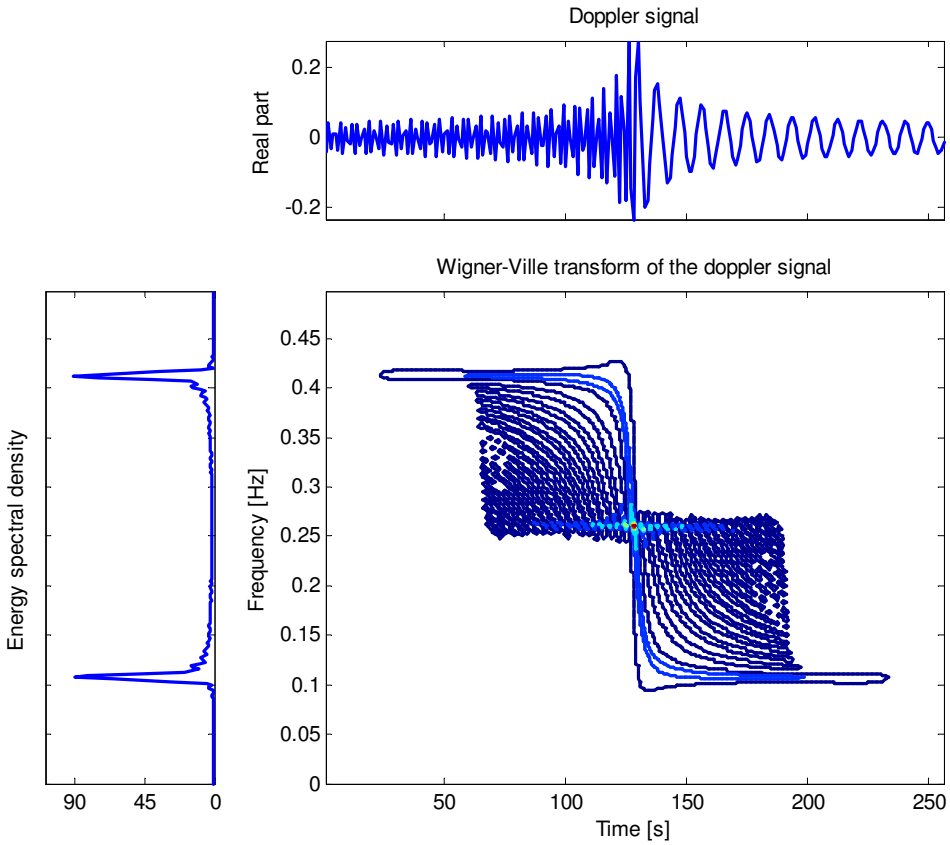

Figure 2.16: Wigner-Ville transform of a Doppler signal

In practice, smoothing in time and frequency can dramatically reduce these interference terms. The result is the smoothed-pseudo Wigner-Ville distribution (SPWVD) defined by

$$W_x(t,f) = g(t) \otimes \left(\int_{-\infty}^{+\infty} h(\tau) \left[x^*(u - \frac{\tau}{2}) x(u + \frac{\tau}{2}) \right] * e^{-i2\pi f \tau} d\tau \right) \qquad (2.6)$$

where $\otimes$ defines the convolution with respect to the time t. The function $g(t)$ is the smoothing function in time and $h(\tau)$ restricts the range of the integral in τ. Restricting the range in τ is equivalent to smoothing in frequency. The SPWVD reduces to the conventional Wigner-Ville distribution when $h(\tau)=1$ and $g(t)=dirac(t)$.

2.3.3 Conclusion

The Wigner-Ville distribution is one of the fundamental methods that have been developed over the years for the time-frequency analysis. In view of its remarkable mathematical structures and properties, the Wigner-Ville distribution is well recognized as an effective method for the time-frequency (space wavenumber) analysis of nonstationary signals (waveforms). Despite its inherent weaknesses as bilinearity and cross terms, the Wigner-Ville distribution plays a central role in the field of bilinear/quadratic time-frequency representations and can be slightly modified by smoothing in one or two dimensions to overcome its drawbacks. In recent years, this distribution has served as a useful analysis tool in many diverse fields and in structural health monitoring in particular.

2.4 Summary

A review of the most common time-frequency methods used in structural health monitoring is established in this chapter. Attention has been paid to describe these different techniques physically more than mathematically through examples. The standard Short-time Fourier transform has shown some limitations to accurately

describe nonlinear and non-stationary time series. Its poor time-frequency resolution, its Fourier dependence and its piecewise stationary assumption make it difficult to use despite its easy implementation. The Wigner-Ville distribution possesses a noteworthy mathematical structure and some interesting properties for the time-frequency analysis. However, this distribution suffers from the same limitations as the Short-time Fourier transform when its shortcomings (bilinearity, cross terms) are overcome by time and frequency smoothing. The wavelet transform is currently the most popular time-frequency method and is used in many diverse fields for the analysis of nonlinear and non-stationary signals. The shifted and scaled basis functions are the main reason for the success of wavelets in signal processing. Nevertheless, one difficulty of the wavelet analysis is its non-adaptive nature. Once the basic wavelet is selected, one will have to use it to analyze all the data. To overcome this drawback, Huang [29] introduces a new adaptive method for analyzing nonlinear and non-stationary data.

Chapter 3

The Empirical Mode Decomposition (EMD) And The Associated Hilbert Spectral Analysis

3.1 Fundamental Concepts

3.1.1 The Hilbert transform and analytical signal

Definition and formula

The Hilbert transform $H[x(t)]$ of a real-valued function $x(t)$ extended from $-\infty$ to $+\infty$ is a real-valued function defined by

$$H[x(t)] = y(t) = \lim_{\varepsilon \to 0}\left[\int_{-\infty}^{0-\varepsilon} \frac{x(u)}{\pi(t-u)}du + \int_{0-\varepsilon}^{\infty} \frac{x(u)}{\pi(t-u)}du\right] \tag{3.1}$$

assuming that $\int_{-\infty}^{\infty}[x(t)]^2 dt < \infty$, equation (3.1) can be rewritten as

$$H[x(t)] = y(t) = \frac{1}{\pi} P\int_{-\infty}^{\infty} \frac{x(u)}{t-u}du \tag{3.2}$$

where P indicates the Cauchy principal value. This transform exists for all functions of class L^p. Thus, $y(t)$ is the Hilbert transform of the initial process $x(t)$. A description of the Hilbert transform with the emphasis on its mathematical formality can be found in Bendat and Piersol [44]. Essentially equation (3.2) defines the Hilbert transform as the convolution of $x(t)$ with $\frac{1}{t}$; it therefore emphasizes the local properties of $x(t)$, even though the transform is global. Physically, the Hilbert

Transform can also be interpreted as a natural $\pi/2$ phase shifter, which consists of passing $x(t)$ through a system that leaves the magnitude unchanged, but changes the phase of all frequency components by $\pi/2$. With this definition, $y(t)$ forms the complex conjugate of $x(t)$ and we can define the analytical signal, $z(t)$, as

$$z(t) = x(t) + iy(t) \tag{3.3}$$

The advantage of this representation lies in the fact that the possibility arises of uniquely determining genuine time-variant variables. These are the instantaneous parameters with amplitude as $a(t) = \sqrt{x(t)^2 + y(t)^2}$ and phase $\theta(t) = \arctan\left(\frac{y(t)}{x(t)}\right)$.

Finally, Equation (3.3) can be rewritten as

$$z(t) = a(t)e^{i\theta(t)} \tag{3.4}$$

In this equation, the polar coordinate expression further clarifies the local nature of this representation. It is the best local fit of an amplitude and phase varying trigonometric function to $x(t)$. The Hilbert transform forms the basis of the definition of an analytical signal and provides a unique way of defining the imaginary part so that the result is an analytic function. In the frequency domain, the definition of the analytical signal has a simple interpretation since $TF[z(t)]$ is a single sided Fourier transform where the negative frequency values have been removed, the strictly positive ones have been doubled, and the DC component is kept unchanged:

$$\begin{aligned} Z(\upsilon) &= 0 \text{ if } \upsilon < 0 \\ Z(\upsilon) &= X(0) \text{ if } \upsilon = 0 \\ Z(\upsilon) &= 2X(\upsilon) \text{ if } \upsilon > 0 \end{aligned} \tag{3.5}$$

in which $X(\upsilon)$ is the Fourier transform of $x(t)$ and $Z(\upsilon)$ is the Fourier transform of $z(t)$.

Thus, the analytic signal can be obtained from the real signal by forcing to zero its spectrum for the negative frequencies, which do not alter the information content since for a real signal, $X(-\upsilon) = X^{*}(\upsilon)$.

An example of Hilbert transform

A simple sine wave and its Hilbert transform (cosine wave) is plotted for comparison in the Figure 3.1.

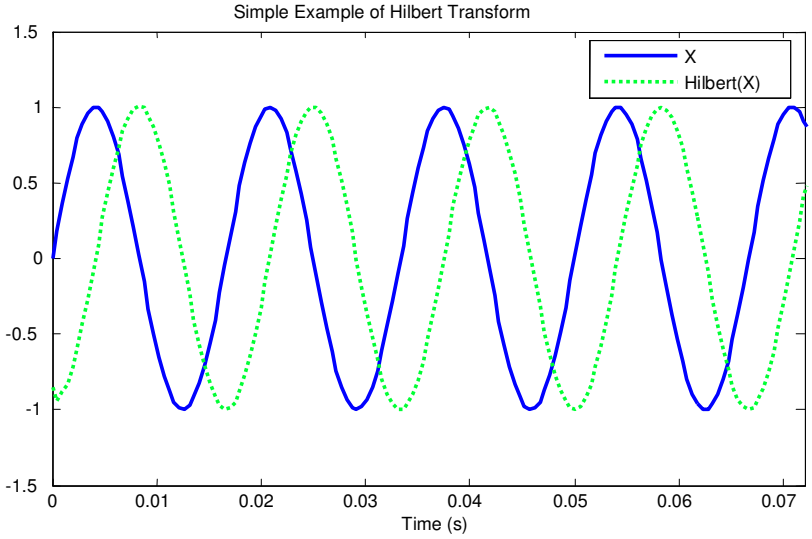

Figure 3.1: Hilbert transform of a sine wave

A phase shift of $\pi/2$ is clear. Since this signal only involves a single frequency wave, the instantaneous amplitude is constant and the phase function is a straight line, as shown in the Figure 3.2.

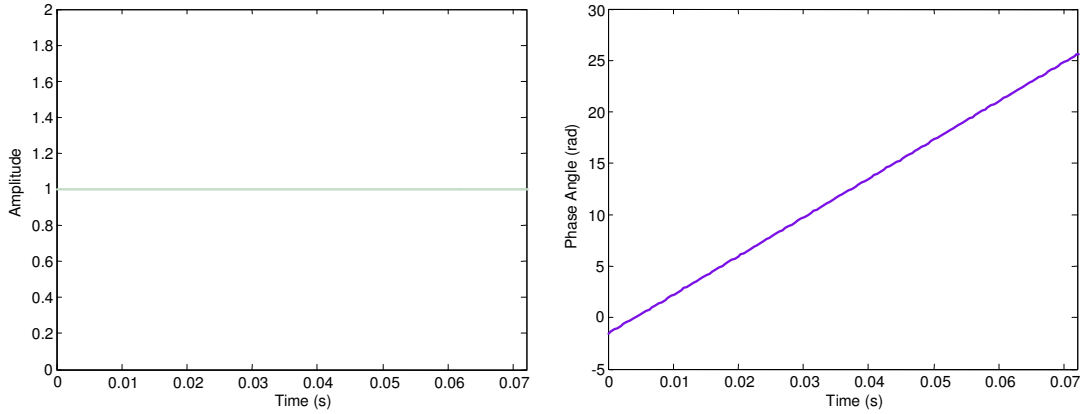

(a) Instantaneous amplitude (b) Instantaneous phase

Figure 3.2: Amplitude and phase of the Hilbert transform of a sine wave

3.1.2 The Instantaneous Frequency

Definition and concept

The notion of instantaneous frequency has been highly controversial and even with the Hilbert transform, there is still considerable controversy in defining the instantaneous frequency as the rate of phase change

$$\omega = \frac{d\theta}{dt} \text{ and } f = \frac{1}{2\pi}\frac{d\theta}{dt} \tag{3.6}$$

The definition of the instantaneous frequency presented here is the most basic but is by no means unique. Ville [41] defined another estimator for the instantaneous frequency as the first moment of the distribution with respect to frequency. Cohen [45] defined the instantaneous frequency to be the average of the frequencies that exist in the time-frequency plane at a given time. A comprehensive discussion on the various proposed formulations may be found in Boashash [46]. The main difficulty in accepting the idea of instantaneous frequency arises from the definition of the

‘global’ frequency in the traditional Fourier analysis. The frequency is indeed defined for the sine or cosine function spanning the whole data length with constant amplitude. As an extension of this definition, the instantaneous frequencies also have to relate to either a sine or a cosine function. Thus, we need at least one full oscillation of a sine or a cosine wave to define the local frequency value. According to this logic, nothing shorter than a full wave will do. Such a definition would not make sense for non-stationary data for which the frequency has to change values from time to time, so that there is an apparent paradox in associating the words ‘‘instantaneous’’ and ‘‘frequency’’. If the concept of instantaneous frequency is applied blindly to any analytic function, one may run into one of the four paradoxes discussed by Cohen [47]. Hence, some limitations on the data are necessary, since the instantaneous frequency given in Equation (3.6) is a single value function of time. The definition implies that at any given time, there is only one frequency value. This leads Cohen [47] to introduce the term, ‘monocomponent function’, which have been loosely defined as narrow band. Finally, one reasonable and meaningful definition of the instantaneous frequency could be the representation of the frequency of the signal at one time, without any information about the signal at other times.

The illustration of the instantaneous frequency concept for a ‘monocomponent’ signal can easily confirm from the definition that the instantaneous frequency of a harmonic function is constant and coincides with the frequency of the function. One can gain intuitive appreciation for the concept of instantaneous frequency by examining a chirp signal. A linear chirp is defined as $y(t) = \cos[(at)t]$ from where the

interpretation of a frequency varying linearly with time is evident. A plot of a linear chirp with its instantaneous frequency computed from Equation (3.6) is plotted in Figure 3.3.

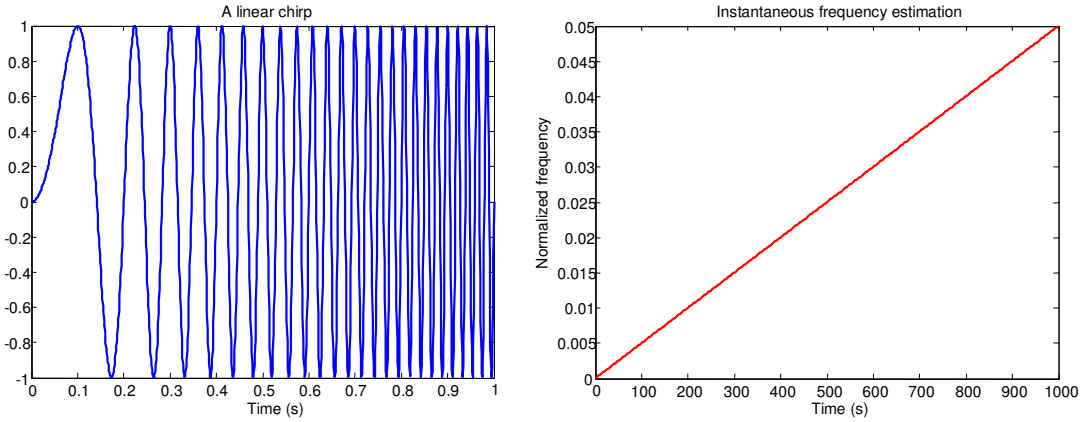

(a) Time domain signal (b) Instantaneous frequency

Figure 3.3: Instantaneous frequency of a linear chirp

As one can see, the instantaneous frequency definition captures the time variation of the frequency accurately. However, when the chirp is represented in the Fourier domain the result contains a large number of components with different frequencies and the simple nature of the signal is lost.

Limitations and restrictions

As mentioned above, the notion of instantaneous frequency implicitly assumes that, at each time instant, there exists only a single frequency component. Thus, if this assumption is no longer valid, which is the case for most of the multi-component signals, the result obtained using the instantaneous frequency is meaningless. For example, let us consider the superposition of two linear frequency modulations. At each time instant t, an ideal time-frequency representation should represent two

different frequencies with the same amplitude. The result obtained using the instantaneous frequency is completely different, and therefore irrelevant as seen in the Figure 3.4.

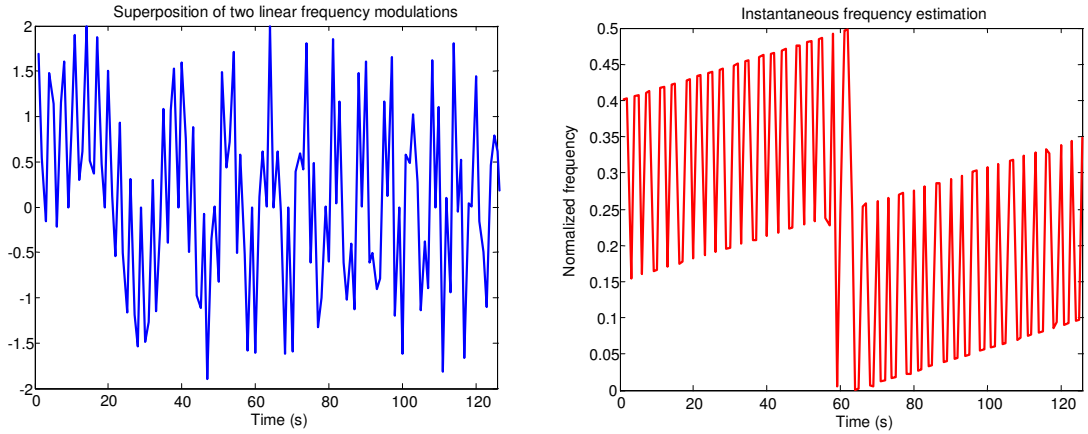

(a) Time domain signal (b) Instantaneous frequency

Figure 3.4: Instantaneous frequency of a multi-components signal

Meaningful instantaneous frequency

In order to obtain meaningful instantaneous frequency, restrictive conditions have to be imposed on the data as discussed by Gabor [48] and Boashash [46]: the frequency of the signal must be positive. Let us consider some simple examples to illustrate this restriction physically, by examining the function $x(t) = \alpha + \sin t$ for $\alpha = 0, 0.5, 1.5$ and by computing the phase function and the instantaneous frequency for each value of α. The phase function of $\sin t$ is a straight line. The phase plot of x-y plane is a simple circle of unit radius as shown in the Figure 3.5. If we change the signal mean by adding a small amount α, the phase plot is still a simple circle independent of the value of α. However, the center of the circle is displaced by the amount α.

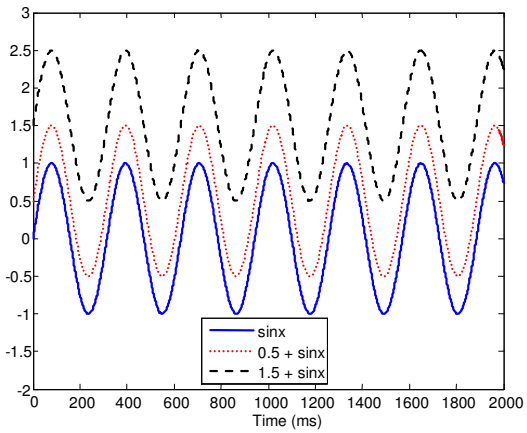

(a) Time domain signals

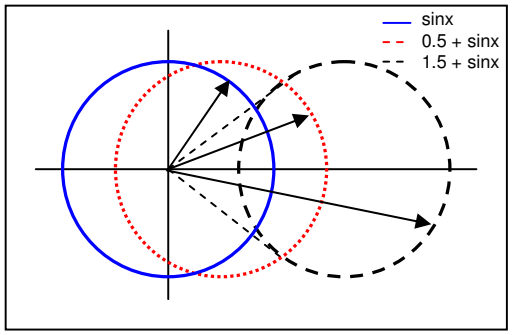

(b) Phase plane for the model functions

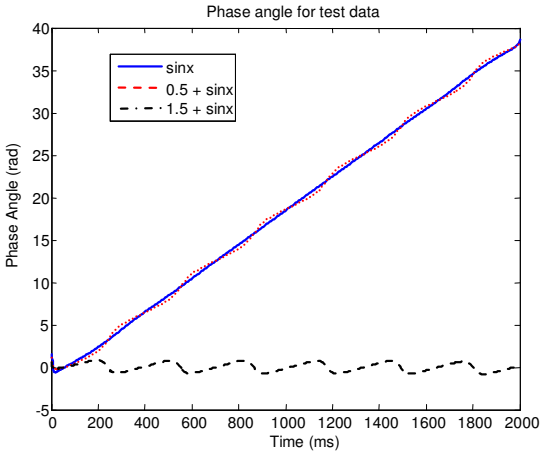

(c) Unwrapped phase of the model functions

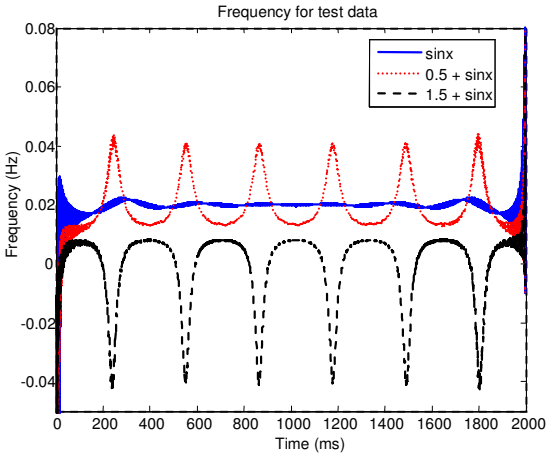

(d) Instantaneous frequencies of the model functions

Figure 3.5: Physical interpretation of instantaneous frequency

If $\alpha < 1$ the Fourier spectrum has a DC term but the mean zero-crossing frequency is still the same. This case corresponds to any asymmetric waveform.

If $\alpha > 1$ both phase function and instantaneous frequency will assume negative value, which is meaningless. This case corresponds to any riding waves.

These simple examples illustrate physically that, for a simple signal such as a sine function, the instantaneous frequency can be defined only if we restrict the function to be symmetric locally with respect to the zero mean level.

Conclusion

The examples presented above, lead to the definition of a class of functions for which the instantaneous frequency can be defined everywhere. A new method needs therefore to be introduced in order to decompose any signal into a superposition of components with well-defined instantaneous frequency. This method will have to locally eliminate riding waves and asymmetries (defined by envelope of extrema) in order to obtain a series of monocomponent contributions. This new method has been introduced by Huang in 1998 [29] and is called 'the empirical mode decomposition'.

3.1.3 The Hilbert-Huang transform

The Hilbert-Huang transform scheme can be divided into two parts. In the first step, the experimental data are decomposed into a collection of intrinsic mode functions (IMFs). This decomposition is viewed as an expansion of the data in terms of the IMFs. In other word, these IMFs are regarded as the basis of that expansion which can be linear or nonlinear as dictated by the data. Since the IMFs have well-behaved Hilbert transforms, the corresponding instantaneous frequencies are calculated. Thus, in the next step, we could localize any event on the time as well as the frequency axis. The local energy and the instantaneous frequency derived from the IMFs give us a

full energy-frequency-time distribution of the data, and such a representation is designated as the Hilbert spectrum.

Part I: The Empirical Mode Decomposition

Intrinsic mode function

Based on the observations of the previous section, a new class of functions designated as intrinsic mode functions can be proposed for the instantaneous frequency to make sense. An intrinsic mode function (IMF) is a function that satisfies two conditions:

(1) in the whole data set, the number of extrema and the number of zero crossings must either equal or differ at most by one

(2) at any point, the mean value of the envelope defined by the local maxima and the envelope defined by the local minima is zero

The first condition is similar to the narrow-band requirement for a stationary Gaussian process. It ensures that the local maxima of the data series are always positive and the local minima are negative, respectively. The second condition modifies a global requirement to a local one, and is necessary to ensure that the instantaneous frequency will not have unwanted fluctuations arising from asymmetric waveforms. An example of an IMF is plotted on the Figure 3.6.

IMFs represent oscillatory modes embedded within data where each IMF involves only one mode of oscillation with no complex riding waves present. An IMF can be non-stationary and either be amplitude and/or frequency modulated.

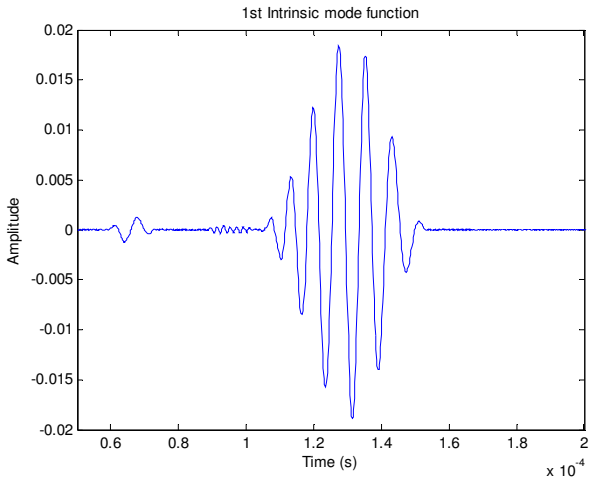

Figure 3.6: Intrinsic mode function (IMF) example

Intrinsic mode functions could be considered as a more general case of the simple harmonic functions. It has to be mentioned that, by definition, intrinsic mode functions always have positive frequencies, because the oscillations in IMFs are symmetric with respect to the local mean.

The sifting process

In general, most of the data are not naturally IMFs and the Hilbert transform cannot provide the full description of the frequency content if the data involves more than one oscillatory mode at a given time. Hence, we need to find a way to decompose the data into a set of independent IMF components.

Huang introduced a method to decompose a complicated data into IMF components with meaningful instantaneous frequencies. This new method is intuitive, direct, a posteriori and adaptive. The decomposition is based on three assumptions:

(1) the signal has at least two extrema, one maximum and one minimum

(2) the characteristic time scale is defined by the time lapse between the extrema

(3) if the data were totally devoid of extrema but contained only inflection points, then it can be differentiated once or more times to reveal the extrema.

The sifting process to find the IMFs of a signal consists of several steps. We will describe these steps using an arbitrary signal denoted $x(t)$.

(1) Find the positions and amplitudes off all local maxima and minima in the input signal. These are marked by green and yellow dots respectively in the Figure 3.7.

(2) Create the upper envelope by spline interpolation of the local maxima and the lower envelope by spline interpolation of the local minima, denoted $e_{\max}(t)$ and $e_{\min}(t)$. These are shown as the blue and red curves in the Figure 3.7.

(3) For each time instant *t*, calculate the mean of the upper envelope and the lower envelope.

$$m_1 = \frac{e_{\max}(t) + e_{\min}(t)}{2} \tag{3.7}$$

This signal is referred to as the envelope mean and is shown as the black line in the Figure 3.7.

(4) Subtract the envelope mean signal from the input signal (black from blue, yielding the results illustrated by blue in Figure 3.7.

$$h_1(t) = x(t) - m_1 \tag{3.8}$$

This is one iteration of the sifting process. The next step is to check if the signal $h_1(t)$ is an IMF or not. In the original work of Huang, the sifting

process stops when the difference between two consecutive siftings is smaller than a selected threshold SD, defined by

$$SD = \sum_{t=0}^{T} \left[\frac{\left| (h_{1(k-1)}(t) - h_{1k}(t)) \right|^2}{h_{1(k-1)}^2(t)} \right] \tag{3.9}$$

We will see later that the choice of the stop criterion is crucial in order to get meaningful IMF components.

(5) If $h_1(t)$ is not an IMF, iterate by repeating the process from step (1) with the resulting signal from step (4). In the second sifting process, $h_1(t)$ is therefore treated as the data, then

$$h_{11} = h_1 - m_{11} \tag{3.10}$$

We can repeat this sifting procedure *k* times, until h_{1k} is an IMF, that is

$$h_{1k} = h_{1(k-1)} - m_{1k} \tag{3.11}$$

When the stop criterion is met, the IMF is defined as

$$c_1 = h_{1k} \tag{3.12}$$

After the IMF c_1 is found (illustrated by the blue curve in the Figure 3.7) define the residue r_1 as the result of subtracting this IMF from the input signal

$$r_1 = x(t) - c_1 \tag{3.13}$$

The residue is illustrated by the blue curve in the Figure 3.7.

(6) The next IMF is found by starting over from step (1), now with the residue as the input signal.

Steps (1) to (6) can be repeated for all the subsequent r_j and the result is

$$r_1 - c_2 = r_2, \ldots, r_{n-1} - c_n = r_n \tag{3.14}$$

The EMD is completed when the residue, ideally, does not contain any extrema points. This means that it is either a constant or a monotonic function. The signal can be expressed as the sum of IMFs and the last residue

$$x(t) = \sum_{i=1}^{n} c_i + r_n \tag{3.15}$$

The extracted IMFs are symmetric, have a unique local frequency and different IMFs do not exhibit the same frequency at the same time

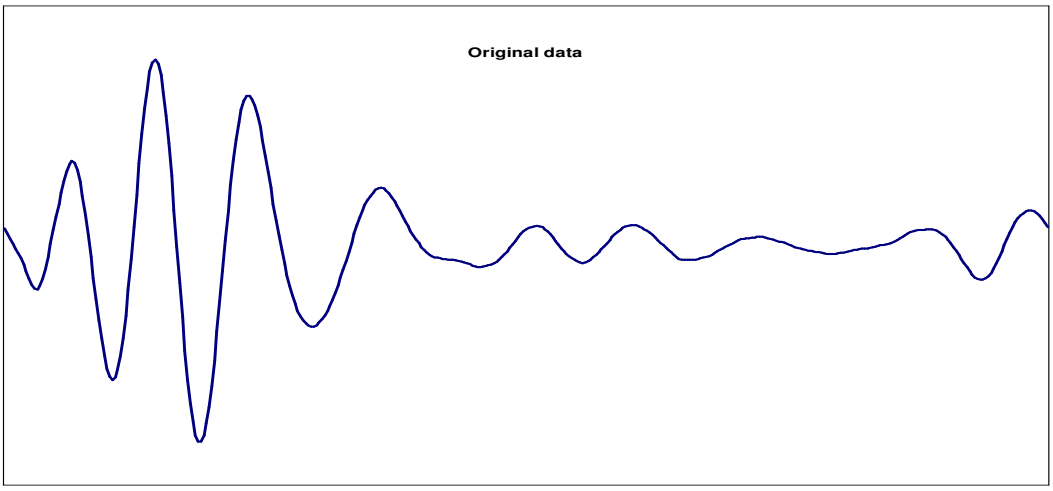

(a) Original signal

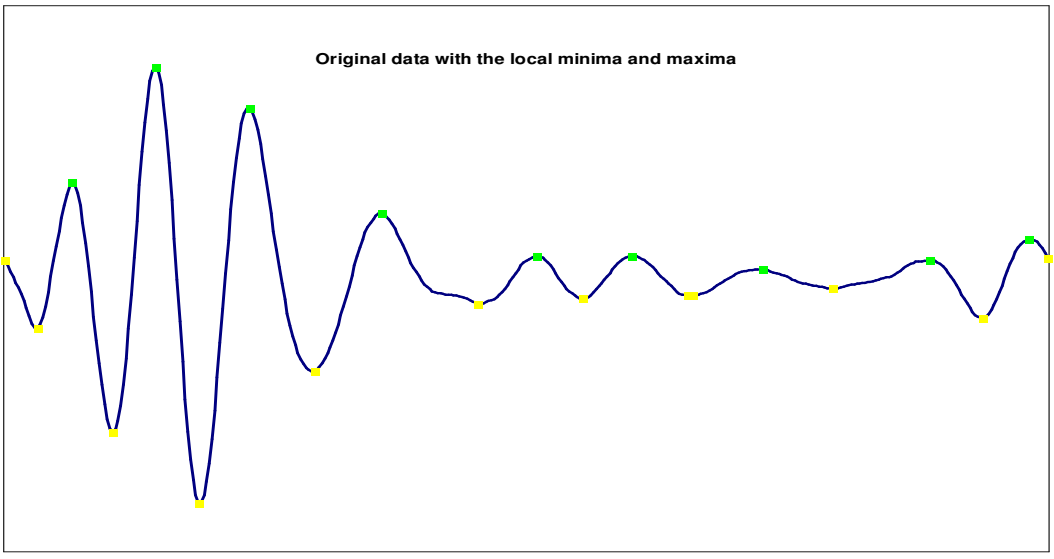

(b) Localization of the local extrema

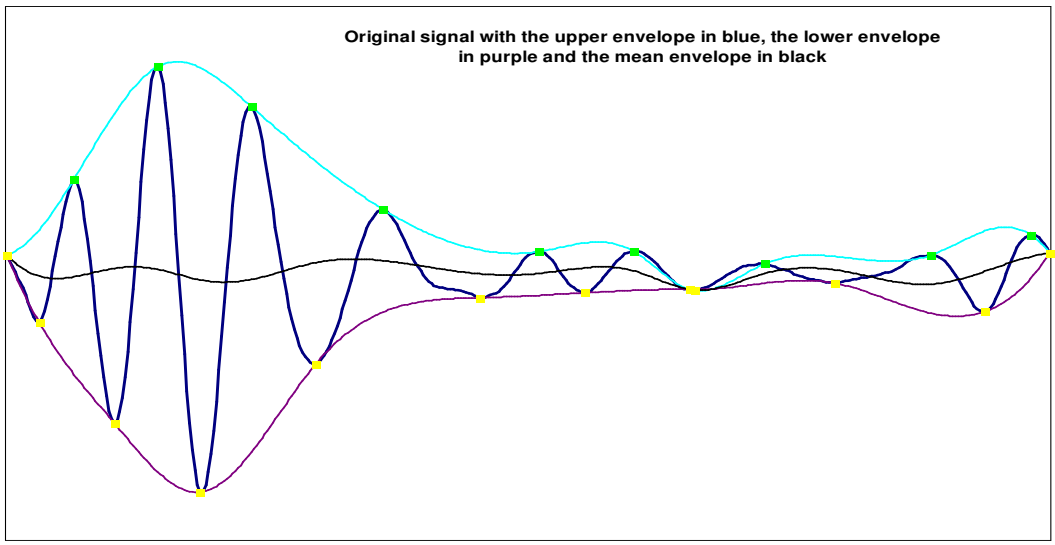

(c) Spline fitting

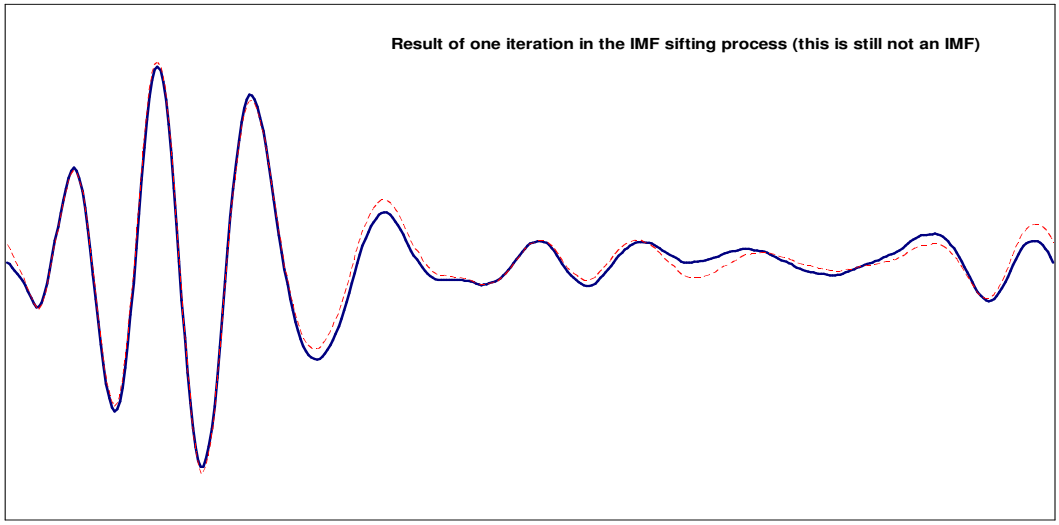

(d) Result of one iteration of the sifting process

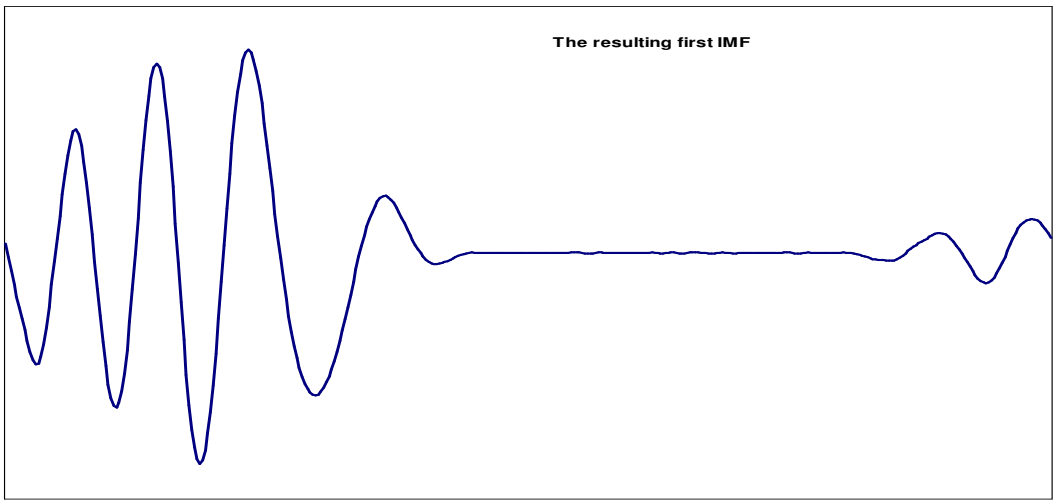

(d) Resulting first IMF

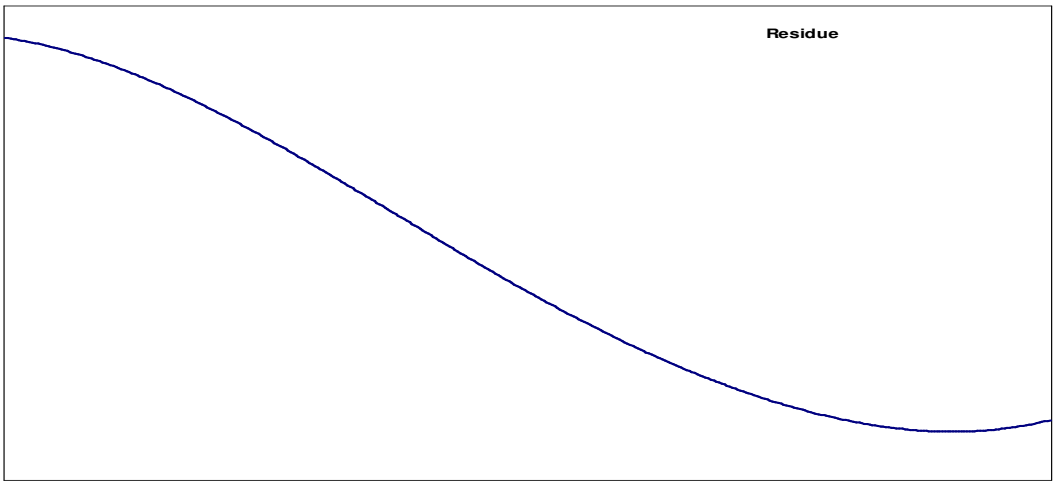

(f) Residue function

Figure 3.7: Sifting process illustration

The decomposition steps are based on the simple assumption that any data consists of different simple intrinsic modes of oscillations. Each mode may or may not be linear, and will have the same number of extrema and zero-crossings. Furthermore, the oscillation will also be symmetric with respect to the 'local mean'. At any given time, the data may have many different coexisting modes of oscillation, one superimposing on the others. The result is the final complicated data. An IMF represents each of these oscillatory modes. To clarify the decomposition process, Figure 3.8 summarizes the procedure of the EMD. The sifting process serves two purposes: to eliminate riding waves and to make the wave-profiles more symmetric in smoothing uneven amplitudes. While the first condition is absolutely necessary for separating the intrinsic modes and for defining a meaningful instantaneous frequency, the second condition is also necessary in case the neighboring wave amplitudes have too large a disparity. Another way of explaining how the EMD works is that it picks out the highest frequency oscillation that remains in the signal.

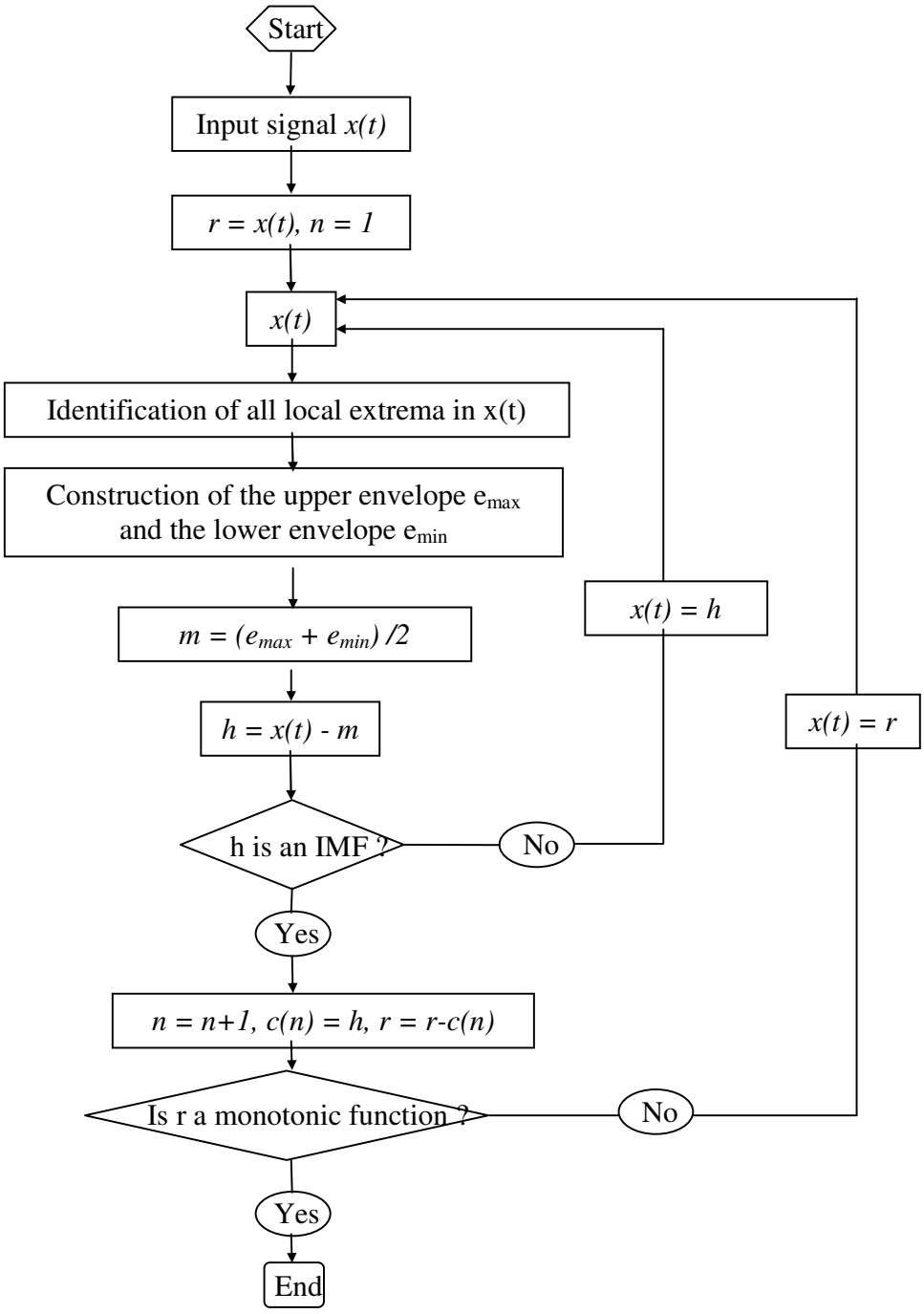

Figure 3.8 Flow chart of the EMD

Thus, locally, each IMF contains lower frequency components than the one extracted just before. The set of IMFs obtained is unique and specific for the particular time series since it is based on and derived from the local characteristics of these data. Hence, the sifting process allows one to decompose the data into n-empirical modes and a residue.

Part II : The Hilbert Spectral Analysis

The Hilbert transform of IMFs

The empirical mode decomposition gives us a set of independent IMF components with meaningful instantaneous frequencies. Each of the IMF components can be therefore treated as a signal where the Hilbert transform can be applied.

$$c(t) = a_j(t) * \exp\left(i \int \omega_j(t) dt\right) \tag{3.16}$$

After performing the Hilbert transform on each IMF component, the original data $x(t)$ can be expressed as a real part (RE) of the complex expansion:

$$x(t) = RE\left[\sum_{j=1}^{n} a_j(t) * \exp\left(i \int \omega_j(t) dt\right)\right] \tag{3.17}$$

The residue r_n is omitted on purpose because it is either a monotonic function or a constant. Here, both amplitude $a_j(t)$ and instantaneous frequency $\omega_j(t)$ are function of time t in contrast with the constant amplitude and frequency in the Fourier expansion.

$$x(t) = RE\left[\sum_{j=1}^{\infty} a_j e^{i\omega_j t}\right] \tag{3.18}$$

Hence, the IMF represents a generalized Fourier expansion.

The Hilbert spectrum

Equation (3.17) enables us to represent the amplitude and the instantaneous frequency as functions of time in a three-dimensional plot, in which the amplitude can be contoured on the frequency-time plane. This frequency-time distribution of the amplitude is designated as the Hilbert amplitude spectrum, $H(\omega,t)$, or simply Hilbert spectrum. Various forms of Hilbert spectra presentations can be made. The first one, the skeleton form, will emphasize frequency variations of each IMF and will be used if more quantitative results are desired. A second form, commonly used as a first look, is the smoothed Hilbert spectrum. If we apply a weighted spatial filter with large enough spatial averaging, we obtain a smoothed spectrum similar to what the wavelet analysis would give. Even if such a smoothing degrades both frequency and time resolutions, it could give a better physical interpretation. Hence, if more qualitative results are desired, the smoothed presentation is more appropriate. Both forms of the Hilbert spectrum are shown in the Figure 3.8 for the example treated in the sifting process section.

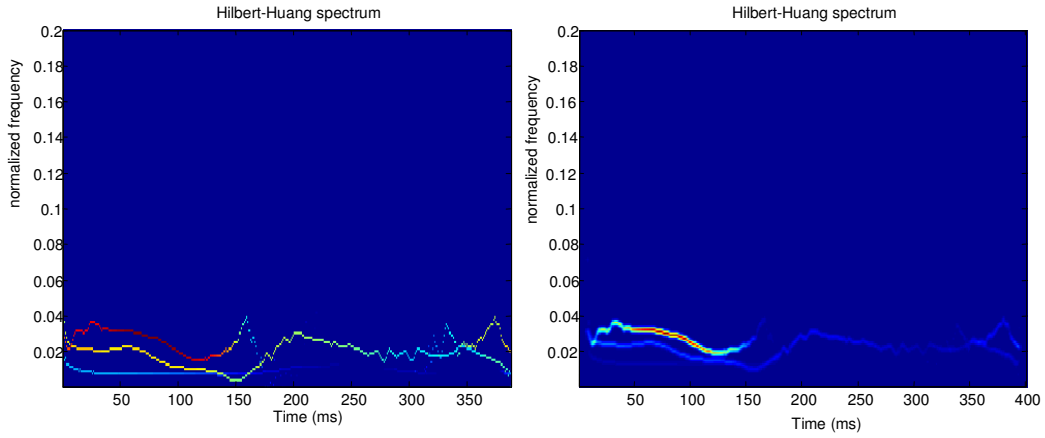

(a) Skeleton form (b) Smoothed form

Figure 3.9: Hilbert-Huang spectrum

The time resolution of the Hilbert spectrum can be as precise as the sampling rate in the data, while the frequency resolution is arbitrary. The lowest extractable frequency is $1/T$, where T represents the duration of the record and the highest frequency is $1/(n\Delta t)$, where $n = 5$ is a minimum number of points, necessary to define frequency accurately and Δt is the sampling rate.

3.2 Program Implementation

Matlab 7.0 was adopted for the numerical implementation of the HHT method in this work. As defined above, the EMD algorithm depends on a number of parameters, which have to be controlled by the user. Spline fitting, stopping criterion and end effects can affect the overall success of the analyzing procedure and hence need to be carefully investigated in order to avoid some inconsistency in the decomposition.

3.2.1 Stop Criterion

To guarantee that the IMF components retain enough physical sense of both amplitude and frequency modulations, we have to determine a criterion for the sifting process to stop. On one hand, a too stringent criterion can result in over-decomposing the data, giving non-physical IMF components. On the other hand, a too lax criterion may not reveal the actual IMF components of the data.

Huang [29] first introduced the standard deviation as a stopping criterion. The standard deviation, SD, is computed from the two consecutive sifting results as

$$SD = \sum_{t=0}^{T} \left[\frac{\left| (h_{1(k-1)}(t) - h_{1k}(t)) \right|^2}{h_{1(k-1)}^2(t)} \right] \tag{3.19}$$

This criterion is typically set between 0.2 and 0.3 and seems to work in practice even if it is an ad hoc criterion. However, numerical simulations indicate that such stop criterion requires a lot of siftings and therefore increase the computer time in extracting each IMF.

Quek [31] proposed another criterion as an alternative measure, defined as

$$SD = \frac{\sum_{t=0}^{T} \left| (h_{1(k-1)}(t) - h_{1k}(t)) \right|^2}{\sum_{t=0}^{T} h_{1(k-1)}^2(t)} \tag{3.20}$$

This criterions turn out to be more efficient along with a good choice of the critical value. A new criterion have been considered by Rilling, et al. [49], which takes into account the locally large excursions while guaranteeing globally small fluctuations in the mean. This criterion is based on two thresholds θ_1 and θ_2 and an evaluation function $\sigma(t) = \left| m(t) / a(t) \right|$ with $a(t) = \frac{e_{\max}(t) - e_{\min}(t)}{2}$. The sifting is iterated until $\sigma(t) < \theta_1$ for 95 % of the total duration, while $\sigma(t) < \theta_2$ for the remaining 5 %. These three different stop criterions have been tested and the most efficient one turns out to be the last one in terms of the number of iterations and computer time.

3.2.2 Spline Fitting

Special attention has to be paid to the problem of obtaining the true envelopes of the signal. The interpolation to produce envelopes from the extrema points can be done in different ways and the nature of the chosen interpolation plays an important role. As the description of the sifting process indicates, the spline fitting is the essential step in generating the intrinsic mode function, the basis for the Hilbert spectral analysis. Cubic splines are commonly used but serious problems can occur near the ends, where the cubic spline fitting can have large swings. The approximate envelopes obtained by the cubic spline interpolation do not always encompass all the data and some leakage can occur, corrupting the signal, as seen in the Figure 3.9. The cubic spline fitting adopted here has both overshoot and undershoot problems. This problem can be overcome by over sampling the discrete signal $x(t)$, resulting in a better localization of the extrema. Another way to get rid of these near end distortions is to use higher-order spline fitting, which is more time consuming. A new method introduced by Blakely [50] takes advantage of the theory of matrix-free moving least-squares approximation to construct the approximate envelopes without the need of solving a system of equations. This method provides an attractive alternative to the cubic spline and offers a fast computation time.

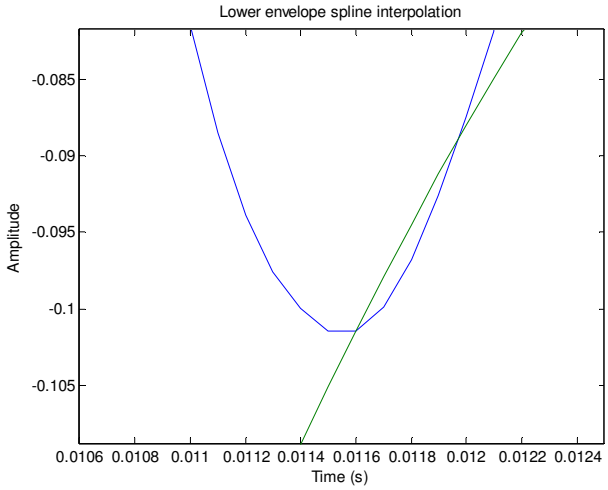

Figure 3.10: Spline fitting leakage

The spline can contaminate the IMFs through the thousand of siftings. Indeed, when we consider the case of the linear sum of two cosine waves with very close frequencies, the EMD cannot extract the two components and the instantaneous frequencies of the components become overlapped. The key problem here is the spline fitting. Unless a better spline fitting is implemented, EMD will not be able to improve the instantaneous frequencies definition in such a case. Thus, the spline fitting appears to be a major factor in the limitations of the Hilbert spectral analysis.

3.2.3 End Effects

Due to a final length signal and its polar representation, the Hilbert Transform experienced the Gibbs phenomenon, caused by representing a discontinuity at the beginning and at the end of the signal (see Figure 3.10). Another type of end effects is due to the spline fitting. At the ends, the cubic splines can indeed have wide swings if left unattended. To alleviate both types of end effects, Huang [29] proposed to add two characteristics waves at the beginning and at the end of the signal to smooth it at

the edges. Another efficient method is to over sample the signal so that the propagation of end effects is outside the required window.

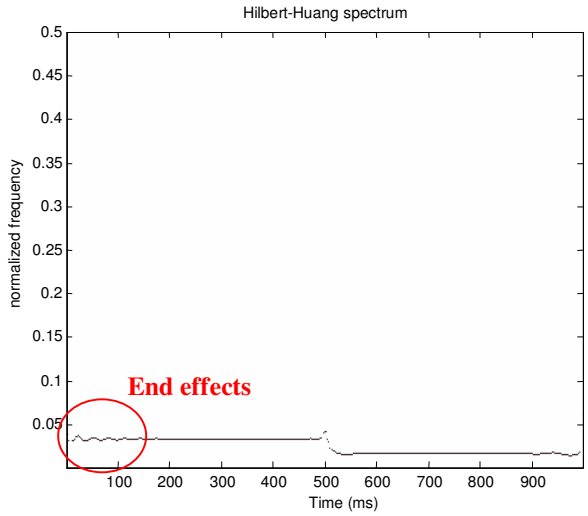

Figure 3.11: End effects illustration

3.3 Program Validation and Comparison

To show the efficiency of the empirical mode decomposition and the Hilbert spectrum, a simple example has been studied and compared to the time-frequency methods reviewed in the previous chapter.

3.3.1 Analyzed Signal

Let us first validate the implementation of the Hilbert-Huang transform on a relevant example. We will consider the case of a simple sine wave with one frequency suddenly switching to another frequency and a Dirac type impulse occurring at a certain time. This signal *s(t)* is defined by the Equation (3.21)

$$\begin{cases} s(t) = \cos(2\pi f_1 t) & 0 < t \le 0.125s \\ s(t) = \cos(2\pi f_2 t) + \delta(t = 0.1875s) & 0.125s < t \le 0.25s \end{cases} \tag{3.21}$$

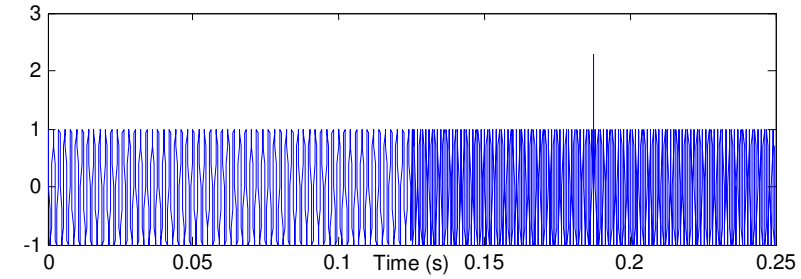

(a) Time domain signal

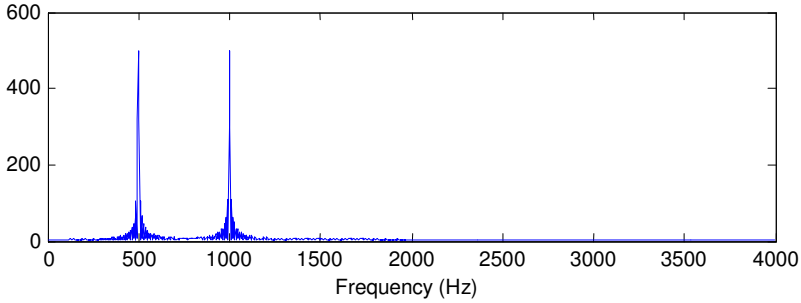

(b) Frequency spectrum

Figure 3.12: Example signal *s(t)*

This signal has been chosen in order to demonstrate the ability of the EMD to separate the different frequency components as well as to identify irregularities in a signal. The time domain representation of this signal along with its Fourier spectrum is given in the Figure 3.11. As expected, the two frequencies present in the signal show up in the Fourier spectrum unlike the spikes that remains undetectable for the FT.

3.3.2 EMD Analysis

The empirical mode decomposition is then applied to the signal. The first part of the EMD consists of extracting the intrinsic modes, as shown in the Figure 3.12.

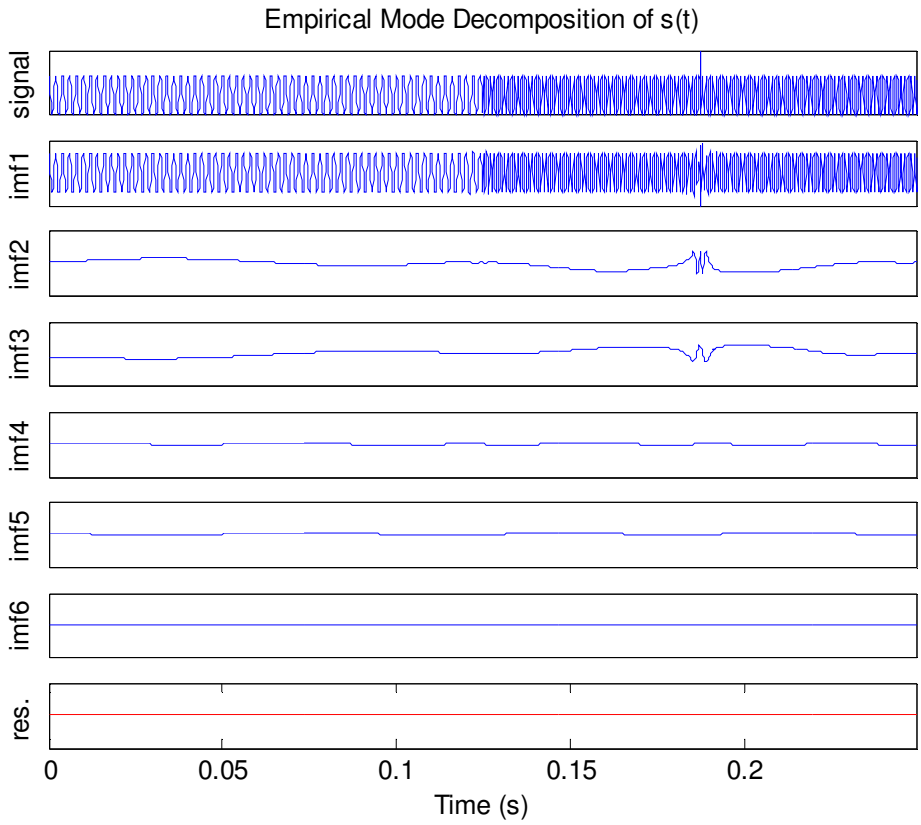

Figure 3.13: Empirical mode decomposition of *s(t)*

From this decomposition, we can notice that the first IMF is mainly composed of the two harmonic terms $f_1 = 1000Hz$ and $f_2 = 500Hz$ of the signal. The second and the third IMF are dedicated to the description of the spike. As one can see, only the irregularity is emphasized on these IMFs. The power of the EMD is thus shown through this example as it proved its ability to extract embedded and hidden feature in the signal. However, IMF#4, #5 and #6 appear to be meaningless in the analysis of this signal. Some more observations can be made. The way the EMD works can indeed be inferred. It turns out that the EMD picks out the highest frequency oscillation of the signal at each sifting iteration. Each IMF is symmetric with respect to its local mean, which guarantee to always get positive frequencies. The residue is a

monotonic function from which no more IMF can be extracted. The purpose of the sifting process was to obtain a set of functions that have well-behaved Hilbert transform. Hence, the second part of the Hilbert-Huang process is to take the Hilbert transform of each IMF and to deduct their meaningful instantaneous frequencies. It is now possible to represent the amplitude and the instantaneous frequency as functions of time in a three-dimensional plot, the Hilbert Huang spectrum (see Figure 3.14)

The empirical mode decomposition with the Hilbert-Huang spectrum gives a high-resolution time-frequency representation. The 2D plot provides fine details about the nature of the two sine waves as well as the impulse. The two frequencies can be accurately determined as well as their time duration. Both frequency and time resolutions are excellent. Moreover, there is little if any leakage at the frequency switch point. The impulse appears as a discontinuity in the frequency band. This can be compared to a discontinuity for a mathematical function. This discontinuity is well localized in time and is spread out over the whole frequency range. This makes sense as an impulse in the time domain theoretically contains all frequencies. All these details can be seen in the 3-dimensional plot in the Figure 3.13.

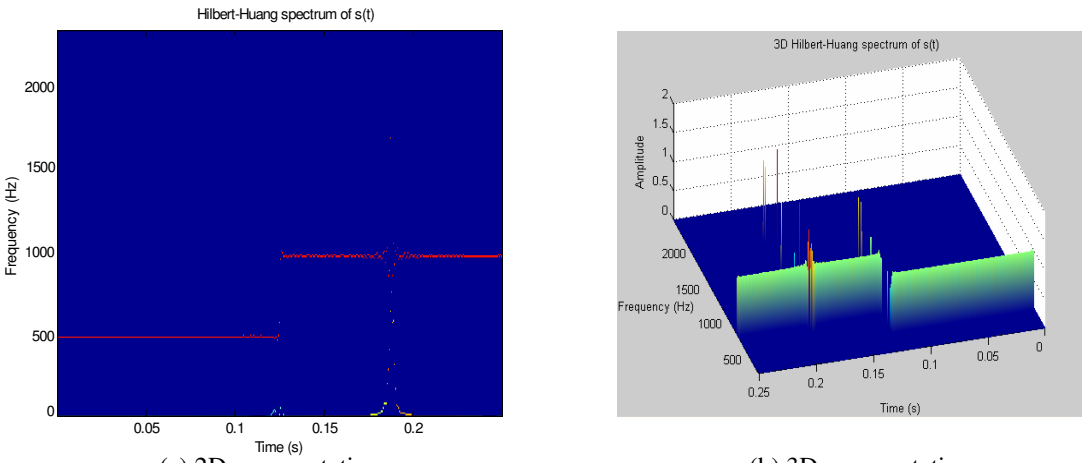

(a) 2D representation (b) 3D representation

Figure 3.14: Hilbert-Huang spectrum of *s(t)*

3.3.3 Comparison with the others time-frequency methods

After analyzing the signal $s(t)$ with the Hilbert-Huang transform, it is instructive to process the same signal through other time-frequency methods. A comparison with these methods will reveal the strengths and weaknesses of other time-frequency methods. The spectrogram of $s(t)$ corresponding to the STFT and the scalogram corresponding to the wavelet transform are plotted in the Figure 3.15. A random window size has been chosen for the Short-time Fourier transform, that is one fourth of the signal length. A large time window implies a good frequency resolution and a poor time resolution. Indeed, we can notice that the two frequency components are overlapping in time around the switch point.

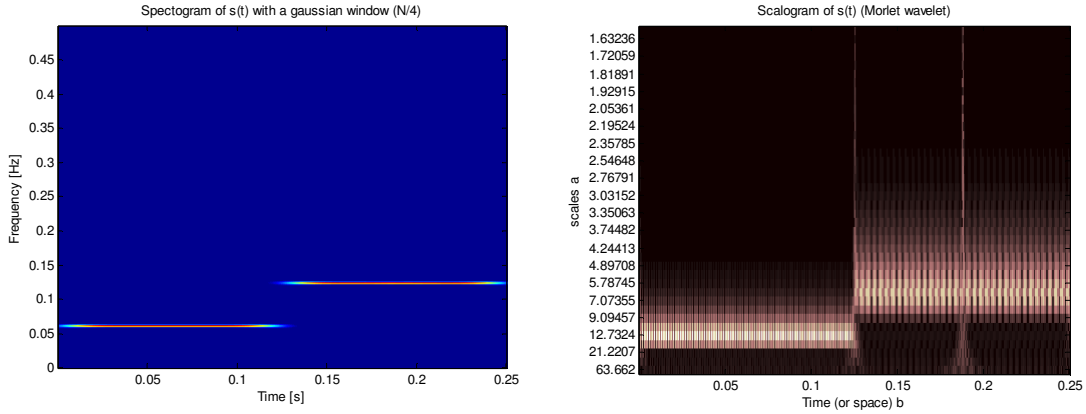

(a) Spectrogram (N/4) (b) Scalogram

Figure 3.15: Spectrogram and scalogram of *s(t)*

Hence, we could believe that both frequencies are present in the signal during a short time period, which is not true. Furthermore, the impulse does not appear in the spectrogram. The Gabor transform is not able to extract the presence of the impulse in the signal with this size of window. The main problem of the STFT is hence underlined. There is no guarantee that the window size adopted coincides with the

stationary time scales. The impulse event being very localized in time, a narrow window must therefore be applied. However, this choice implies a poor frequency resolution, as shown in the Figure 3.15.

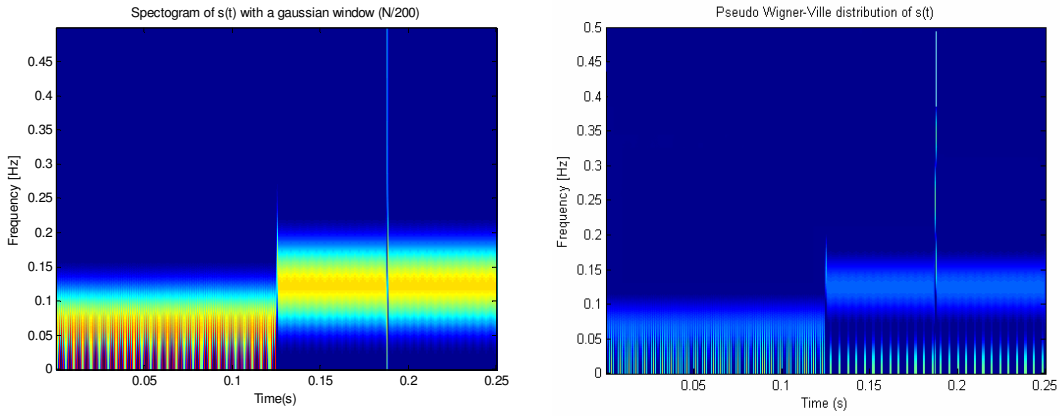

(a) Spectrogram (N/200)

(b) Pseudo Wigner-Ville distribution

Figure 3.16: Similarity between the STFT and the PWVD

The impulse can now be seen but the spectrogram gives now a smeared average frequency range over witch the main waves energies reside. The STFT turns out to be very limited compared to the Hilbert-Huang transform for the analysis of non-stationary data. Moreover, the pseudo Wigner-Ville distribution is plotted in the Figure 3.16. In order to get rid of the cross terms and interferences, the time-frequency representation has been modified by smoothing in time and frequency. The result is, then, basically that of the STFT analysis. The Wigner-Ville distribution therefore suffers all the limitations of the short-time Fourier transform.

The wavelet analysis is the best available non-stationary data analysis so far and turns out to be the big rival of the Hilbert-Huang transform for the supremacy of the

nonlinear and non-stationary signal analysis methods. The standard Morlet wavelet analysis identifies the local frequency before and after the frequency switch as well as the location of the frequency switch in the Figure 3.14. At the same time, the result also shows the leakage of the energy to the neighboring modes. In the Hilbert-Huang spectrum, we can see much sharper frequency definitions and the time location of the frequency switch than those shown in the scalogram. The range of variation is insignificant compared with the leakage in the wavelet analysis result. This suggests that the Hilbert-Huang transform is capable of providing a more crisp indication of the frequencies in the signal.

Another interesting observation is that the scalogram shows the smearing of the precise time location of the frequency switch event in the lower-frequency range. If we only look in the low-frequency range, we cannot tell the exact time of the impulse whereas it is well localized in the high-frequency range. More generally, to look for definition of a low-frequency event, we have to look at the high-frequency range in the wavelet spectrum. On the contrary, the energy of the impulse is well localized in both time and frequency domains in the Hilbert-Huamg spectrum. This illustrates the unique property of the Hilbert spectrum in elimination of the spurious harmonic components to represent the non-stationary data. Another strength of the Hilbert-Huang transform is its ability to resolve the intra-wave frequency modulation, while the wavelet can only describe the inter-wave frequency modulation. The analyzed signal $s(t)$ does not illustrate this property. Huang demonstrates it clearly through some examples [29].

3.3.4 Conclusion

This relatively simple example has been used to try to underline the strength as well as weaknesses of the wavelet transform, the short-time Fourier transform and the Hilbert-Huang transform. A comparative table summarizes the advantages and shortcomings of these different time-frequency methods.

	STFT	Wavelet	Hilbert-Huang
Strength	easy to implement	basis functions obtained by shifting and scaling a particular function	high time-frequency resolution
		uniform resolution	generalized Fourier analysis with variable amplitudes and frequencies
		analytic form for the result	first local and adaptive method in frequency-time analysis
		non-stationary data analysis	can clearly define both inter- and intrawave frequency modulations
		feature extraction	robust nonlinear and non-stationary data analysis
			feature extraction
Weakness	piecewise stationarity of the data assumption not always justified	uniformly poor resolution	end effects due to spline fitting and the Hilbert transform
	time-frequency resolution limited by the Heisenberg principle	leakage generated by the limited length of the basic wavelet function	cannot separete signals with very close frequencies
	non-adaptive nature	non-adaptive nature	no physical meaning of some IMFs
	feature extraction impossible	cannot resolve intrawave frequency modulation	no mathematical formulation
		high-frequency range observation to define local events	

Table 3.1: Strength and weaknesses of the STFT, the wavelet transform and the HHT

The STFT seems to be limited compared to the wavelet and the HHT in the analysis of nonlinear and non-stationary signals. The wavelet transform has been the best available non-stationary data analysis before the introduction of the Hilbert-Huang transform. However, the analysis of the signal $s(t)$ has proven that the HHT offers a better time and frequency resolutions than the wavelet transform and allows a better physical interpretation of the signal content. The Hilbert-Huang transform turns out to be a new revolutionary nonlinear and non-stationary signal data analysis method.

3.5 Summary

The combination of the empirical mode decomposition and the associated Hilbert spectral analysis has proven to be versatile and robust in analysis of nonlinear and non-stationary data. Central to the present approach is the sifting process to produce the intrinsic modes that enables complicated data to be reduced into such a structure that the instantaneous frequencies are meaningful. The expansion in terms of IMF basis has the form of a generalized Fourier analysis with variable amplitudes and frequencies. The application of the Hilbert transform on the extracted IMFs allows the creation of an energy-time-frequency representation, the Hilbert-Huang spectrum, characterized by a high time and frequency resolutions. However some problems related to its implementation still exist and need attention. The spline fitting has overshoot and undershoot problems, the criteria in the sifting process needs to be selected judiciously and the end effects need more improvements. The EMD combined with the Hilbert spectral analysis has offered a powerful method for nonlinear and non-stationary data analysis. It is the first local and adaptive method in time-frequency analysis

Chapter 4

EMD Metrics For Damage Detection

From the previous chapters, the empirical mode decomposition with its associated Hilbert spectral analysis has shown promising results in the analysis of time-series data. This great potential could be applied to help the diagnosis and the prognosis of aerospace structures. The structural health monitoring aims at developing a damage identification method that provides complete damage information. Rytter [51] proposed a system of classification for damage-identification techniques, which defined four levels of damage identification. The presence of damage, its location, its size and the prediction of the remaining service life of the structure are the different hierarchical goals to reach for any damage detection scheme. A metric is the key tool to infer the size of the damage. From the measurement of a specific physical property of the structure (damping, stiffness, energy…), a metric will give the necessary information to quantify the severity of the damage. This chapter is therefore dedicated to the investigation of the Hilbert-Huang transform features that could be used to obtain robust and efficient metrics for damage detection in isotropic and composite structures.

4.1 The Hilbert instantaneous phase

Some researchers has recently suggested exploiting instantaneous phase features of the vibration signals combined with wave mechanics based concepts for damage detection [34,52]. Compared to the others time-frequency methods, the Hilbert

instantaneous phase is a unique feature that describes the traveling structural wave propagation. Pines and al. [34] have indeed proved the dependency of the phase on the structural parameters as stiffness, mass and damping. The Hilbert instantaneous phase turns therefore out to be an interesting feature to investigate in our quest for damage detection metrics.

4.1.1 Description

As seen in section 3.1.1, the Hilbert transform of a real-valued time-domain signal $x(t)$ is another real-valued time-domain signal, denoted by $H[x(t)]$, such that $z(t) = x(t) + iH[x(t)]$ is an analytic signal, where

$$H[x(t)] = \frac{1}{\pi} \int_{-\infty}^{\infty} \frac{x(u)}{t-u} du \tag{4.1}$$

We can define an envelope function $a(t)$ describing the instantaneous amplitudes of the original signal $x(t)$ and a phase function $\theta(t)$ describing the instantaneous phase of $x(t)$ versus time using $z(t) = x(t) + iH[x(t)] = a(t)e^{i\theta(t)}$. These instantaneous parameters are hence defined as,

$$a(t) = [x(t)^2 + H[x(t)]^2]^{1/2} \text{ and } \theta(t) = \arctan\left(\frac{H[x(t)]}{x(t)}\right) \tag{4.2}$$

The instantaneous Hilbert phase is therefore defined for the real-valued time-domain signal $x(t)$ in Equation (4.2). However, in the purpose of our research, the signal $x(t)$ is first processed through the empirical mode decomposition in order to get the intrinsic modes (IMFs), which admit well-behaved Hilbert transform. The signal $x(t)$ is thus decomposed into n empirical modes $c_i(t)$ and can be expressed as,

$$x(t) = \sum_{i=1}^{n} c_i(t) \tag{4.3}$$

The residue, which is a mean trend, has been left out on purpose. Then the Hilbert transform is applied to each IMF and produces the instantaneous phase as functions of time,

$$\theta_i(t) = \arctan\left(\frac{H\left[c_i(t)\right]}{c_i(t)}\right) \tag{4.4}$$

The total instantaneous phase is the sum of the instantaneous phases corresponding to each IMF and is defined as,

$$\theta(t) = \sum_{i=1}^{n} \arctan\left(\frac{H\left[c_i(t)\right]}{c_i(t)}\right) \tag{4.5}$$

Because the intrinsic modes have been restricted to be symmetrically local with respect to the mean zero level, the phase can be considered to be local and to increase monotonically as a function of time. The instantaneous frequencies are derived in taking the derivative of the phase and hence need the continuity of this one. Computing the unwrapped phase instead preserves this continuity. The phase function is not restricted anymore to an interval of length 2π and increases monotonically. An example of the unwrapped phase is given in Figure 4.1 along with its corresponding time-domain signal.

The unwrapped instantaneous Hilbert phase has been therefore defined and needs now to be investigated as a potential damage detection tool.

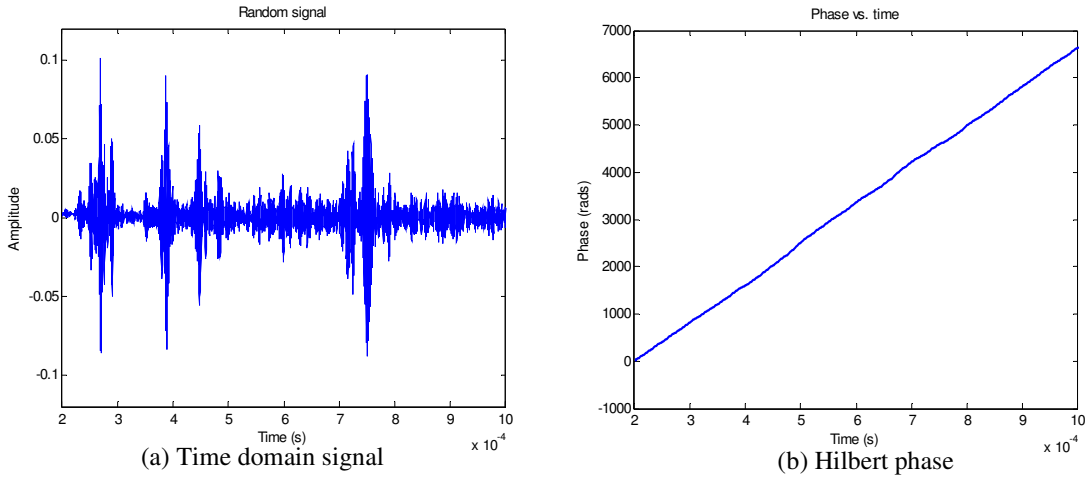

(a) Time domain signal (b) Hilbert phase

Figure 4.1: Hilbert phase example

4.1.2 1D finite element simulation

Before computing the phase for real undamaged and damaged data, a finite element model has been simulated in order to understand how the instantaneous phase can be used to detect damage in structures. A dynamic finite element model of a clamped-free rod was created in order to simulate the 1D wave propagation. Damage was introduced by a loss of stiffness in an element and the excitation input was a sine burst signal. The simulation results are then processed through the EMD and the phases for the undamaged case and the damaged case are then computed and compared.

4.1.2.1 Governing equation for a thin rod

Let us review very quickly the governing equation of a rod and the basic wave propagation characteristics. Consider a straight rod as shown in the Figure 4.2 along with the free body diagram of a differential element.

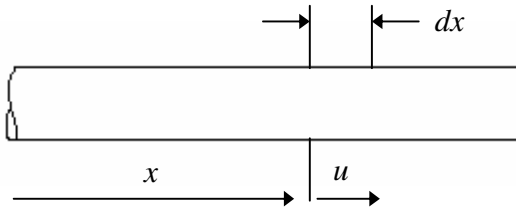

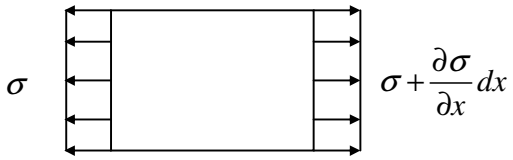

x is to the cross section of the rod
A is the cross-sectional area
u is the longitudinal displacement
σ is the stress field

Figure 4.2: Thin longitudinal rod

Assuming that there is no body force, the equation of motion in the x direction becomes:

$$-\sigma A+\left(\sigma+\frac{\partial\sigma}{\partial x}dx\right)A=\rho A dx\frac{\partial^2 u}{\partial t^2} \tag{4.6}$$

that reduces to

$$\frac{\partial\sigma}{\partial x}=\rho\frac{\partial^2 u}{\partial t^2} \tag{4.7}$$

We now assume that the material follows the Hooke's law $\sigma = E\varepsilon$ where E is the Young's modulus and ε the axial strain. We obtain for a homogeneous rod (E and ρ are constant) the following equation of motion,

$$E\frac{\partial^2 u}{\partial x^2}=\rho\frac{\partial^2 u}{\partial t^2} \tag{4.8}$$

From the familiar wave equation $\frac{\partial^2 u}{\partial x^2}=\frac{1}{c_0^2}\frac{\partial^2 u}{\partial t^2}$, we deduct the wave propagation speed in a longitudinal thin rod, that is $c_0=\sqrt{\frac{E}{\rho}}$. (4.9)

4.1.2.2 Finite element formulation

We want to describe the wave propagation as a function of time in a rod. The most widely used formulation to determine the transient response of a structure is the finite element method where a structure is discretized into elements in which the potential and kinetic energies are formulated. Using variational mechanics, the variation of the difference between the kinetic and the potential energy gives rise to a second order differential equation which describes the structure's dynamics, $M\ddot{q} + Kq = F$. Where M and K are the mass and stiffness matrices, F is the applied force and q is the vector of nodal degrees of freedom. The transient response is then obtained in replacing the time derivative in the equation of motion by finite difference approximations.

A rod can only carry axial load. The basic finite element is shown in the Figure 4.3 and is a two-node element that can be obtained from the exact solution for a rod with constant properties along its axis and pure nodal loading.

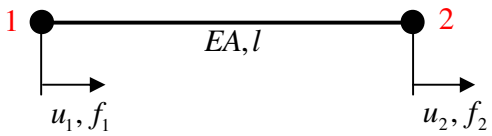

Figure 4.3: Two-node element

The element stiffness matrix and the element mass matrix are the well-known matrices

$$Ke = \frac{EA}{l}\begin{bmatrix} 1 & -1 \\ -1 & 1 \end{bmatrix} \quad \text{and} \quad Me = \rho Al\begin{bmatrix} 1 & 0 \\ 0 & 1 \end{bmatrix} \tag{4.10}$$

The number of elements chosen turns out to be an important parameter in the wave propagation. To describe the wave propagation via the finite element model, the wavelength of the excitation signal has to be taken into account. A number of three elements per wavelength is a good approximation. For aluminum rod and an excitation burst at $10\,kHz$ frequency, the wave speed is given by $c = \sqrt{\frac{E}{\rho}} \cong 5100\ m/s$ and the wavelength is $\lambda = \frac{c}{f} \cong 0.5\ m$. From these calculations and in order to get clear signals, a long rod of $30m$ with a mesh of 400 elements has been created as shown in the Figure 4.4.

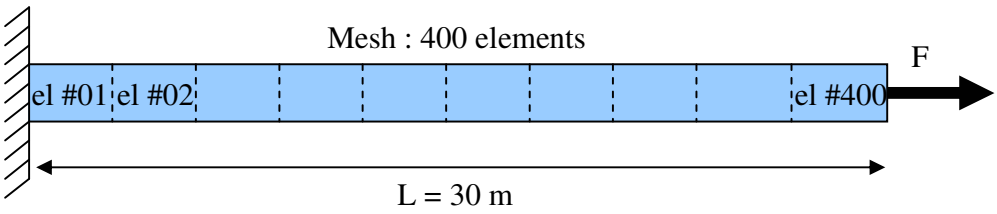

Figure 4.4: Meshing of the rod model

After the assembly of the global stiffness and mass matrices, the equation of motion $M\ddot{q} + Kq = F$ becomes,

$$\rho Al \begin{bmatrix} 1 & 0 & & & \\ 0 & 2 & 0 & & \\ & 0 & 2 & \dots & \\ & & \dots & \dots & \dots \\ & & & \dots & 1 \end{bmatrix}_{401*401} \ddot{q} + \frac{EA}{l} \begin{bmatrix} 1 & -1 & & & \\ -1 & 2 & -1 & & \\ & -1 & 2 & \dots & \\ & & \dots & \dots & \dots \\ & & & \dots & 1 \end{bmatrix}_{401*401} q = f(t) \begin{bmatrix} 0 \\ 0 \\ \dots \\ \dots \\ 1 \end{bmatrix}_{401*1} \quad (4.11)$$

Once the boundary conditions are applied and the forcing actuation is set, the transient analysis can start. The more general methods for transient analysis are based on replacing the time derivative in the equation of motion by finite difference

approximations. The most widely used methods are implicit methods like the Newmark method. They lead to an incremental, time stepping algorithm. The transient vibration of a rod can be simulated to view its wave propagation properties.

4.1.3 Simulation results

First, we wish to analyze the response of an undamaged rod to a transient load. The problem will be that of a rod, fixed at $x = 0$ and subjected to a transient load $f(t)$ at $x = L = 30m$. The goal of the dynamic FEM simulation is to plot the variation of the displacement $u(x,t)$ with time for any x along the rod. For the present study case, the transient load will be a sine burst at 10 kHz frequency applied at the tip and the displacement at $x = 22.5m$ will be evaluated as shown in the Figure 4.5.

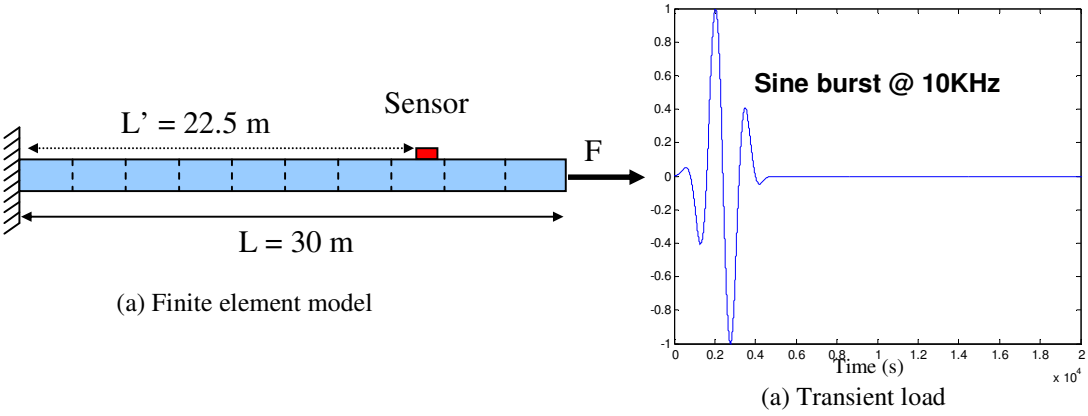

(a) Finite element model

(a) Transient load

Figure 4.5: Forced vibrations model of a rod

The wave-propagation solution of this kind of problem is very well known and can be found in Graff's book [53]. Waves in a rod are non-dispersive. This means that their speed of propagation is constant, independent of frequency as seen in Equation (4.9). The mathematical resolution of the wave-propagation is therefore facilitated and the reflection from boundaries can be mathematically predicted. As shown in Graff's

book [53], we will have a displacement reversal at the fixed boundary. This statement can be verified by the result of the simulation as seen in Figure 4.6.

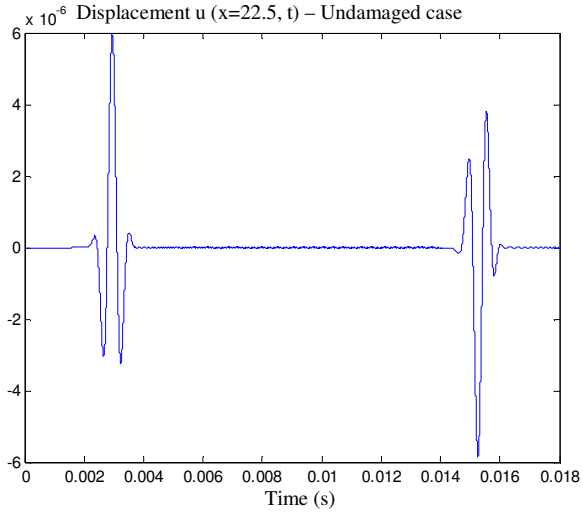

Figure 4.6: Response of an undamaged clamped-free rod to a transient load

The sensor detects at first the traveling wave generated by the tip excitation. The reflection from the clamped boundary is identified later and is reversed as predicted by the wave propagation theory in a rod. The wave propagation in the undamaged rod is depicted in the Figure 4.6.

Reflections of waves may occur at discontinuities other than a boundary condition. One way to simulate damage in a computational model is to create a discontinuity in cross-section, or material properties, or both, which is commonly referred to as an impedance change. A loss of stiffness in an element is hence introduced in the model, resulting in a damaged rod. The situation is shown in the Figure 4.7.

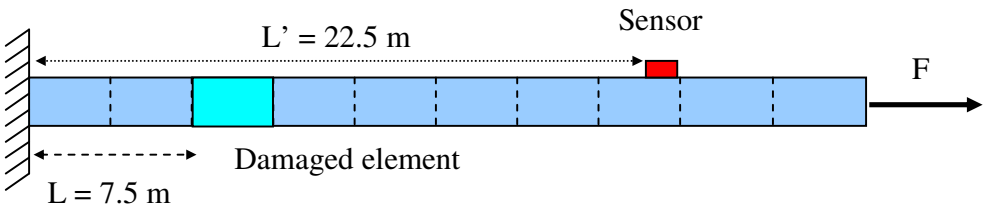

Figure 4.7: Damaged rod finite element model

Two damaged models have been created to introduce a loss of stiffness in the element located at $x = 7.5m$ such that (i) $E_{dam} = \frac{E_{und}}{2}$ for the first case and (ii) $E_{dam} = \frac{E_{und}}{4}$ for the second case. Both wave-propagation simulation results are plotted in the Figure 4.8.

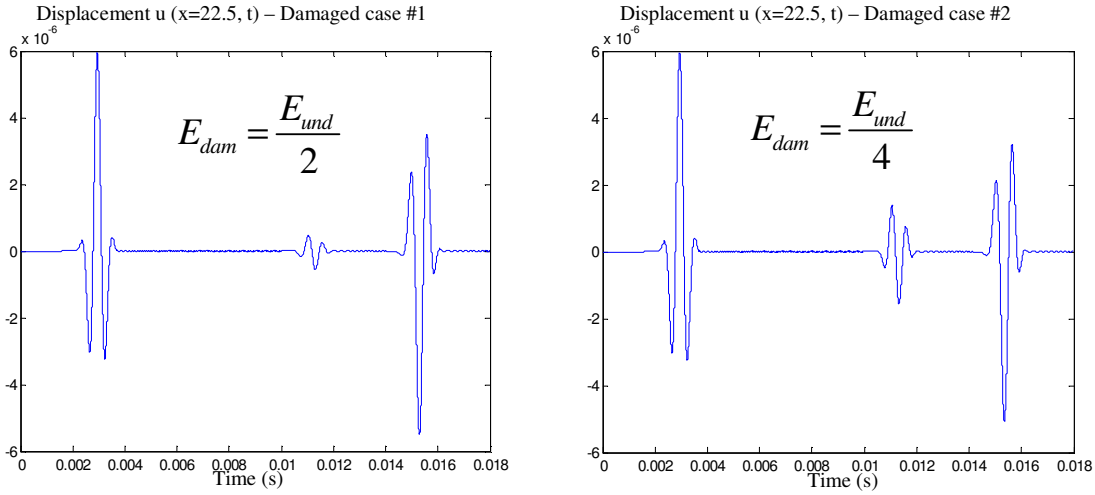

(a) Damaged case #01 (b) Damaged case #02

Figure 4.8: Response of a damaged clamped-free rod to a transient load

The reflections from the damage and the edge are clearly visible. The amplitude of these reflections increases with an increase in loss of stiffness in the element. A larger damage releases more energy in the structure, implying a greater magnitude in the waveform reflection.

A hamming window is applied in order to smooth the ends of the data to eliminate some aberrations and to allow a better spline interpolation in the EMD algorithm.

The empirical mode decomposition along with the Hilbert transform can now be applied to these signals and the phase computed. The result for the Hilbert phase of the undamaged case and the damaged case is represented in the Figure 4.9.

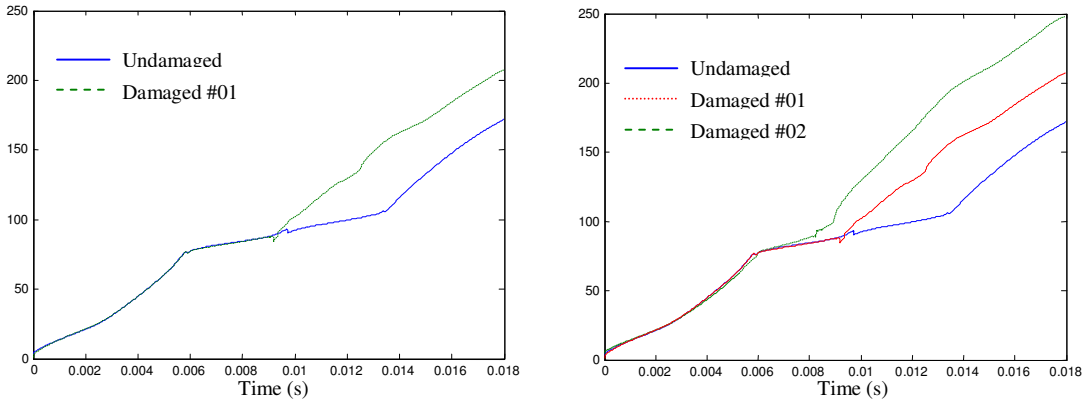

(a) Damaged case #01

(b) Damaged case #02

Figure 4.9: Hilbert phase

From this plot, we can conclude that the reflection from the damage is interpreted by a slope change in the Hilbert phase. Physically, any damage in a structure alters the speed at which the energy traverses the structure. Once the wave passed through the damage, the energy speed is no more affected and the Hilbert phase behaves in the same manner for both undamaged and damaged cases as depicted in the Figure 4.9. Furthermore, the slope change appears to be dependent on the size of the damage as seen in the Figure 4.9. The energy speed propagation would be therefore altered in a different way depending on the size of the damage. This implies that one can track increasing amount of damage as a function of phase. Thus, the Hilbert phase allows the size and location of damage to be determined.

Even if the simulation results are not perfect and could be improved by augmenting the meshing and discretizing the rod by more elements, the damages are clearly localized by the slope change of the Hilbert phase.

4.2 The energy metric

One of the main advantages of the Hilbert-Huang transform is to provide a high-resolution energy time-frequency representation. The Hilbert spectrum is capable of describing with high precision the frequency content of any nonstationary and non-linear signals. The different features embedded in the time-domain signal can therefore be highlighted and better understood. For these reasons, the energy time-frequency plot provided by the HHT could be used to identify and assess structural damage. A Hilbert energy spectrum describing the wave energy density can be created and the severity of the damage inferred from the reflected energy.

4.2.1 Wave and energy

A wave can be described as a disturbance, which travels through a medium, transporting energy from one location (its source) to another location without transporting matter. Each individual particle of the medium is temporarily displaced and then returns to its original equilibrium position [54]. Consequently a wave is an energy transport phenomenon, which transports energy along a medium without transporting matter. The amount of energy carried by a wave is related to the amplitude of the wave. A high-energy wave is characterized by high amplitude; a low energy wave is characterized by low amplitude.

4.2.2 The Hilbert spectrum and the reflected energy

As seen earlier, after applying the EMD and the Hilbert transform on the IMFs, a real signal $x(t)$ can be expressed as $x(t) = \sum_{j=1}^{n} a_j(t) * \exp\left(i \int \omega_j(t) dt\right)$ where $a_j(t)$ are the instantaneous amplitudes and $\omega_j(t)$ are the corresponding instantaneous frequencies. Because both amplitude and frequency of each IMF is a function of time, they can define a three-dimensional space or ordered triplet $[t, \omega(t), a(t)]$. This space is generalized by means of a function of two variables $H(\omega, t)$ to $[t, \omega(t), H(\omega, t)]$, where $a(t) = H(\omega(t), t)$. Therefore we obtain a three-dimensional plot, in which the amplitude can be contoured on the frequency-time plane. As mentioned previously, the amount of energy carried by a wave is related to its amplitude. This transported energy is directly proportional to the square of the amplitude of the wave. Thus, the squared values of amplitude can be substituted in the Hilbert spectrum to represent the energy density and to produce the Hilbert energy spectrum. The idea behind this is that any reflection from a damage can be quantitatively estimated through the energy transported by the reflected wave. It has been shown in the previous section that the amplitude of the reflection increases with the size of the damage. This increase in amplitude should be revealed locally in the energy-time-frequency representation. We can therefore expect to infer the size of the damage through the Hilbert energy spectrum. The next section illustrates the use of the energy density spectrum for detecting and evaluating damage.

4.2.3 The Hilbert-Huang spectrum as a damage detection parameter

Let us apply the Hilbert-Huang transform to a progressively damaged structure and plot the corresponding Hilbert energy spectrum. The baseline signal and three different damage cases are plotted in the Figure 4.10.

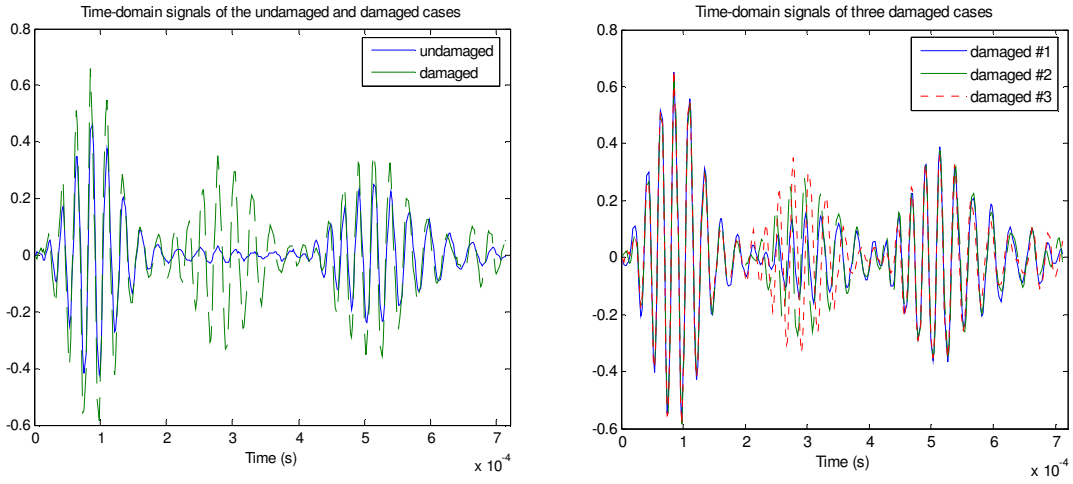

Figure 4.10: Baseline signals of a progressively damaged structure

The reflection from the damage can clearly be seen in the time-domain signals. As the damage becomes bigger, the amplitude of the reflection increases as shown in the Figure 4.10. The values of the instantaneous amplitudes provided by the Hilbert transform of each IMF are squared and the energy density for each of these signals are plotted in the Figure 4.11.

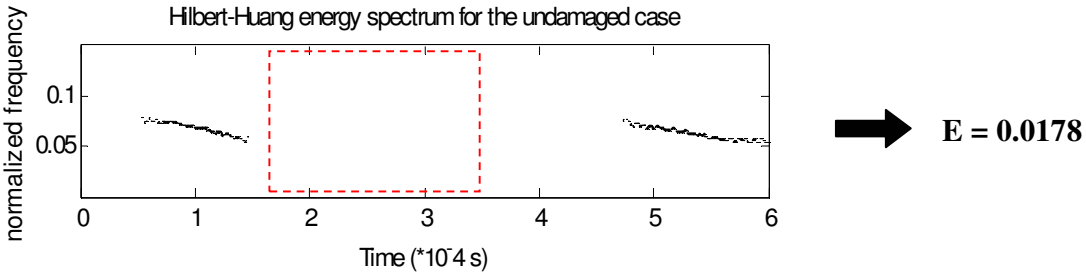

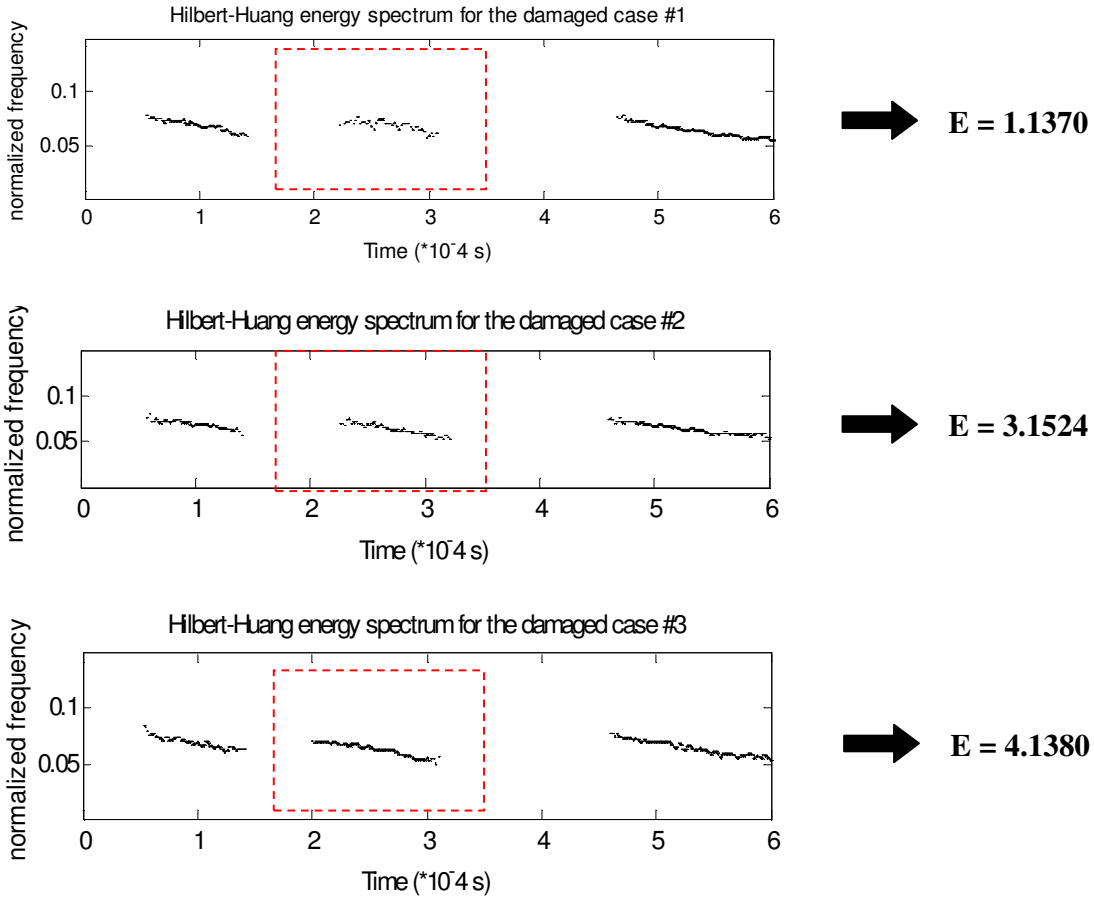

Figure 4.11: Hilbert-Huang energy spectra

These Hilbert energy spectra reflect the observations made for the time-domain signals. The damage is described by a frequency band well localized in time and the energy of the reflected waveform is quantified by the squared value of the amplitude. The plots clearly show a variation of the reflected energy with the amount of damage. Thus a damage index can be introduced in order to quantify the severity of the damage as a function of reflected energy,

$$E = \sum_{f}\sum_{t}\left|H_e(t,f)\right| = \sum_{f}\sum_{t}\left|a(t)^2\right| \qquad (4.12)$$

where $H_e(t, f)$ is the energy density spectrum and $a(t)$ is the instantaneous amplitude.

This damage index is applied to the red dashed window part of the spectrum, corresponding to the reflected waveform from the damage, and the result is displayed next to each spectrum. As expected, this damage index increases with the size of the damage and a trend could be interpolated to infer the increasing damage.

The analysis of this damaged structure is facilitated by clear time-domain signals. The reflection from the damage is visible without any data pre-processing. In general, reflections from boundaries and other discontinuities will be difficult to identify. The empirical mode decomposition serves this purpose. The ability of the EMD to decompose any complicated data into a set of simple oscillatory functions would allow extracting embedded reflections.

To summarize, the objective is first to extract signal structures embedded in the data. The empirical mode decomposition is therefore the fundamental key to reveal the damage signatures that may otherwise remain hidden. The next step is to create the Hilbert energy spectrum for both undamaged and damaged cases. At this point, the energy density representation accurately describes the wave propagation in the structure. The presence of damage can hence be inferred and an estimation of the size predicted through the amount of reflected energy.

The Hilbert-Huang spectrum can also be a useful tool to describe at the first sight the shape of a structure. The high-resolution time-frequency description of a signal's content allows a better understanding of the physics hidden in the data. A simple experiment of an aluminum beam with a crack milled into it is significant. The depth of the crack is half the thickness of the beam and the acquisition of the data is done with a strain gage. The Hilbert spectra for the undamaged case and the damaged case are plotted in Figure 4.12.

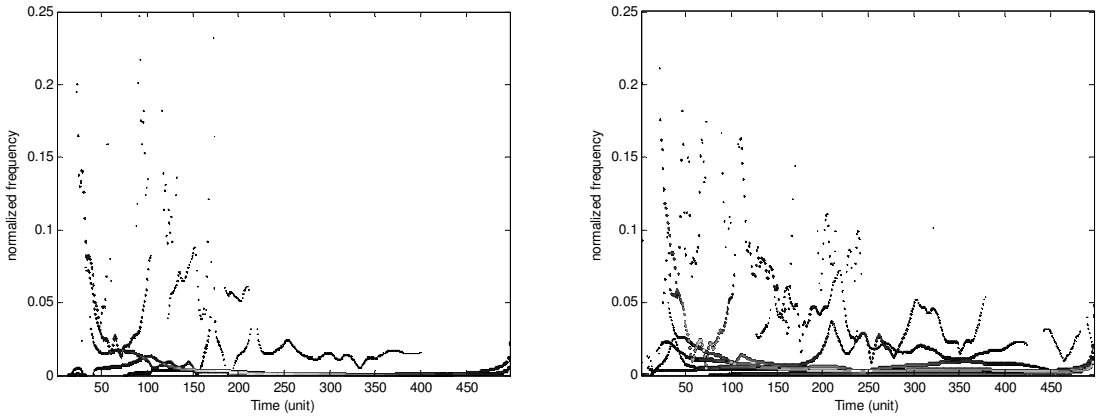

(a) Undamaged (b) Crack milled into the beam

Figure 4.12: Hilbert-Huang spectra of an aluminum beam

A quick look at the plots allows one to determine that the beam is damaged. The damage introduced into the beam creates additional harmonics in the amplitude spectrum of the strain energy that have not been present in the undamaged beam. This simple observation of the spectrum can be used for small parts of structure that cannot be fixed and that need to be replaced if damaged.

4.3 The phase shift metric

The high frequency and energy definitions provided by the HHT are used in the previous section to locate and infer the size of a damage. Another interesting parameter to investigate is the high time resolution of the Hilbert-Huang spectrum. The time of flight is an important feature that is often used in damage detection schemes. The time of flight between the actuator and sensor in a structure is directly dependent on the wave propagation properties in the structure.

The time resolution is therefore explored to obtain an accurate time of flight and consequently a precise position of the structural discontinuity. The track of increasing damage would be also possible as long as the initial size of the damage is known.

4.3.1 Principle

A wave propagates at a certain speed in a structure. The time difference between the initial sensing actuation and the reflection from a discontinuity gives the time needed for the wave to travel. The basic formula $length = speed * time$ locates the damage. When a wave encounters a damage, part of the incident wavefront is reflected back while the rest is transmitted through the damaged region. This reflection occurs at the beginning of the damage, which implies that a bigger damage would engender a sooner reflection than a smaller damage located at the same position. Hence, the times of flight would be different for damages with different sizes at the same location as shown in the Figure 4.13. Thus, if the time resolution of the HHT is powerful enough to perceive the small fluctuations of the different times of flight, an estimation of the severity of the damage would be possible.

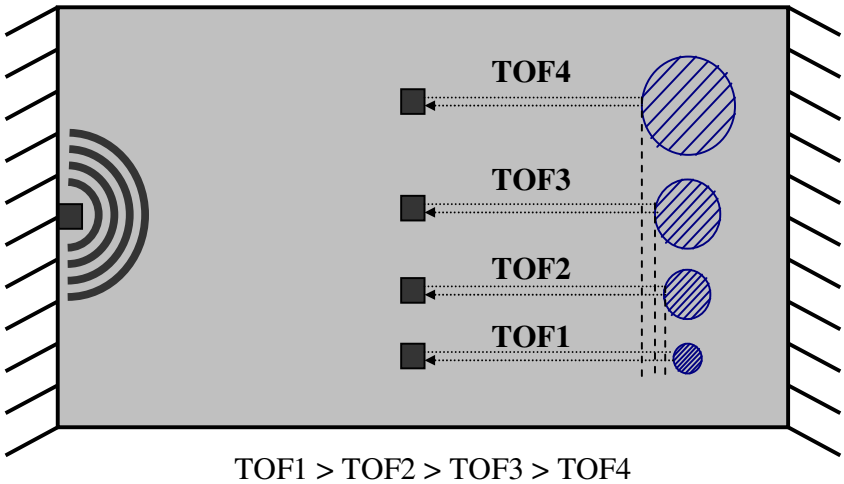

TOF1 > TOF2 > TOF3 > TOF4

Figure 4.13: Variations of the time of flight with the size of damage

4.3.2 Application

In order to demonstrate the ability of the Hilbert spectrum to accurately describe the wave temporal propagation, an energy-time plot for the progressively damaged structure of the previous section is created in the Figure 4.14.

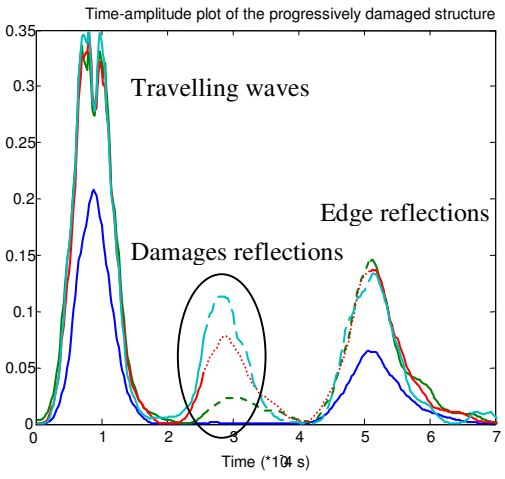

(a) Energy-time spectrum

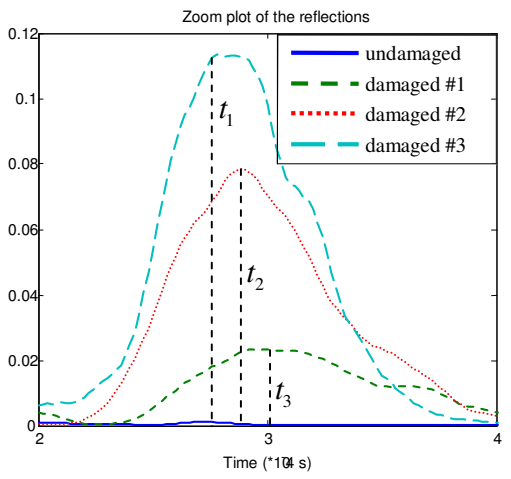

(b) Portion of signal corresponding to reflection

Figure 4.14: Energy-time spectrum of a progressively damaged structure

As we can see in the Figure 4.14, the amplitude peaks corresponding to the damages reflections are shifted in time. This is even more visible on the zoom plot of the reflections. From the different times of arrival, we can formulate a first qualitatively conclusion about the size of the damages. The damage corresponding to the arrival time t_1 turns out to be the biggest one, as the wave needs less time to travel from the sensor to the damage. Assuming that the size and the shape of the initial damage are known, simple geometric calculations would allow to estimate the growth of the damage from the time difference between the initial and the new reflections. The severity of the damage can be thus quantified through the arrival time of the reflection as long as the initial damage is identified. From the observation of the Figure 4.14, we can also notice that the amplitude of the reflections increases with the size of the damage, which makes sense with the previous theories.

Hence, the importance of an accurate signal processing for obtaining the flight times cannot be over-emphasized. Accurate identification of localized events is required to determine the location of the damage, especially when complications due to the dispersive nature of waves in plates will exist.

4.4 Summary

The empirical mode decomposition and the Hilbert spectrum offer a lot of possibilities for damage detection. First of all, the Hilbert phase represents a unique feature describing the energy propagation in a structure. The Hilbert phase as a damage detection parameter seems to work pretty well for one-dimensional models with non-dispersive wave propagation. The presence of damage is interpreted by a slope change in the Hilbert phase plot, which corresponds to a modification of the

speed at which the energy traverses the structure. The finite element simulation as well as the civil building model analysis by Pines and Salvino [34] has shown promising results in the detection and evaluation of structural damage. Second of all, the energy metric relies on the high energy-time-frequency resolution of the Hilbert spectrum. This metric listens to the energy release in the structure upon defect growth. The amount of reflected energy is described and quantified with the Hilbert energy spectrum and an estimation of the severity of the damage can be deduced. Finally, a phase shift metric is developed based on the arrival times of reflected waves from damage. Depending on the size of the damage, the wave will need a certain time to travel. This time of flight can be exploited along with geometric considerations to determine the defect growth from the knowledge of the initial damage properties.

Hence, the EMD along with the Hilbert transform seems to be the appropriate time-frequency analysis method for health monitoring of structures. The ability of the empirical mode decomposition to extract embedded oscillation, to reveal hidden reflections in the data and to accurately describe the frequency content of a signal through the high-definition Hilbert spectrum make it an ideal tool for damage detection. The different damage detection schemes developed in this chapter must now be investigated to two-dimensional isotropic and composite plate structures where the waves are dispersive and thus more complicated to describe.

Chapter 5

Damage Detection In Isotropic Plates

5.1 Introduction

For thin plates, wave propagation is described using Lamb waves. Lamb waves are dispersive plate waves that occur for traction-free forces on both surface of the plate. In this chapter, a description of Lamb waves and their properties is discussed. The interaction of these waves with a damaged region changes the way the waves propagate. Part of the incident wavefront is reflected back while the rest is transmitted through the damaged region. The presence of the reflected waves indicates that damage is present in the structure. The generation of Lamb waves in the plate is carried out through the excitation of a piezoceramic actuator. This actuation element actively interrogates the plate and the response signals are gathered with a sensor array made from a piezoelectric sheet. Reflections from damage can then be extracted from sensor signals in an effort to locate a damage region. Damage in the form of holes in an isotropic plate is examined. The experimental setup used in this work was developed by Purekar for his doctoral research [39]. The energy and the phase shift metrics, described in Chapter 4, are applied on data sets obtained from exciting waves in isotropic plates. These techniques are used to show that the location of the hole can be determined as well as trends indicating that the size can be inferred. These damage

detection schemes are facilitated by the isotropic nature of the plate. The Lamb wave propagation is indeed well described in isotropic plate structures.

5.2 Basic wave mechanics

Before describing Lamb wave propagation in plates, fundamental notions on wave mechanics need to be recalled [53]. A propagating wave is characterized by a spatial frequency, k, as well as a temporal frequency, ω. The wavenumber is the spatial frequency of a wave. The distance between two successive points of constant phase is the wavelength and is defined from the corresponding wavenumber as $\lambda = \frac{2\pi}{k}$. A wave propagating in one direction is commonly described by $e^{i(\pm kx+\omega t)}$, the sign of the wavenumber indicating the direction of travel. The propagation velocity of the constant phase is $c_p = \frac{\omega}{k}$, defined as the phase speed. A group of waves corresponding to a band of frequencies will travel at a speed which may be different than the phase speed. This group speed happens to be the local slope of the frequency-wavenumber relationship and is defined as $c_g = \frac{\partial \omega}{\partial k}(\bar{\omega})$ for a group of waves centered around the frequency $\bar{\omega}$. The relationship between the wavenumber and the temporal frequency describes the way the waves propagate. If this relation is linear, then the phase speed is constant. The shape of the wave would be the same as the wave propagates through the structure. These types of waves are called non-dispersive waves. However, when the wavenumber-frequency relationship is not linear, the frequency components of the wave signal will travel at different speeds and the wave form will not maintain its shape. These types of waves are called dispersive

and are much more complicated to study. The wavenumber turns out to be a crucial parameter in the wave propagation since it describes not only the spatial distribution of the wave but also leads to the wave propagation speed in a medium. The wavenumber-frequency relationships for a thin isotropic plate are shown to be [39]:

$$\text{transverse vibration:} \quad k = \sqrt{\omega}\sqrt[4]{\frac{m}{D}} \tag{5.1}$$

$$\text{in-plane vibrations:} \quad k = \pm\omega\sqrt{\frac{\rho}{E}}\sqrt{1-\upsilon^2} \tag{5.2}$$

where m is the mass per area of the plate and D the rigidity of the plate. The wavenumber-frequency relationship is therefore non linear in the case of transverse vibration of a thin plate and linear in the case of in-plane vibrations. These relationships hold for cases where the thickness of a plate is a lot smaller than the wavelength of the wave and assuming no shear deformation. A more general description of the wave propagation properties needs to take into account shear deformation and is given by the Lamb wave theory.

5.3 Lamb wave propagation in isotropic plates

5.3.1 Lamb wave for damage detection

Guided waves are able to interact with defects in structures due to their propagation properties that are highly sensitive to any discontinuities in materials. The interaction of Lamb waves with defects on plates has been investigated best by Alleyne and Cawley [55]. Giurgiutiu, et. al. [56] conducted numerical and experimental studies of reflections of Lamb modes from cracks in an aluminum plate. A damage index based

on the scattering information of Lamb waves interactions with a crack was developed by Ihn and Chang [15]. Because Lamb waves travel long distances and can be applied with conformable PZT actuators, they are suitable for online structural health monitoring. Lamb waves are the most widely used guided ultrasonic waves for structural damage detection.

5.3.2 Theory of Lamb wave propagation

Lamb waves refer to elastic perturbations propagating in a solid plate with free boundaries and with a thickness of the order of a wavelength or so. These two-dimensional propagating vibrations in a plate are described by mathematical equations formulated by Horace Lamb in 1917 [57]. There are two groups of propagation modes according to their displacement pattern, the symmetric waves and the anti-symmetric waves, that satisfy the wave equation and the boundary conditions. A graphical representation of these two groups of waves can be seen in Figure 5.1. For a given plate thickness d and acoustic frequency f, there exists a finite number of propagation modes specified by their phase velocities. The velocities of these waves depend on the frequency and the thickness of the plate. A complete description of propagation characteristics for plates is normally given in the form of a set of dispersion curves, illustrating the plate-mode phase velocity as a function of the frequency-thickness product. Each curve represents a specific mode, which is conventionally called A_0, S_0, A_1, S_1, A_2, S_2, etc. where A_n denotes anti-symmetric modes and S_n symmetric modes.

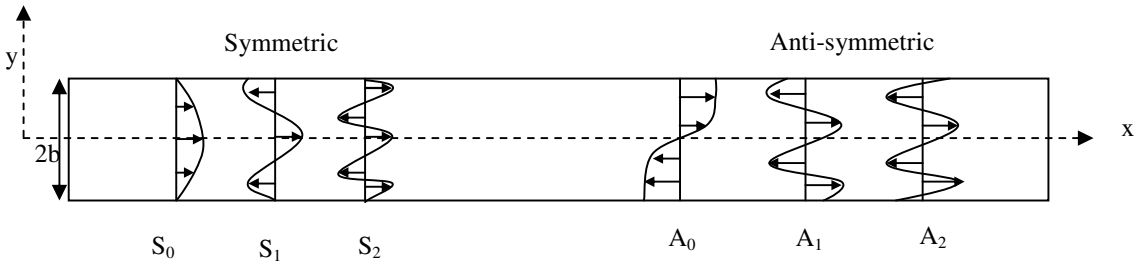

Figure 5.1: Graphical representation of the symmetric and anti-symmetric waves

The method of potential is the most common approach for solving the Lamb wave problem. Let us consider a thin plate bounded by two parallel planes a distance $2d$ apart as shown in the Figure 5.2.

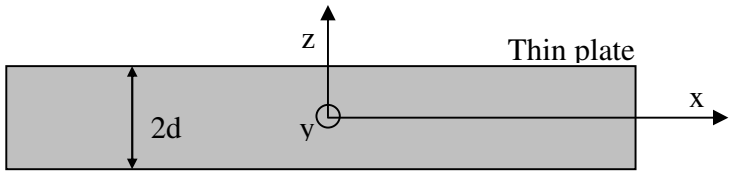

Figure 5.2: Geometry of the plate for Lamb wave propagation

The equation of motion of the particle displacements can be given as (Achenbach [58])

$$\mu w_{i,jj} + (\lambda + \mu) w_{j,ji} + \rho f_i = \rho \ddot{w}_i \tag{5.3}$$

where w_i are the displacements, f_i are body forces, λ, μ are Lame constants and ρ is the density. The boundary conditions for the surface tractions can be defined as $t_i = S_{ij} n_j$ where t_i are traction forces, S_{ij} are stresses and n_j are cosine directions. Using the Helmholtz decomposition, the wave equations can be obtained from Equation (5.3)

$$\frac{\partial^2 \phi}{\partial x_1^2} + \frac{\partial^2 \phi}{\partial x_3^2} = \frac{1}{c_L^2}\frac{\partial^2 \phi}{\partial t^2}$$
$$\frac{\partial^2 \psi}{\partial x_1^2} + \frac{\partial^2 \psi}{\partial x_3^2} = \frac{1}{c_T^2}\frac{\partial^2 \psi}{\partial t^2} \tag{5.4}$$

These wave equations govern the longitudinal and shear waves of plain strain. ϕ and ψ represent decomposed displacement variables, c_L indicates the velocity of longitudinal wave whereas c_T is the velocity of shear (transverse) waves. The actual longitudinal and transverse displacements of the plate can be obtained as

$$w_1 = \frac{\partial \phi}{\partial x_1} + \frac{\partial \psi}{\partial x_3} \qquad \text{longitudinal}$$
$$w_2 = \frac{\partial \phi}{\partial x_3} - \frac{\partial \psi}{\partial x_1} \qquad \text{transverse} \tag{5.5}$$

respectively. The solutions of Equations (5.4), representing traveling waves in the x_1 direction and standing waves in the x_3 direction can be assumed to be in the form given by

$$\phi = \Phi(x_3)\exp[i(kx_1 - \omega t)]$$
$$\psi = \Psi(x_3)\exp[i(kx_1 - \omega t)] \tag{5.6}$$

where ω is the frequency and k is the wavenumber. Substituting Equations (5.6) into Equations (5.4) gives the unknown amplitude functions Φ and Ψ as

$$\Phi(x_3) = C_1 \sin(px_3) + C_2 \cos(px_3)$$
$$\Psi(x_3) = D_1 \sin(qx_3) + D_2 \cos(qx_3) \tag{5.7}$$

where

$$p^2 = \frac{\omega^2}{c_L^2} - k^2 \text{ and } q^2 = \frac{\omega^2}{c_T^2} - k^2 \tag{5.8}$$

and C_1, C_2, D_1, D_2 are arbitrary constants. Since both field variables involve sine and cosine functions, which are odd and even respectively, the solutions are often split into two symmetric and anti-symmetric modes. The displacements for the symmetric modes are

$$\begin{aligned} w_1 &= ikC_2 \cos(px_3) + qD_1 \cos(qx_3) \\ w_2 &= -pC_2 \sin(px_3) - ikD_1 \sin(qx_3) \end{aligned} \tag{5.9}$$

whereas the solutions for the anti-symmetric modes can be given as

$$\begin{aligned} w_1 &= ikC_1 \sin(px_3) - qD_2 \sin(qx_3) \\ w_2 &= pC_1 \cos(px_3) - ikD_2 \cos(qx_3) \end{aligned} \tag{5.10}$$

These equations, referred as Rayleigh-Lamb equations for guided waves in plates, show that Lamb wave propagation is generally complex due to the coexistence of at least two modes at any given frequency and the strongly dispersive nature of these modes at high frequency. The traction-free boundary conditions for the plain strain need to be additionally applied in order to obtain the constants C_1, C_2, D_1, and D_2. This lead to Rayleigh-Lamb frequency relations known as dispersion equations

$$\frac{\tan(qh)}{\tan(ph)} = -\frac{4k^2 pq}{(q^2 - k^2)^2} \text{ for the symmetric modes} \tag{5.11}$$

$$\frac{\tan(qh)}{\tan(ph)} = -\frac{(q^2 - k^2)^2}{4k^2 pq} \text{ for the anti-symmetric modes} \tag{5.12}$$

where $h = d/2$. The above equations can be solved numerically in order to predict velocities of a propagating Lamb wave of frequency f in a plate of thickness d. The results are presented as a function of the fd frequency-thickness product. Figure 5.3 gives an example of the dispersion characteristics for an aluminum plate.

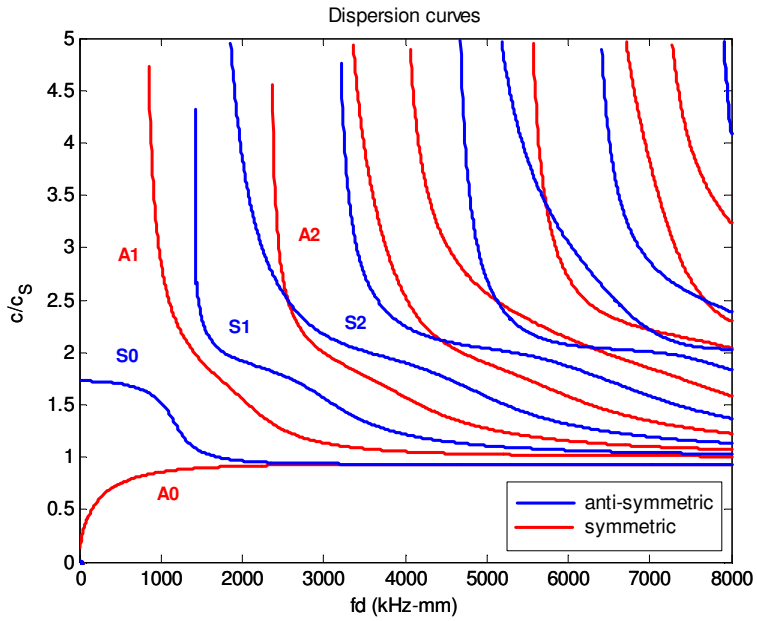

Figure 5.3: Lamb wave dispersion characteristics for an aluminum plate

This figure clearly shows how many complex modes can propagate in the plate. Single S_0 and A_0 Lamb wave modes are possible only for small values of the frequency-thickness product (typically $fd < 2$).

5.3.3 Modes selection for damage detection

As seen in the Figure 5.3, a different number of modes may propagate depending on the frequency-thickness values. In a practical application of Lamb waves, for simplicity of analysis, the frequency-thickness values are kept under the cut-off frequency of the A_1 mode where there is only a fundamental symmetric mode S_0 and a fundamental anti-symmetric mode A_0. The anti-symmetric mode is widely used in detection of damage in composite structures due to its sensitivity to delamination damages [59]. The fundamental symmetric mode has been used to detect surface

crack growth in metallic structures [60] and is utilized in this study for hole detection in an aluminum plate

5.4 Excitation and sensing of Lamb waves

There are a variety of techniques for generating and receiving Lamb waves. Advanced methods employ laser sources for generation and optical fiber detectors for reception. The simplest methods use piezoelectric devices since they exhibit simultaneous actuator and sensor behavior. Piezoelectric transducers are the most widely used sensors for damage detection. Their low weight and volume makes them suitable for incorporation in autonomous systems. The two most widely used manufactured materials are lead zirconate titanate (PZT) and polyvinylidene fluoride (PVDF). The PZT is a ceramic and is quite brittle whereas the PVDF are very flexible polymer films, easy to handle.

5.4.1 Constitutive equations

Piezoelectric materials exhibit coupled mechanical, electrical and piezoelectric properties. The constitutive equations describing these materials can be given as

$$\begin{aligned} S &= S_E T + d^t E \\ D &= \varepsilon_T E + dT \end{aligned} \tag{5.13}$$

where S is the mechanical strain, E is the electric field, T is the mechanical stress, D is the electrical displacement, d is the piezoelectric coefficient and ε is the permittivity. The subscripts E and T indicate that the quantities are under constant electrical and stress fields, respectively. Piezoelectric coefficients d_{ij} characterize

either the strain produced by an applied electrical field or the charge density developed from the applied stress field and are defined as

$$d_{ij} = \frac{strain}{applied\ electric\ field} = \frac{charge}{applied\ stress} \tag{5.14}$$

The subscript *i* indicates the direction of electric field or displacement, whereas the subscript *j* gives the direction of strain or stress. Typical properties of ceramic and polymer based piezoelectric materials are given in the Table 5.1.

	Ceramic (PZT-5H [63])	Polymer (PVDF [64])
ρ (kg/m^3)	7500	1780
S_{11}^E (10^{-12}m^2/N)	16.5	250
d_{31} (10^{-12}V/m)	-274	23
d_{33} (10^{-12}V/m)	593	-33
$\varepsilon_{33}/\varepsilon_0$ ($\varepsilon_0 = 8.85\times10^{-12}$F/m)	3400	12

Table 5.1: Typical properties of piezoelectric materials

5.4.2 PZT actuator

From the Equation (5.13), an applied electric field will produce a mechanical deformation. This is the converse effect, illustrated graphically in the Figure 5.4.

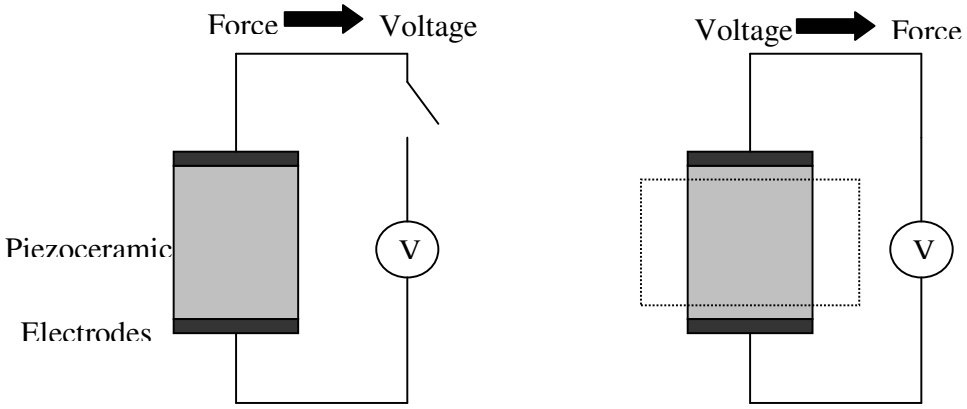

Figure 5.4 Direct and Inverse piezoelectric effects

When an electric field is applied in the direction normal to the PZT surface, surface strains are generated. Due to the coupling of the element to the structure, forces and moments are induced in the structure, generating elastic waves. A single piezoelectric element on a plate would produce both an in-plane loading and a bending moment. The actuation transducer used was a PZT-5H piezoceramic element and is shown in the Figure 5.5.

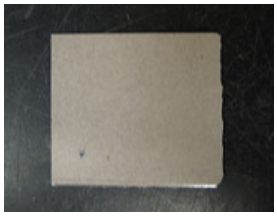

Figure 5.5: PZT-5H piezoceramic element

A single 3.2 mm x 3.2 mm (1/8 inch x 1/8 inch) element was directly mounted on the right edge of the top surface of the plate and used to interrogate it.

5.4.3 PVDF sensor array

From Equation (5.13), the resulting deformation in a material due to a mechanical force generates an electric field proportional to the magnitude of the deformation. This is the direct effect as seen in the Figure 5.4. When an elastic wave propagates through the structure, the strain and stresses induced generate a voltage on the piezoceramic element. One way to use the direct effect is to hold the electric field, E, constant. As a result, the electric displacement on the surface of an element is only a function of mechanical quantities. The electric displacement is obtained from

integrating over the area of the sensing element to get a charge representing a measure of the strain in the material:

$$q = \int_A D_3 dA \tag{5.15}$$

The use of an array of sensors offers a better robustness, reliability and confidence in the results. It will be shown later that it also allows a spatial filtering of the propagating and reflecting waves. A sensor array made from a 52 μm (.002 in.) thick PVDF piezoelectric sheet from Measurement Specialties, Inc. is used in the experimental damage setup. For this experiment, a sensor array, like the one shown in Figure 5.6, is composed of 19 elements with a spacing of 3.175 mm (1/8 in.) where each sensor has a diameter of 1.59 mm (1/16 in.).

Figure 5.6: PVDF sensor array

5.5 Experimental setup and results

5.5.1 Equipment

The set of experiments conducted in this thesis made use of tools and equipments commonly used in a laboratory. A signal conditioning circuitry has been created by Purekar [39] to obtain the PVDF sensor signals. A charge amplifier circuit with additional gain stages was created for this purpose. The Tektronix TDS420A digital

oscilloscope (see Figure 5.7) was used to display the sensor signals and to store the data on a disk. The piezoceramic actuator was excited by a signal constructed and transferred to the Agilent 33220A function generator, shown in the Figure 5.7. This function generator could read the digital signal and output the corresponding analog signal to the power amplifier. The Piezo Systems, Inc. EPA-104 power amplifier was aimed to provide the necessary power for the excitation of the actuation element.

(a) Tektronix TDS420A oscilloscope

(b) Agilent 33220A function generator

(c) Piezo Systems, Inc. EPA-104 power amplifier

Figure 5.7: Experimental equipment

Figure 5.8 summarizes the damage detection configuration used in this thesis.

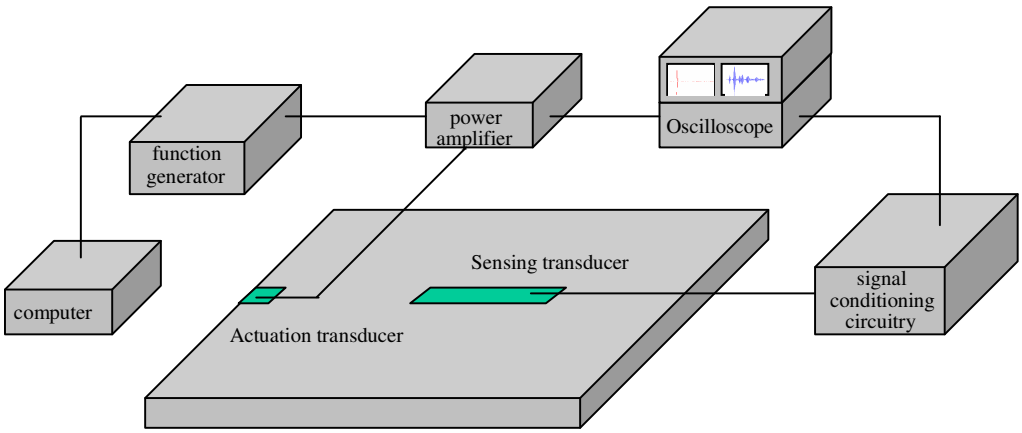

Figure 5.8: Damage detection configuration

5.5.2 Damage detection setup

A .060 inch thick aluminum plate was instrumented with a sensor array and the actuator described earlier. The plate was 26 inches long and 20 inches wide. A 1/8 inch diameter hole was first drilled at a distance of 6 inch from the middle sensor. The size of the holes was progressively increased to reach a maximum size of ½ inch. The plate is shown in Figure 5.9.

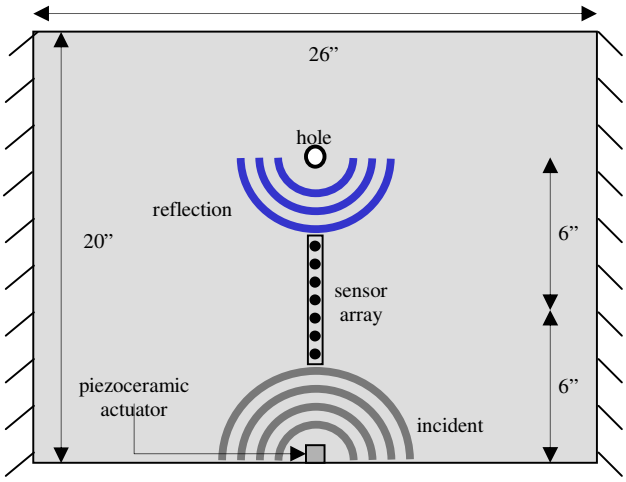

Figure 5.9: Experimental setup

A piezoceramic actuator was used to excite the structure with Lamb waves. The waves propagated outward, through the array, and reflected off of the hole. The sensor array was used to capture the transient signals associated with the incident and reflected wave energy.

5.5.3 Transient analysis

The excited transient signal made up of a windowed 5 cycles sine tone burst at 600 kHz is shown in the Figure 5.10 along with its frequency spectrum. This signal is windowed in order to get a single wave traveling at the desired driving frequency.

Because the pulse has a finite duration, range of frequencies is excited rather than a single frequency and dispersion distorts the shape of the pulse as different frequency components travel at different velocities. A Dolph-Chebyshev window was used to prevent the generation of unwanted modes. The advantage of this windowed tine burst was the elimination of significant side lobes allowing for the attenuation of the spurious parasite modes.

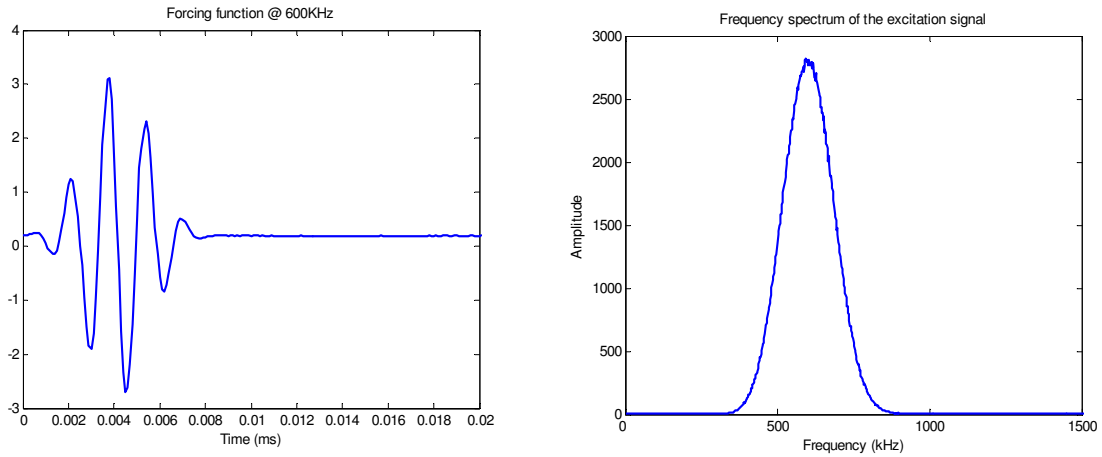

(a) Time domain signal (b) Frequency spectrum

Figure 5.10 : Excitation signal sent to actuation element

The waves created by the actuation element propagate outward and the signals at each sensor location are gathered. Each sensor signal is averaged 40 times before being saved on the disk. A sample of the saved transient signals is shown in Figure 5.11. The signals correspond to the S0 mode propagating in the plate gathered by sensors #01 and #19 of the array. The S0 mode was chosen because higher frequency waves are generally more appropriate for detecting small amounts of damage. As expected, the waves travel to the top and hit the lowest element first. The first wave corresponds to the S0 mode whereas the second wave corresponds to the wave reflecting off of the right and left edges of the plate.

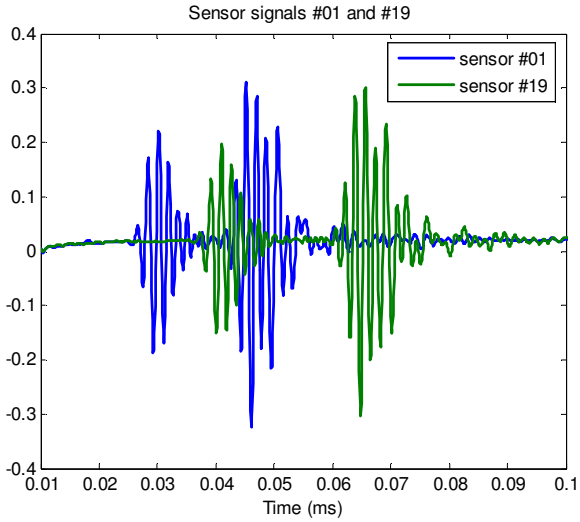

Figure 5.11: Sample of the response signals

5.6 Hilbert-Huang Transform analysis

5.6.1 Empirical mode decomposition

Once the response signals are gathered for all sensors, the processing of the data starts by the empirical mode decomposition and the sifting process to extract the intrinsic mode functions. The comparison between the undamaged and damaged transient signals of the middle sensor does not give any information about the presence or not of damage in the plate, as shown in the Figure 5.12.

Both signals seem identical and the reflection from the hole is not visible. Thus, we cannot determine the status of the plate's health from the transient signals. The empirical mode decomposition algorithm is applied on these signals and the resulting IMFs are plotted in the Figure 5.13 and 5.15.

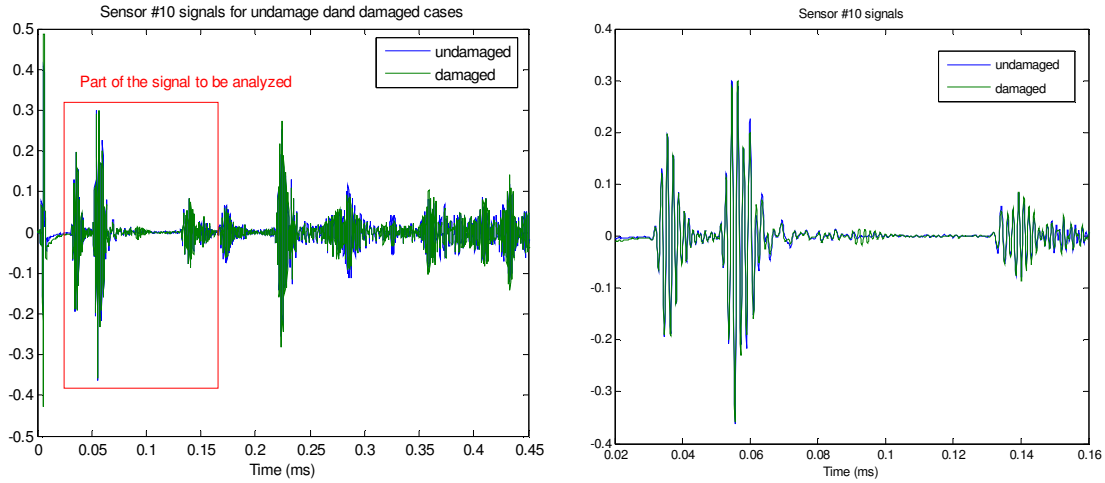

(a) Damaged and undamaged signals comparison

(b) Portion of signal to be analyzed

Figure 5.12: Middle sensor responses

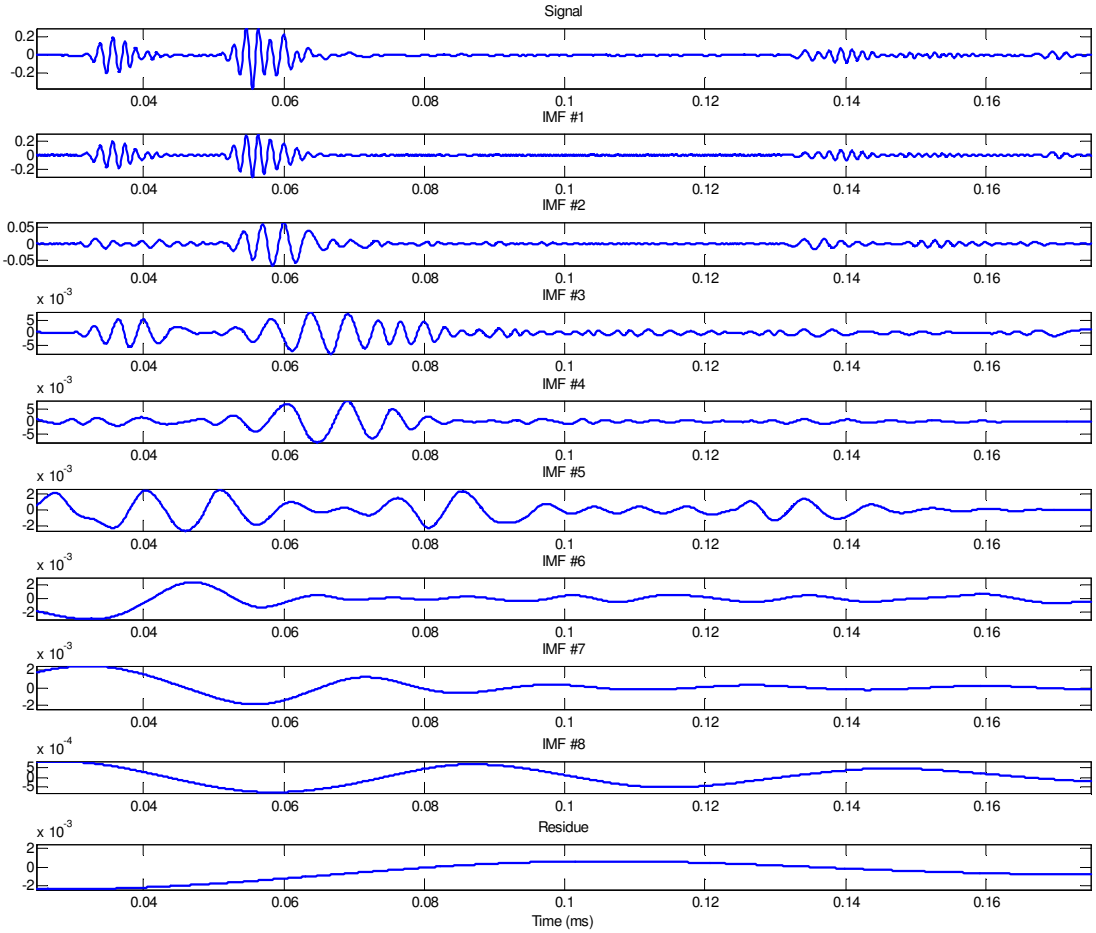

Figure 5.13: Empirical mode decomposition of the undamaged signal

The EMD extracted 9 IMFs for both undamaged and damaged cases. Because of the implementation problems of the algorithm detailed in Chapter 3, some IMFs may not have a physical meaning. In our study, only one part of the signal gathered by the sensor needs to be examined since all the damage information is contained between the right/left edges and the upper edge reflections. As a result, the meaningful component of the sensor signal must be extracted. Indeed, the initial wavefront is an interference noise due to the conditioning circuitry whereas the rest of the signal is composed of multiple unwanted reflections. The signal included in the red box of the Figure 5.12 is therefore extracted and windowed with a Tukey window in order to get smooth ends for the spline-fitting step of the sifting process. An energy threshold value is proposed to retain the physical meaningful IMFs. If the energy carried by the IMF is less than a certain value, the corresponding IMF is not taken into account in the analysis. The energy of each IMF is therefore computed and plotted in the Figure 5.14.

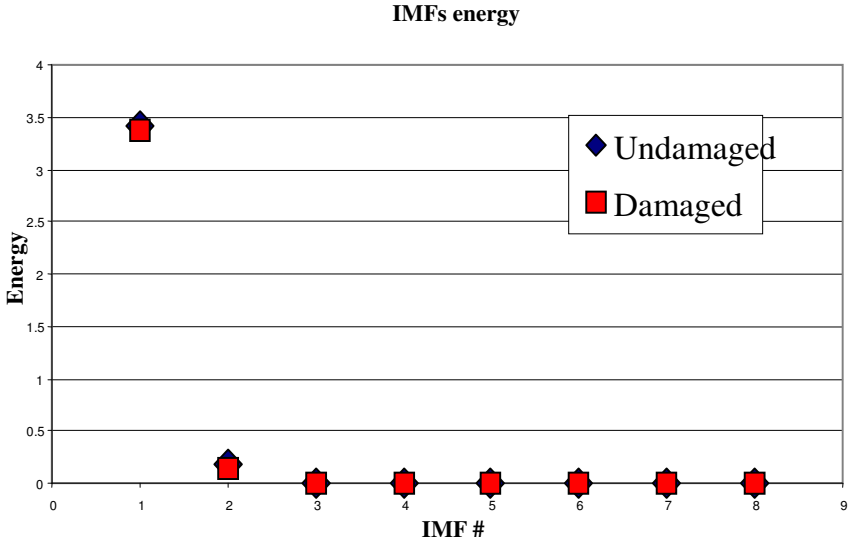

Figure 5.14: Variation of IMFs energy

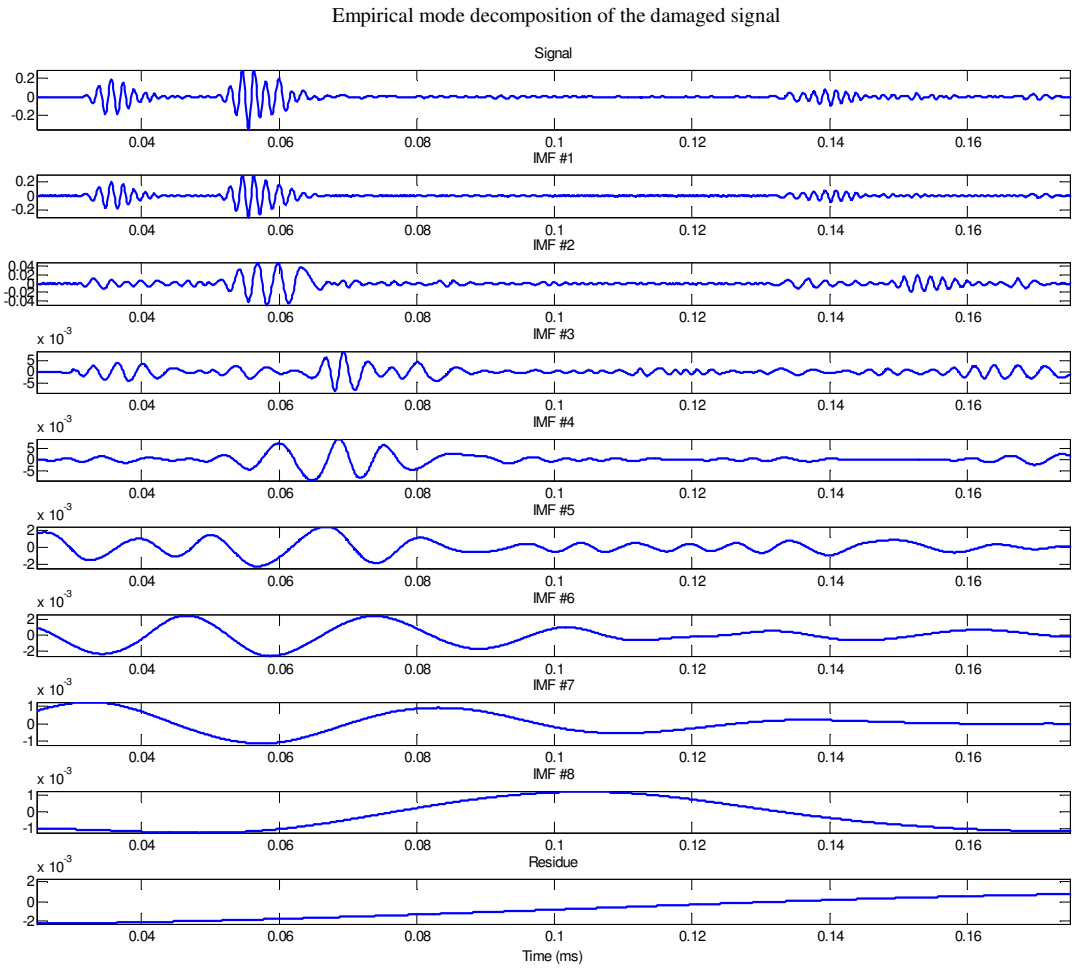

Figure 5.15: Empirical mode decomposition of the damaged signal

For this precise case study, most of the wave propagation information is carried in the first 2 IMFs. A closer look at the first intrinsic mode leads to an interesting observation. A new wave appears only in the damaged IMF, corresponding to a discontinuity reflection in the plate. The presence of the hole is therefore detected in the first IMF, as seen in the Figure 5.16.

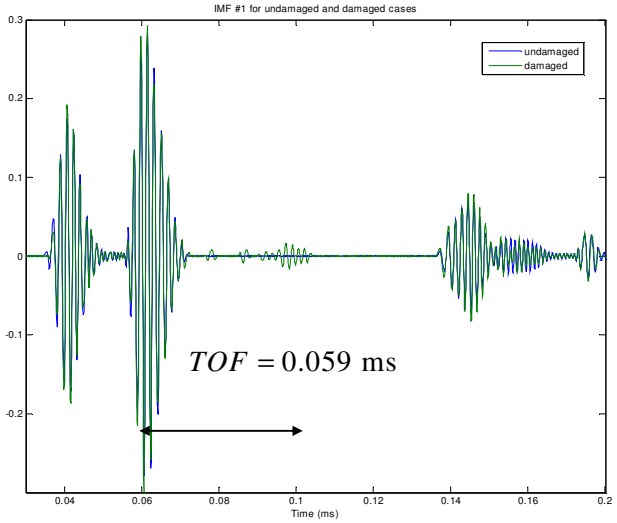

Figure 5.16: IMF #01

The wave propagation characteristics along with the time of flight between the actuation and the damage reflection leads to an estimation of the damage distance. This position is determined using the group speed of the mode at the given frequency. The Lamb wave group velocity curves can be determined from the aluminum properties and the plate thickness (see Figure 5.17).

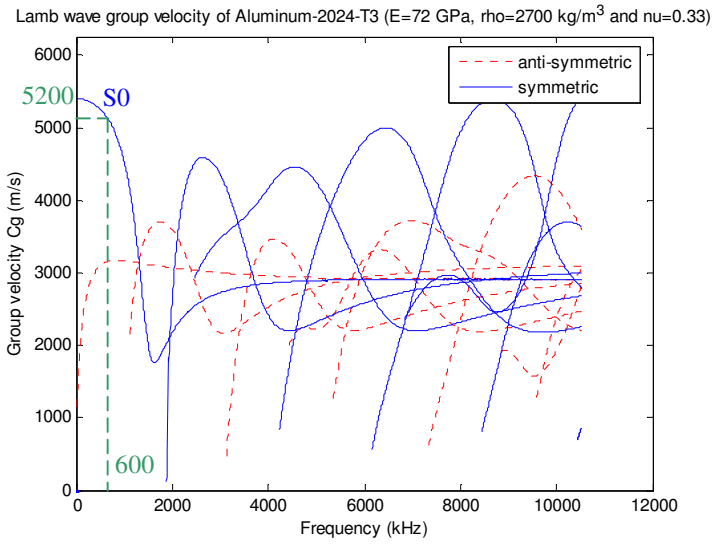

Figure 5.17: Lamb wave group velocity characteristics for an aluminum plate

At a 600 kHz frequency, the S0 Lamb wave propagates at a speed $c_g = 5200$ m/s in a .060 inch thick aluminum plate. The time of flight between the actuation waveform and the reflection wave from the hole is determined through the IMF #1 plot in Figure 5.16. The location of the damage can then be inferred, as shown in the Figure 5.18.

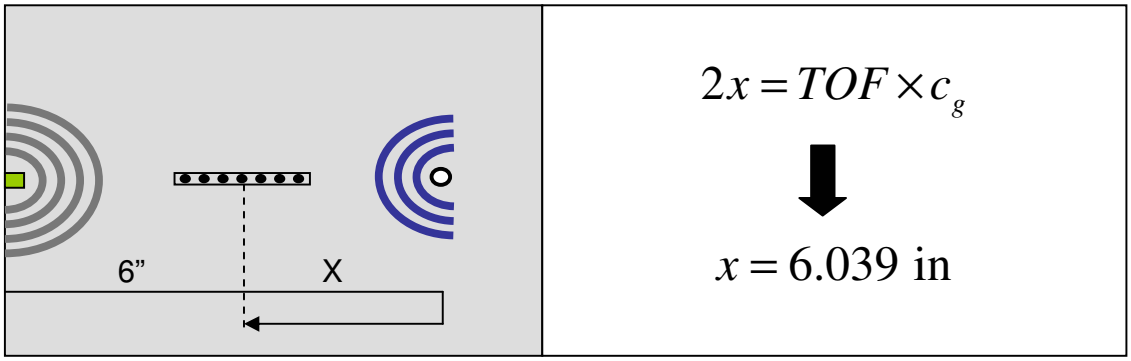

Figure 5.18: Localization of the hole position

The exact distance of the hole was 6 in. from the middle sensor. The estimation from the time of flight and the group speed localized the hole at 6.039 in., which corresponds to less than 1% error. Thus, the empirical mode decomposition gives a really precise approximation of the location of the damage. The sifting process has cleared the original signal of all the noise and interferences to give a new and comprehensible signal where the reflections of the boundaries and the damage were obviously revealed. One of the main advantages of the empirical mode decomposition is its ability to extract embedded oscillations in the signal. In the present study, the EMD allows the extraction of the embedded reflection from the damage that was hidden in the transient signal displayed in Figure 5.12. The size of the hole is now increased in order to investigate the ability of the Hilbert-Huang transform to track

the increasing damage. The energy metric and the phase shift metric are tested to detect the damage growth in the plate.

5.6.2 Hilbert-Huang spectrum and the Energy metric

As outlined in the Chapter 4, the energy metric uses the high-resolution energy-time-frequency representation provided by the Hilbert spectral analysis. Since, the energy metric relies on the Hilbert-Huang spectrum, a study of the three-dimensional images of both damaged and undamaged cases is carried out. The EMD associated with the Hilbert spectral analysis is therefore applied to the response signal of sensor #1. Only the first IMF is considered in this study since most energy is concentrated within the first mode. The damaged (hole size = 1/2 in.) and undamaged Hilbert-Huang spectrum are plotted in the Figure 5.19.

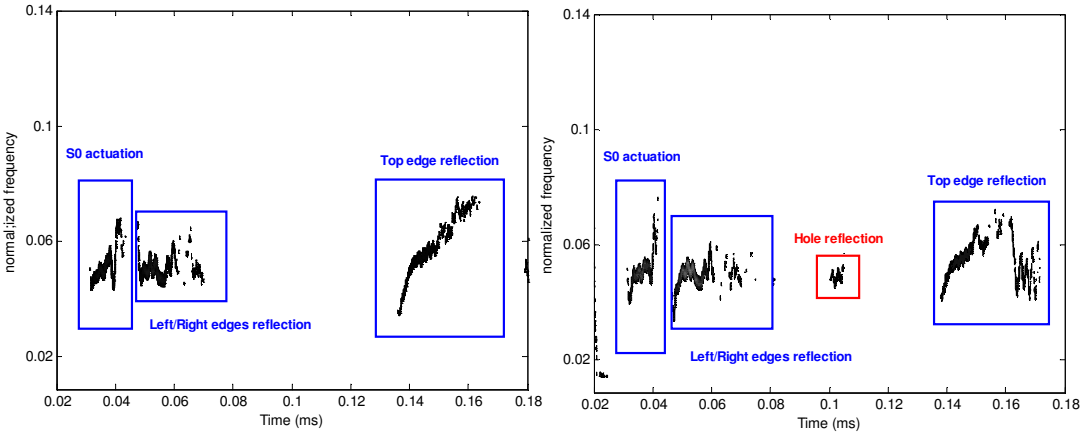

(a) Undamaged spectrum (b) Damaged spectrum

Figure 5.19: Hilbert-Huang spectrum for the sensor #01

The smoothed spectra have been privileged as a first qualitative approach. The different frequency bands correspond to the S0 actuation wave, the reflection from the right and left edges and the reflection from the top edge, respectively. The

damaged spectrum also revealed the reflection from the hole. The propagation is entirely described through the time-frequency spectrum. The array can be used to infer the direction of propagation of the different waves present in the signal. The spectra for the response signals of sensor #19 are plotted in Figure 5.20 to confirm the wave propagation properties as well as the presence of the defect.

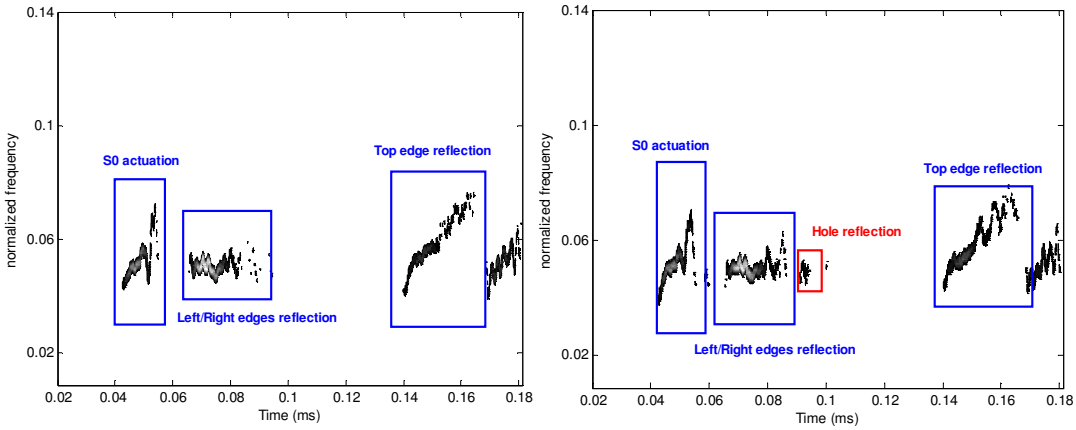

(a) Undamaged spectrum (b) Damaged spectrum

Figure 5.20: Hilbert-Huang spectrum for the sensor #19

The study of these plots indicates the way the waves travel in the plate. As we can see, the different frequency bands propagate along the time axis from sensor #1 to sensor #19. The wavefronts corresponding to the S0 actuation and the right and left edges reflections propagate rightward since they arrive later in time to the sensor #19 than to the sensor #1. On the contrary, the reflection from the hole travels leftward and is sensed earlier by the sensor #19. This observation confirms that the frequency band identified in the damaged signal correspond to the reflection from the damage.

A quantitative approach of the Hilbert-Huang spectrum is now examined in order to detect defect growth. The damage index, based on the energy density, consists of

extracting the reflection from the damage and computing the energy release in the structure, displayed in the Hilbert-Huang energy spectrum. The energy metric has been defined in Chapter 4 as

$$E = \sum_f \sum_t \left| H_e(t, f) \right| = \sum_f \sum_t \left| a(t)^2 \right| \tag{5.16}$$

where $H_e(t, f)$ is the energy density spectrum and $a(t)$ is the instantaneous amplitude.

Four holes sizes are considered in this experiment, ranging from 1/8 in. to 1/2 in. The energy density spectrum of the reflection wave is plotted for each case in the Figure 5.21 along with the corresponding energy computation. As expected, the energy metric increases as the damage increases. A linear interpolation of the energy release in the structure upon defect growth is created from the first 3 cases as a tool to predict the size of damage. This curve is then used for the last case corresponding to a 1/2 in. hole drilled in the plate in order to predict the size of this hole from the energy measurement. The linear fit is plotted in the Figure 5.22.

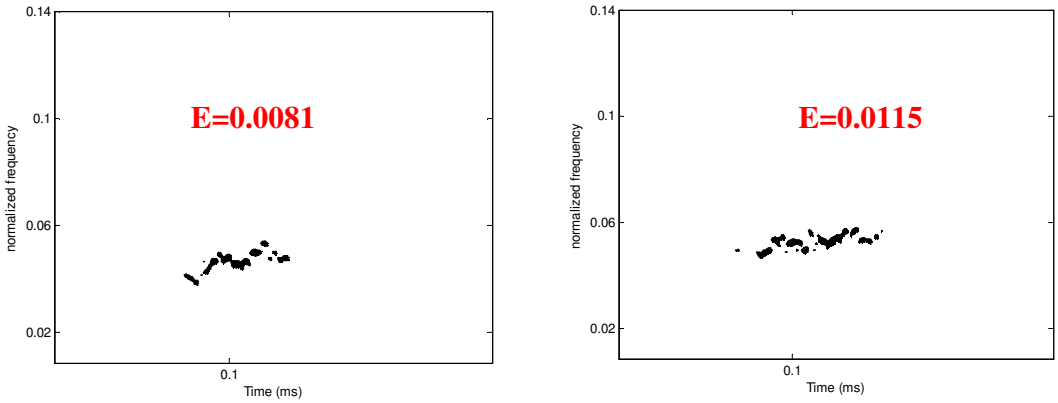

(a) Hole #01 (b) Hole #02

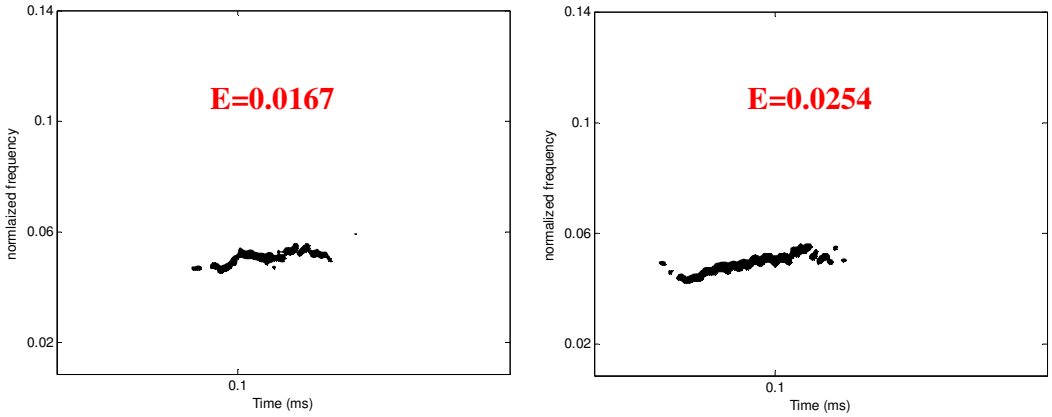

(c) Hole #03 (d) Hole #04

Figure 5.21: Energy density of the damage reflected frequency band

The reflected energy for the 1/2 in. hole is given in the Figure 5.21. This value can be plugged in the prediction trend in order to obtain an estimation of the size of the corresponding hole. The energy value of $E = 0.0254$ leads to an approximate diameter of $\phi = 0.56$ in., which corresponds to a 12 % error.

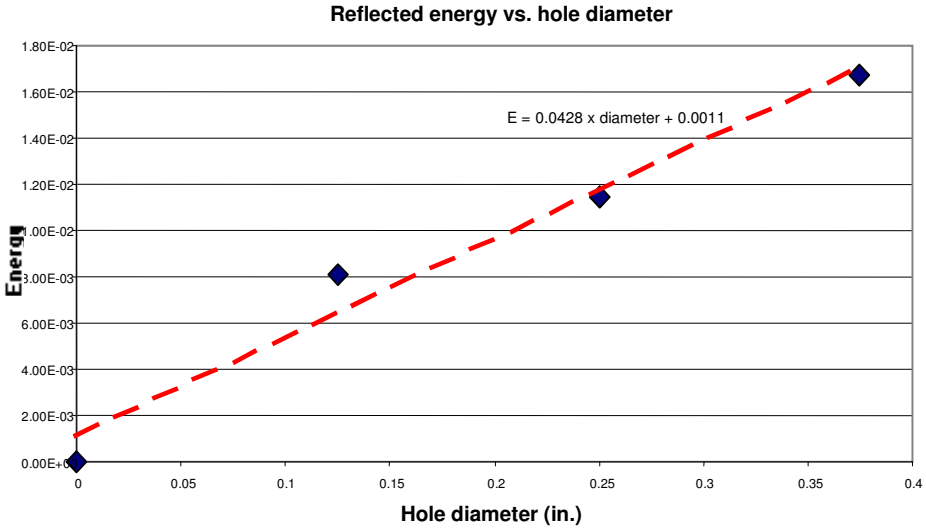

Figure 5.22: Linear prediction of the hole diameter from the reflected energy

The energy metric turned out to be able to detect the location of damage as well as to give an estimation of its size. However, a prediction trend corresponding to each type of damage must be defined beforehand to predict the size of a defect from the energy released in the structure.

5.6.3 Energy-time spectrum and the Phase shift metric

The importance of an accurate signal processing technique for obtaining the flight times cannot be over-stressed. In our study, accurate identification of localized events is required to determine the location of the damage in the plate precisely and to quantify the defect growth. The phase shift metric uses the time resolution of the Hilbert-Huang transform to extract accurate time of flight so as to track the increasing damage in a structure. The peaks on the energy-time spectrum for the IMF component containing the highest energy give the wave arrival times of interest. As seen earlier, the first IMF encloses the highest energy in the signal. The energy-time spectrum for the first IMF of the plate is plotted for each damage size for an actuation frequency of 700 kHz, in the Figure 5.23.

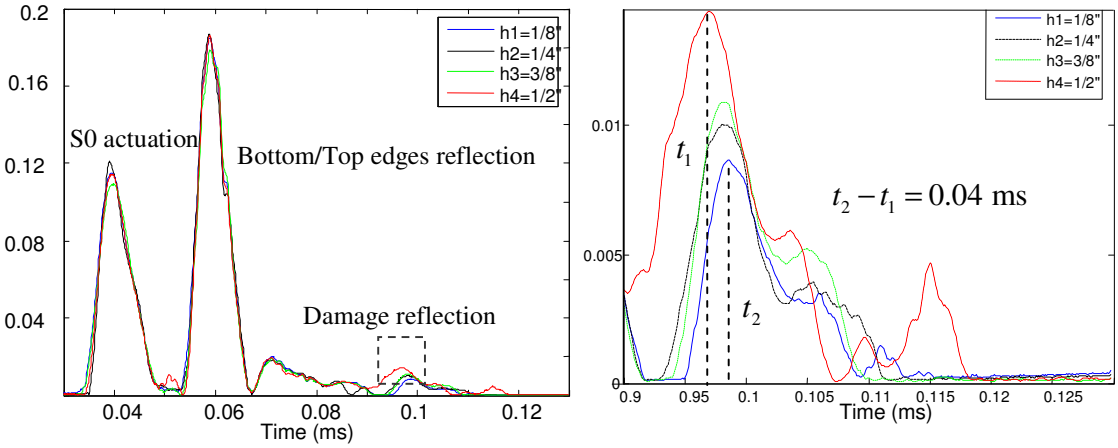

(a) Energy-time spectrum of damaged signals (b) Portion of spectrum corresponding to reflection

Figure 5.23: Energy spectrum and phase shift metric

A small time difference exists between the different reflections from the holes. The amplitude peaks corresponding to the damages reflections are shifted in time, indicating a change in the size of the damage. Some simple geometric considerations along with the Lamb wave group velocity can quantify the extent of the damage, as depicted in the Figure 5.24. The shape and the initial size of the damage are assumed to be known.

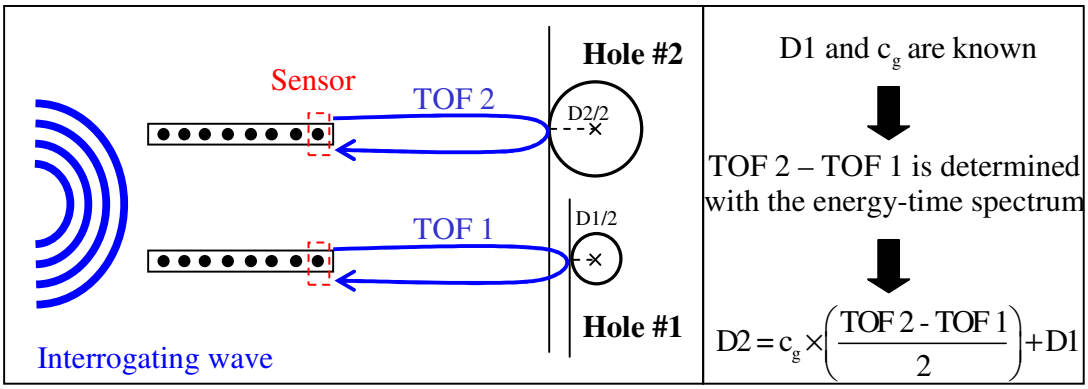

Figure 5.24: Quantification of the damage size from the time of flight

The size of the 1/2 in. hole is predicted assuming the initial size hole is 1/8 in. and that the hole is circular. From the time difference between the two maximum peaks, the extent of the damage can be inferred and the new diameter is estimated: $\phi = 0.53$ in., which gives a 7% error. The time difference between the actuation sensing and the reflected wave from the different holes sizes is plotted in the Figure 5.25. A polynomial trend fits the data and can be used as a damage prediction curve as well.

The bigger the damage is, the less time is needed by the wave to travel between the actuator and the sensor. The energy peaks in the Hilbert spectrum corresponding to

crack-reflected waves provide a means for determining accurate flight times and also for estimating the severity of the damage.

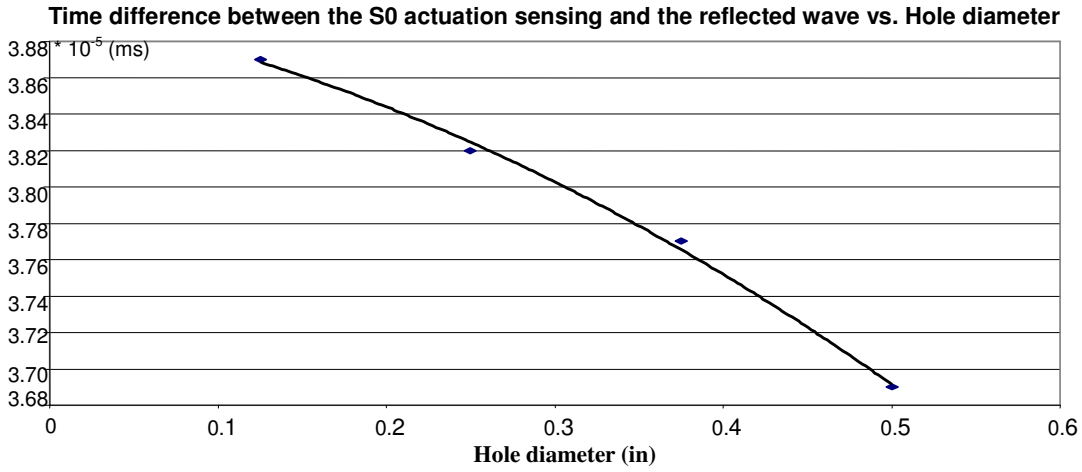

Figure 5.25: Time difference trend relating the actuation and the reflected waves

5.7 Summary

The Empirical Mode Decomposition (EMD) technique using the Hilbert-Huang transform was demonstrated to be useful for hole detection and characterization using phased arrays in Aluminum plates. Experimental data on an Aluminum plate was analyzed for hole detection and characterization. In the damaged case, the reflected wave from a hole is observed on the first intrinsic mode function (IMF) of the decomposition whereas no reflection can be seen for the undamaged case. The sifting process has proved to be efficient in separating the transient signal from noise and interferences to reveal hidden reflections in the data. From the time of flight and using the known wave propagation speed, the damage position could be found. To estimate the size of the hole, two metrics were examined: one was the reflected

energy in the Hilbert Huang spectrum. As the damage size increases, the reflected energy increases and fits a linear curve. The prediction of a damage size was also possible, using the interpolation trend and the energy measurement. The other metric was the phase shift between the reflected signals from the holes. As the damage size increases, the time difference between the traveling waveforms and the reflecting waveform decreases. The smallest time of flight will correspond to the hole with the biggest diameter. The extent of the damage could also be quantified if the initial shape and size were known.

Chapter 6

Damage detection in composite plates

6.1 Introduction

The high stiffness to weight ratio, low electromagnetic reflectance and the ability to embed sensors and actuators have made fiber-reinforced composites very attractive for primary aircraft structures. However, damage detection in composites is more difficult than in metallic structures due to the anisotropy of the material, the conductivity of the fibers, the insulating properties of the matrix, and the fact that much of the damage often occurs beneath the top surface of the laminate and is therefore not readily detectable. The Acousto-ultrasonic technique becomes therefore more complicated for composite structures due to the anisotropic nature of the material. The wave propagations dynamics is now dependent of the layup of the laminate. The dispersion curves are not anymore described by the Equations (5.11) and (5.12). Purekar [39] used a finite element approach to model the wave propagation dynamics and to obtain the dispersion relations. The CLPT theory also provides the wavenumber-frequency relationships for both transverse and in-plane vibrations. These results will be used to apply an acousto-ultrasonic approach for damage detection in composite plate structures experimentally. The most common encountered defects in composite structures are delaminations and impact damage. Delamination can produce catastrophic failure due to loss of interlaminar shear carrying capability whereas impact damage causes significant loss on the

compression static strength. A set of experiments, involving cross plies laminates, is conducted in this research in order to simulate these types of damage. A low-velocity impact experiment is realized with a pendulum mechanism to reproduce a real world situation. The acousto-ultrasonics approach along with the HHT data processing tool for damage detection looks for changes in the wave propagation characteristics due to defects in the structure. In this study, the low frequency A0 mode is used in the composite laminate to determine the presence of delaminations and impact damage. The data are post-processed with the HHT in a damage detection and quantification purpose. On the contrary of the isotropic study where a single sensor was used, the array is exploited to spatially filter sensor signals to extract reflections from damage. The Hilbert-Huang transform analysis shows promising results for damage detection in composite plate structures.

6.2 Wave propagation in composite laminates

6.2.1 Low-frequency wave propagation

At low frequency, the common way to model the wave propagation is to use the Classical Laminated Plate Theory (CLPT). By use of this theory, the stiffness properties of a structural laminate can be determined from the basic building block, the lamina.

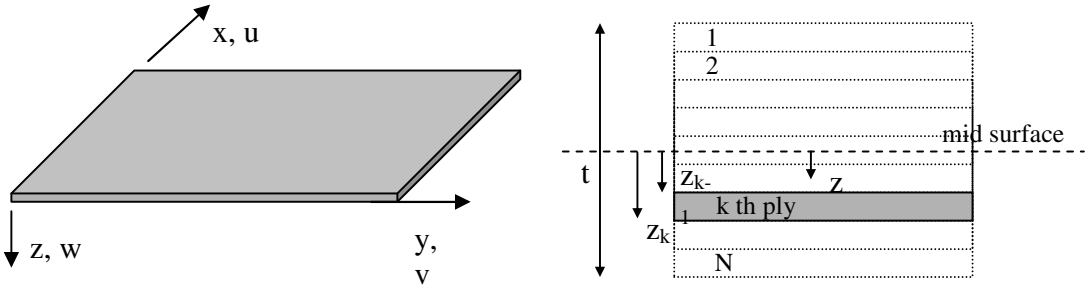

Figure 6.1: Laminate configuration

First, the stress-strain behavior of an individual lamina is expressed for the k^{th} ply of a laminate [61] by

$$\{\sigma\}_k = [Q]_k \{\varepsilon\}_k \tag{6.1}$$

where Q are the transformed reduced stiffnesses, defined in terms of the engineering constants. Then, the variations of stress and strain through the thickness of the laminate are determined in order to define the extensional and bending stiffnesses of the laminate. Assuming linear displacement distributions through the thickness of the laminate, the strains are

$$\begin{bmatrix} \varepsilon_x \\ \varepsilon_y \\ \gamma_{xy} \end{bmatrix} = \begin{bmatrix} \varepsilon_x^0 \\ \varepsilon_y^0 \\ \gamma_{xy}^0 \end{bmatrix} + z \begin{bmatrix} \kappa_x \\ \kappa_y \\ \kappa_{xy} \end{bmatrix} = \begin{bmatrix} u_{0,x} \\ v_{0,y} \\ u_{0,y} + v_{0,x} \end{bmatrix} - z \begin{bmatrix} w_{0,xx} \\ w_{0,yy} \\ 2w_{0,xy} \end{bmatrix} \tag{6.2}$$

u_0 and v_0 are constant in-plane displacements and the derivative of the in plane displacements are expressed by $u_{0,x}$ and $v_{0,y}$. The second derivative of the transverse displacement $w_{,xx}$ and $w_{,yy}$ express the middle curvature of the middle surface.

The resultant forces and moments acting on a laminate are obtained by integration of the stresses in each layer through the laminate thickness

$$\begin{bmatrix} N_x \\ N_y \\ N_{xy} \end{bmatrix} = \int_{-t/2}^{t/2} \begin{bmatrix} \sigma_x \\ \sigma_y \\ \tau_{xy} \end{bmatrix} dz \qquad \begin{bmatrix} M_x \\ M_y \\ M_{xy} \end{bmatrix} = \int_{-t/2}^{t/2} \begin{bmatrix} \sigma_x \\ \sigma_y \\ \tau_{xy} \end{bmatrix} z dz \tag{6.3}$$

Substituting Equations (6.1) and (6.2) in (6.3), the force-strain curvature and moment-strain curvature relations can be expressed in a matrix form

$$\begin{bmatrix} N \\ M \end{bmatrix} = \begin{bmatrix} A & B \\ B & D \end{bmatrix} \begin{bmatrix} \varepsilon_0 \\ \kappa \end{bmatrix} \tag{6.4}$$

where $A = \sum_{k=1}^{N} [Q]_k \left(z_k - z_{k-1} \right)$, $B = \frac{1}{2} \sum_{k=1}^{N} [Q]_k \left(z_k^2 - z_{k-1}^2 \right)$ and $D = \frac{1}{3} \sum_{k=1}^{N} [Q]_k \left(z_k^3 - z_{k-1}^3 \right)$

The configuration and the geometry of the plate are shown in the Figure 6.1. The matrices A, B, D are therefore dependent on the stacking sequences of the plies. Thus, the choice of the layup will change the properties of a laminate, constructed with the same ply material.

For dynamic problems, the governing equations of motion are shown to be [39]:

in-plane:

$$\begin{bmatrix} \frac{\partial}{\partial x} & 0 & \frac{\partial}{\partial y} \\ 0 & \frac{\partial}{\partial y} & \frac{\partial}{\partial x} \end{bmatrix} \begin{bmatrix} N_x \\ N_y \\ N_{xy} \end{bmatrix} = m \begin{bmatrix} \ddot{u} \\ \ddot{v} \end{bmatrix} \Leftrightarrow \begin{bmatrix} \frac{\partial}{\partial x} & 0 & \frac{\partial}{\partial y} \\ 0 & \frac{\partial}{\partial y} & \frac{\partial}{\partial x} \end{bmatrix} \begin{bmatrix} A & B \end{bmatrix} \begin{bmatrix} \varepsilon_0 \\ \kappa \end{bmatrix} = m \begin{bmatrix} \ddot{u} \\ \ddot{v} \end{bmatrix} \tag{6.5}$$

transverse:

$$\begin{bmatrix} \frac{\partial^2}{\partial x^2} & \frac{\partial^2}{\partial y^2} & 2\frac{\partial^2}{\partial x \partial y} \end{bmatrix} \begin{bmatrix} M_x \\ M_y \\ M_{xy} \end{bmatrix} = m\ddot{w} \Leftrightarrow \begin{bmatrix} \frac{\partial^2}{\partial x^2} & \frac{\partial^2}{\partial y^2} & 2\frac{\partial^2}{\partial x \partial y} \end{bmatrix} \begin{bmatrix} B & D \end{bmatrix} \begin{bmatrix} \varepsilon_0 \\ \kappa \end{bmatrix} = m\ddot{w} \tag{6.6}$$

In our present research, the composite plate was constructed of IM7/8552 with a layup of [90/0/0/90]s. A laminate of multiple orthotropic layers that are symmetrically arranged about the middle surface exhibits no coupling between

bending and extension; that is the B matrix is zero. The extensional stiffness matrix, A, and the bending stiffness matrix, D, take also a simpler form:

$$A = \begin{bmatrix} A_{11} & A_{12} & 0 \\ A_{12} & A_{22} & 0 \\ 0 & 0 & A_{66} \end{bmatrix} \qquad D = \begin{bmatrix} D_{11} & D_{12} & 0 \\ D_{12} & D_{22} & 0 \\ 0 & 0 & D_{66} \end{bmatrix} \tag{6.7}$$

By introducing these simplified matrices in Equation (6.5) and (6.6), the governing equations of motion for transverse and in-plane wave propagation become:

$$\text{transverse: } D_{11}w_{,xxxx} + D_{22}w_{,yyyy} + 2\left(D_{12} + 2D_{66}\right)w_{,xxyy} + m\ddot{w} = 0 \tag{6.8}$$

$$\text{in-plane: } \begin{cases} A_{11}u_{,xx} + A_{12}v_{,xy} + A_{66}\left(u_{,yy} + v_{,xy}\right) - m\ddot{u} = 0 \\ A_{12}u_{,xy} + A_{22}v_{,yy} + A_{66}\left(u_{,xy} + v_{,xx}\right) - m\ddot{v} = 0 \end{cases} \tag{6.9}$$

A wave traveling solution in the x and y directions can be assumed and the wavenumber-frequency relationship can be deduced from the Equations (6.8) and (6.9):

$$\text{transverse : } \begin{cases} \text{x-dir.: } \left(w(x,y) = w_0 e^{i(\omega t - kx)}\right) \;\rightarrow\; k = \sqrt{\omega}\sqrt[4]{\dfrac{m}{D_{11}}} \\ \text{y-dir.: } \left(w(x,y) = w_0 e^{i(\omega t - ky)}\right) \;\rightarrow\; k = \sqrt{\omega}\sqrt[4]{\dfrac{m}{D_{22}}} \end{cases} \tag{6.10}$$

$$\text{in-plane: } \begin{cases} \text{x-dir.: } \left(u(x,y) = u_0 e^{i(\omega t - kx)} \text{ and } v(x,y) = 0\right) \;\rightarrow\; k = \omega\sqrt{\dfrac{m}{A_{11}}} \\ \text{y-dir.: } \left(u(x,y) = 0 \text{ and } v(x,y) = v_0 e^{i(\omega t - ky)}\right) \;\rightarrow\; k = \omega\sqrt{\dfrac{m}{A_{22}}} \end{cases} \tag{6.11}$$

The wavenumber-frequency relationships for both transverse and in-plane wave propagation have the same form than for the isotropic cases. However, these relations suggest that the wave propagation will depend on the stacking sequence and on the fiber direction. The wave group speed will therefore differ for each layup and for

each direction of travel. The CLPT theory is able to represent the low frequency dynamic of laminates. Nevertheless, this model is not valid at high frequencies since the assumption of no shear deformation is not verified anymore. A new model must be conceived to take in to account the shear deformation to predict the Lamb wave propagation at high frequencies.

6.2.2 High-frequency wave propagation

The finite element model constructed by Purekar [39] includes the shear deformation and hence can predict more accurately the Lamb wave propagation than the simple CLPT model. The wavenumber-frequency plots of the CLPT and FEM models are represented in the Figure 6.2 for the symmetric orthotropic laminate [90/0/0/90]s.

As seen in the previous Chapter, the knowledge of the Lamb wave group velocity in the material is indispensable to determine the location as well as the extent of damage. The group speeds, based on the CLPT and the FE model, are determined from the local slope of the wavenumber-frequency curves.

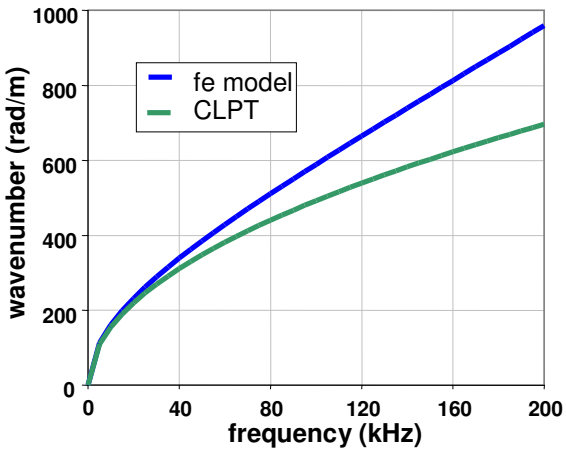

(a) A0 mode (0° direction)

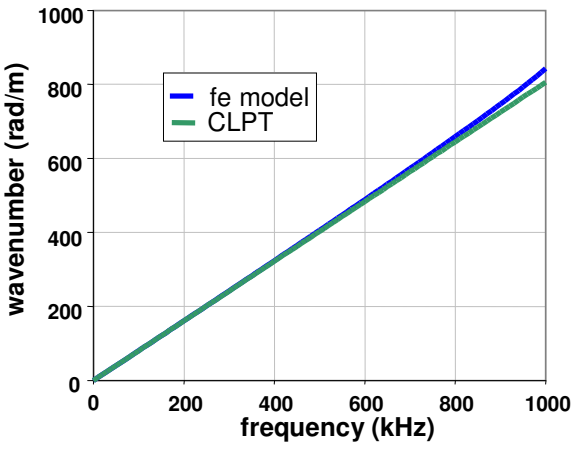

(b) S0 mode (0° direction)

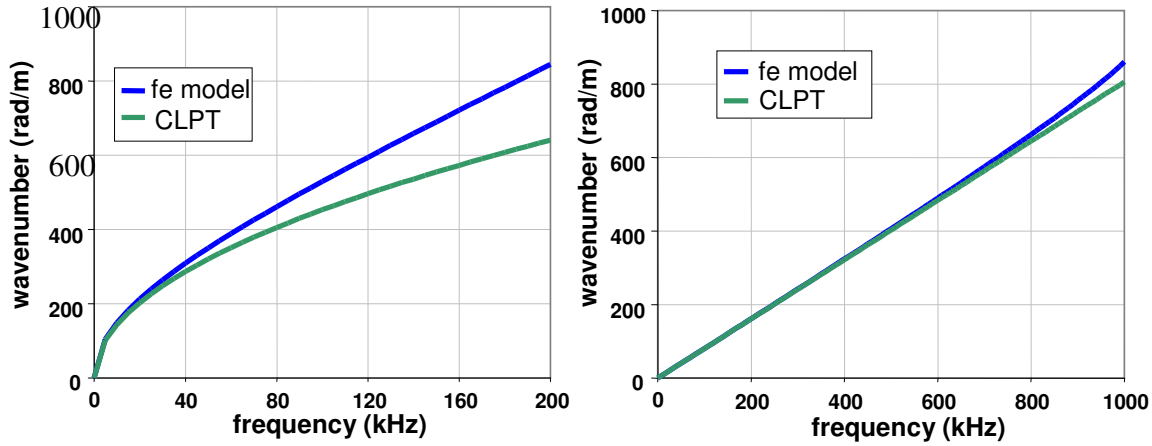

(c) A0 mode (90° direction) (d) S0 mode (90° direction)

Figure 6.2: Wavenumber-frequency relationships for the $[90/0/090]_{6s}$ layup

6.2.3 Wavenumber filtering

Sensor arrays can be used as wavenumber filters in much the same way as temporal filters act on frequencies [40]. The wavenumber filtering technique is able to eliminate unwanted information using the set of sensor responses. The transient signals of each sensor are weighted by a gain function and consolidated together to form the sensor array signal, given by

$$\psi(t) = \sum_{i=1}^{N} \phi(x_i) w(x_i, t) \tag{6.12}$$

where $\phi(x_i)$ is the gain applied to the sensor located at x_i. The different weights applied to the group of sensors determine the filtering properties of the array response. As a result, a wave arriving from a specific direction can be isolated by an appropriate choice of gains. At each temporal frequency corresponds a spatial frequency in the structure, the wavenumber. The wavenumber defines both the

direction that the wave propagates and the angle that the wave travels relative to the array axis. The sign of the wavenumber corresponds to the direction of the wave propagation. For a sensor array oriented along the x-axis, a negative wavenumber corresponds to a rightward propagating wave. In the wavenumber domain, the leftward propagating waves occupy the right side of the axis (positive k) whereas the rightward propagating waves occupy the left side of the axis (negative k). The directional filter is able to separate the data and to solely give either the leftward propagating waves or the rightward propagating waves. The principle is the same as for a band-pass filter where only a band of frequencies is passed through. The choice of the weighting functions to obtain the leftward propagating waves is shown in the Figure 6.3. The array output, $\psi(t)$, can be expressed in the wavenumber domain using the Fourier transform.

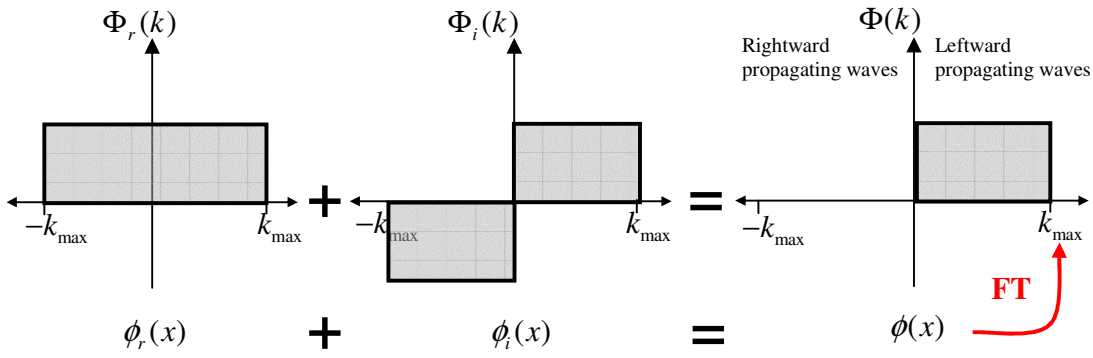

Figure 6.3: Weighting functions for the leftward filtering

The wavenumber filter would be composed of an even and an odd function in the wavenumber domain to separate the leftward propagating waves from the rightward propagating waves. The ideal filter would allow a single wavenumber to pass through, as shown in Figure 6.4.

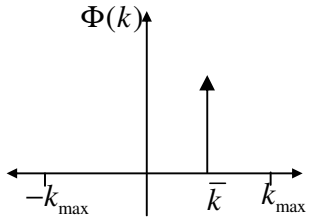

Figure 6.4: Ideal filter

The spatial weighting function corresponding to this ideal filter is:

$$\text{spatial domain: } \phi(x) = \frac{1}{2}\cos(\bar{k}x) + i\frac{1}{2}\sin(\bar{k}x) = \phi_R(x) + i\phi_I(x) \qquad (6.13)$$

$$\Updownarrow$$

$$\text{wavenumber domain: } \Phi(k) = \delta(k - \bar{k}) \qquad (6.14)$$

where $\bar{k}$ is the desired wavenumber to be passed through the filter. The discrete nature of the array limits the usable wavenumber to a maximum wavenumber analogous to the Nyquist frequency in temporal sampling. The finite number of sensors also implies that a band of wavenumbers will be filtered instead of one specific wavenumber. The capabilities of a discrete finite sensor array can be improved with the use of windowing functions along with the spatial weighting.

This filtering technique will be used along with the HHT to look at a specific direction and hence to infer the presence of delaminations and impact damage in composite plate structures.

6.3 Composite plate manufacturing

The construction of the laminate in the present study uses the carbon fiber pre-preg IM7/8552 manufactured by Hexcel Composites. The material consists of

unidirectional carbon fibers (IM7) impregnated in an epoxy resin (8552) with a nominal volume fraction of 57%. The properties of the material are presented in the Table 6.1.

E_L (GPa)	E_T (GPa)	υ_{LT}	G_{LT} (GPa)	ρ (kg/m^3)	t_p (mm)
170	11	.31	5.0	1430	.173

Table 6.1: IM7/8552 material properties

The composite plate was manufactured using a hand lay-up technique. Appropriate plies were cut out and laid up as a $[90/0/0/90]_{8s}$ laminate. The geometric configuration of the plies is shown in the Figure 6.5.

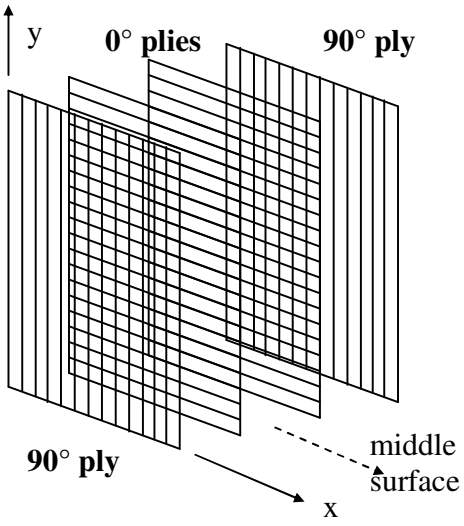

Figure 6.5: Layup geometric configuration

After being vacuum bagged to eliminate air gaps, the layup was ready for curing in the autoclave. The curing cycle for curing in one cycle the composite laminate is shown in the Figure 6.6. The resulting laminate was then cut into the plate of dimensions 35 by 24 in.

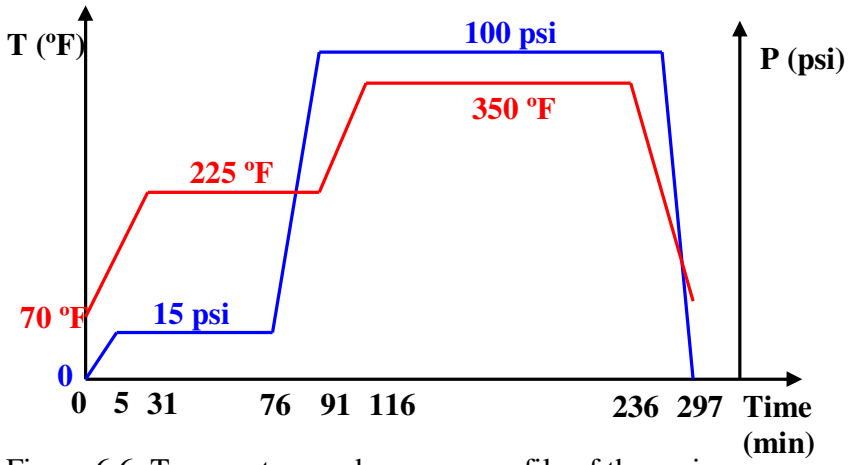

Figure 6.6: Temperature and pressure profile of the curing process

6.4 Delaminations detection and characterization

Delaminations arise in composite structures due to a variety of reasons. Defects in the manufacturing process, debonding or even impact damage can cause a delamination between the plies of the composite structures. Though not visible to the naked eye, a delamination leads to a loss in structural stiffness and strength and may conduct to catastrophic failure. Various attempts have been made recently to detect and characterize delamination growth in composite laminates.

6.4.1 Experimental setup

An experimental setup to examine delamination damage detection is shown in Figure 6.7. This experiment was conducted by Dr. Purekar for his research work [39]. A 6 plies orthotropic and symmetric composite plate was instrumented with a PVDF sensor array and a piezoceramic actuator. The plate was 35 inch long and 24 inch wide. A 1/8 in. × 1/8 in. PZT-5H patch actuator was bonded to the surface of the

laminate at the left edge and used to excite the structure with interrogating A0 waves. The actuation element creates a moment on the plate. This moment loading produces bending waves which are used for the damage detection. A sensor array was bonded in the middle of the plate. The array contained 19 circular sensor elements with a diameter of 1/16 in. and a spacing of 1/8 in. A tone burst signal of a given frequency and number of cycles was used to excite the actuator and the resulting transient responses were observed and recorded at each sensor locations of the array. The reproduction of a delamination damage was created by introducing a circular layer of Teflon between a 90° and a 0° ply in the middle of the plate. Two sizes of delamination were examined with Teflon patches of 1 in. and 2 in. diameters.

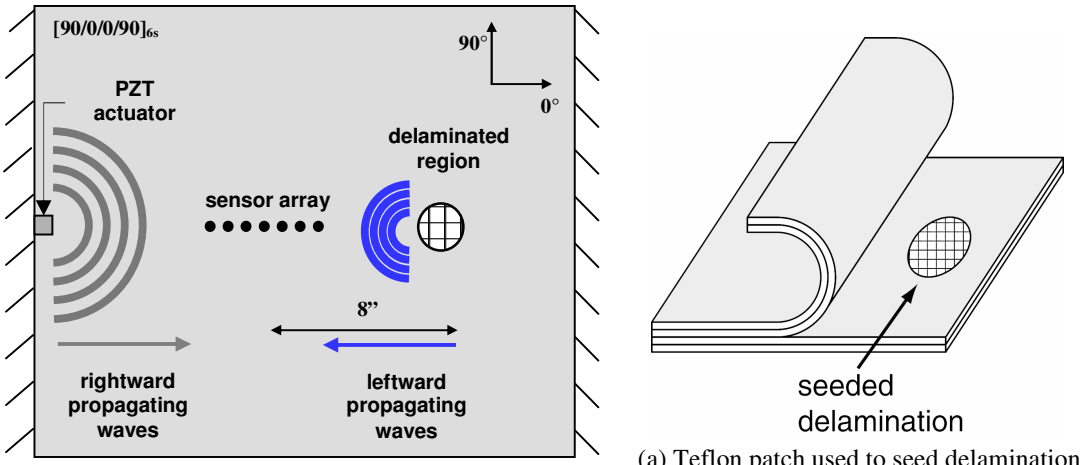

(a) Plate setup

(a) Teflon patch used to seed delamination

Figure 6.7: Experimental setup

6.4.2 Transient analysis

The plate was excited with a 7 cycles tone burst at a 80 kHz frequency. The middle sensor response shows no significant difference between the responses of the undamaged and delaminated plates, as shown in the Figure 6.8.

When the A0 lamb wave mode is excited, it propagates away from its origin. The energy will spread out in both space and time. Owing to dispersion and interaction with the damage, the measured signal will be a combination of the scaled and shifted versions of the excitation waveform as depicted in the Figure 6.8. An interference wavefront at .05 ms is still present in the signal and will be filtered out. The incident waves from the actuation element are located at .35 ms for each case whereas the reflections from the top and bottom edges arrive at .55 ms . A reflection waveform from the delamination should be comprised between the bottom/top edges reflections and the right edge reflection wave. A close observation of the transient signals does not point to the presence of damage in the structure despite slight differences. The reflection from the delamination in the damaged plates must be weak and is probably drowned out by the boundaries reflections. The empirical mode decomposition might be able to reveal these feeble reflections from delaminations if they exist in the transient signals.

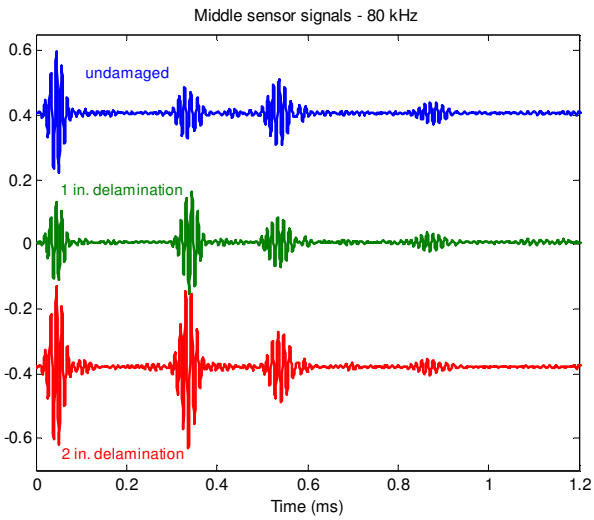

Figure 6.8: Middle sensor responses

6.4.3 Empirical mode decomposition

The EMD algorithm is applied to the undamaged plate and the delaminated plates. The results of the decomposition are given in the Figure 6.9, 6.10 and 6.11. The sifting process extracts one more IMF in the case of the undamaged plates than in the damaged plate. Even if the transient signals look the same, the EMD clearly detects a difference between the undamaged and the damaged cases. The deep inspection of the second IMFs shows an extra reflection in the delaminated decompositions. This reflection turns out to be very weak as expected and could correspond to the delamination reflection as shown in the Figure 6.12.

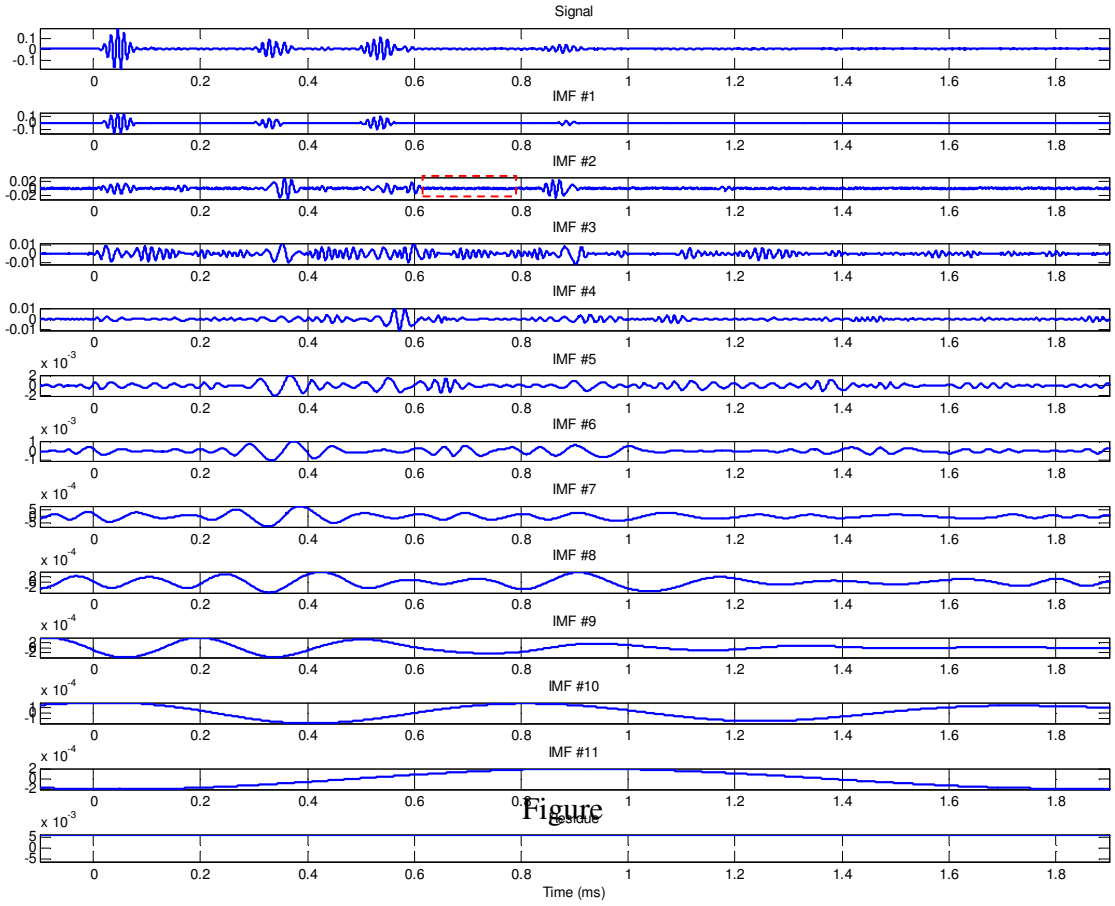

Figure 6.9: Empirical mode decomposition of the undamaged signal

The sifting process therefore extracts a new waveform in the second intrinsic mode. The amplitude of this reflection increases with the size of the delamination, which confirms the connection with the delamination.

The distance between the array and the delamination location can be determined based on the time interval between the incident propagating wave and the identified reflected wave from the delamination in the IMF #2.

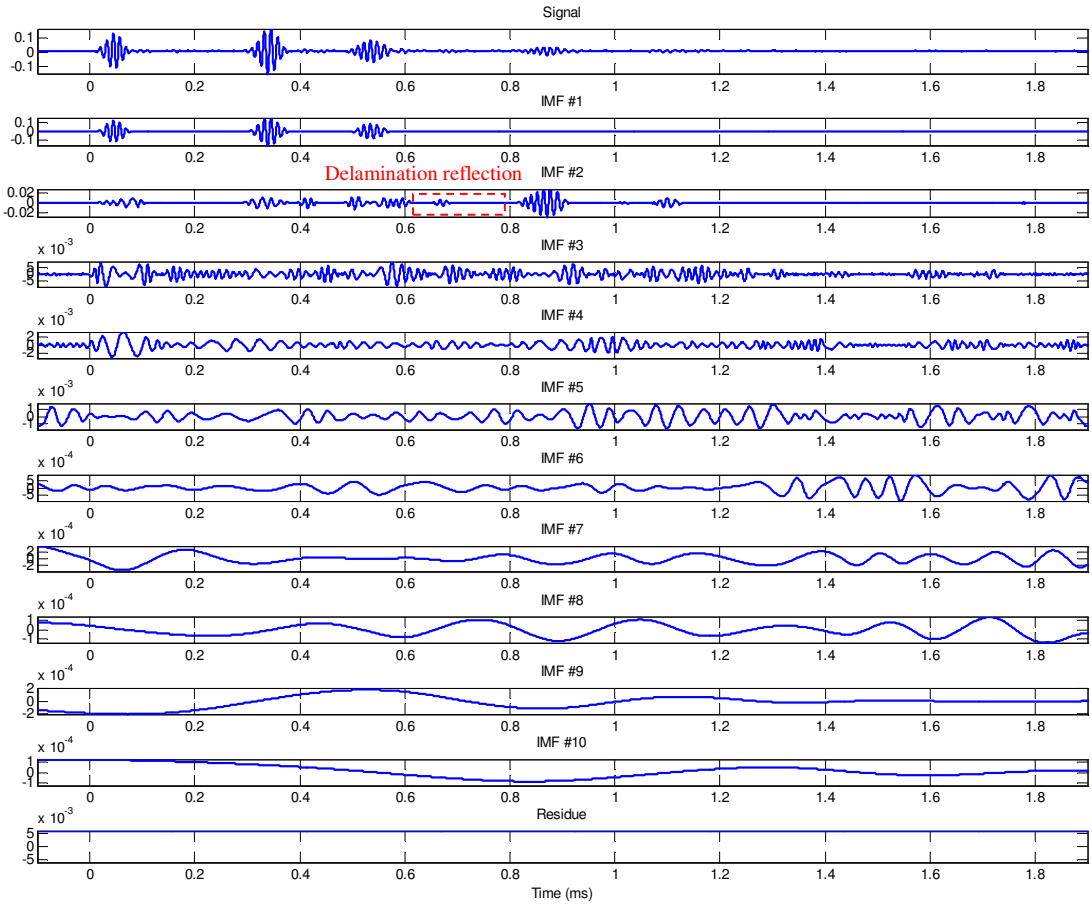

Figure 6.10: Empirical mode decomposition of the delaminated signal – 1 in.

The group velocity of the actuation signal is deducted from the wavenumber-frequency plot for the A0 mode along the 0° fiber direction. The delaminations

reflections are localized at 0.66 ms , which gives a time interval of $\Delta t = 0.31$ ms. With a group velocity of 1500 m/s , the delamination is estimated at 9.15 in., which is far from the exact solution of 8 in. The empirical mode decomposition cannot predict precisely the presence of the delamination from the hidden reflections revealed by the sifting process. The 15 % error on the location estimation suggests that weak reflections embedded in large reflections are hard to accurately extract in the time domain. However, the sifting process has shown again its capability to extract signal features.

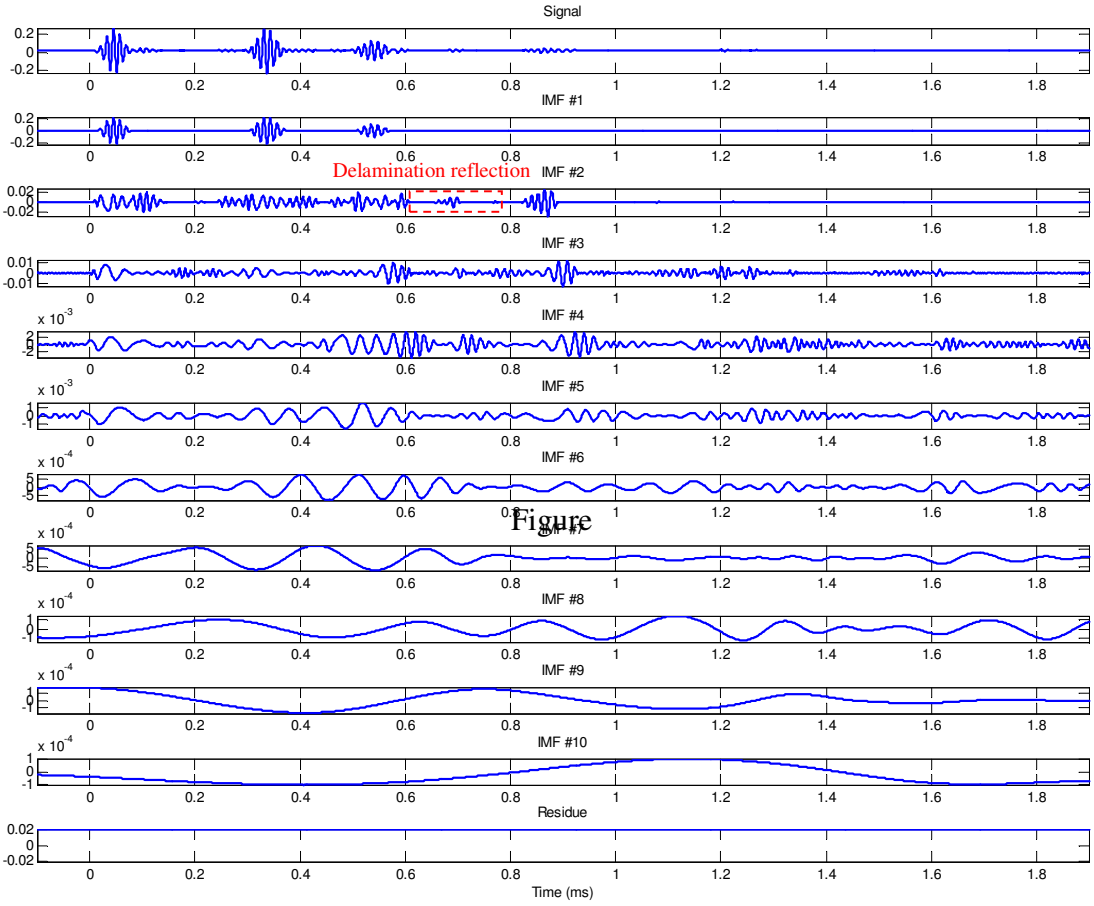

Figure 6.11: Empirical mode decomposition of the delaminated signal – 2 in.

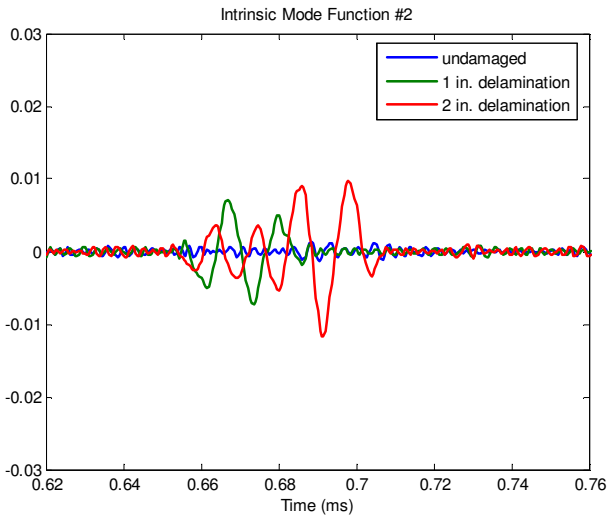

Figure 6.12: IMF #02

6.4.4 Directional filtering

The wavenumber filtering can be applied prior to the data processing with the EMD algorithm. The seeded delamination is positioned in the sensor array axis. As a result, the extraction of the leftward propagating waves should give information about the presence of the delamination. The rightward propagating signals represent the incident waves traveling toward the delamination whereas the leftward propagating signals reflect the interactions with the delamination. The plate is excited with a 7 cycles tone burst at 60 kHz. The middle sensor responses are shown in the Figure 6.13 along with the associated rightward and leftward signals. As with the 80 kHz case, there is no significant difference in the middle sensor signals for the undamaged plate and the delaminated plates.

There are number of observations that can be made from the analysis of the Figure 6.13

1. The rightward propagating signals from the undamaged and damaged cases shows no discernible difference.

2. The leftward propagating signals show a reflection in the delaminated plate cases at 0.6 ms that is not present in the undamaged case.
3. The reflection from the right edge of the plate is seen at 1.2 ms .
4. The reflections from the delaminations and the right edge are still weak in magnitude. Noise and interference corrupt these reflections and make their readability difficult.

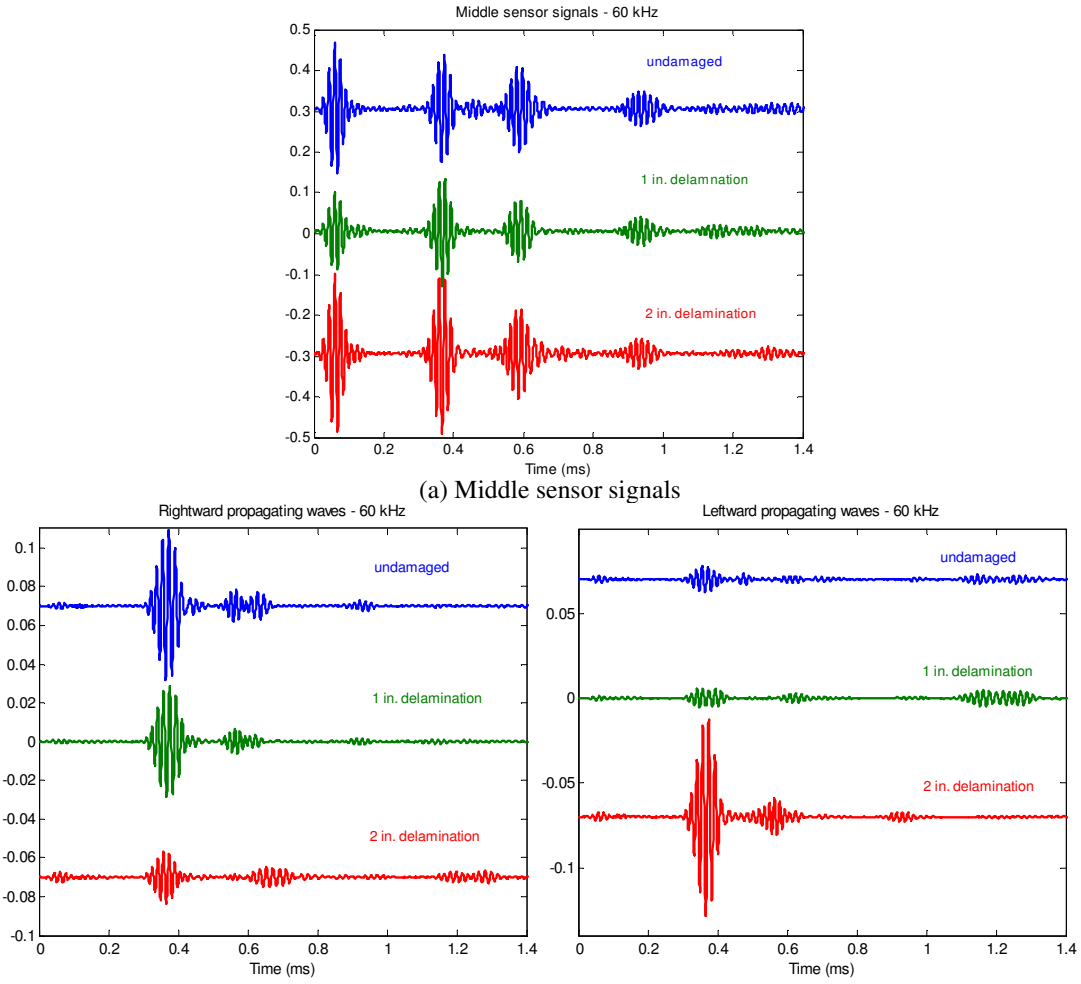

(a) Middle sensor signals

(b) Rightward propagation

(c) Leftward propagation

Figure 6.13: Directionally filtered response for 60 kHz excitation

The efficiency of the wavenumber filtering is in some way altered. The reflections from the delamination are still visible and increase with the size of the defect. An

approximation of the location of the delamination is also possible using the time of flight and the group velocity. This method gives approximately the same results as those in the previous section and will not be privileged to infer the delamination position.

6.4.5 Hilbert-Huang spectrum and the energy metric

The EMD associated with the Hilbert spectral analysis might clear up the leftward propagating signals to only display the reflection from the delamination. The Hilbert-Huang spectra for undamaged and damaged cases are plotted in Figure 6.14 in order to be analyzed in a damage identification purpose.

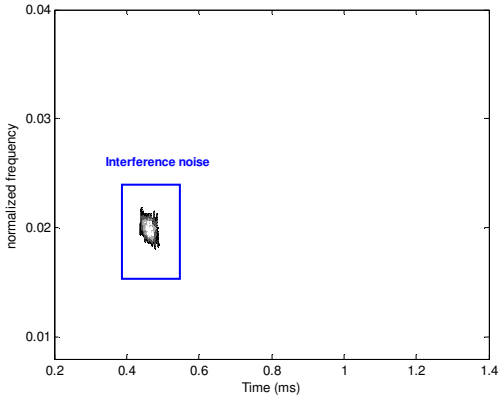

(a) Undamaged

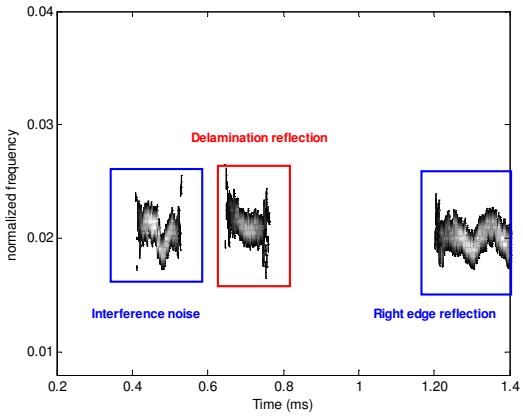

(b) Delamination #01

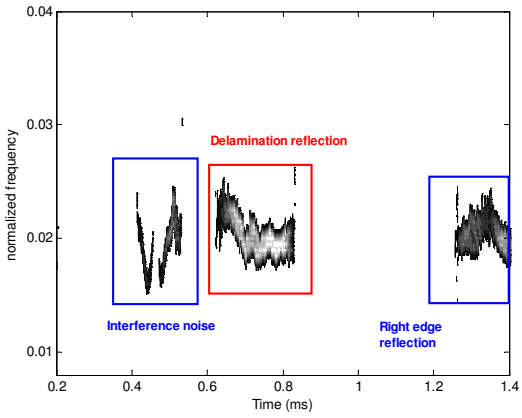

(c) Delamination #02

Figure 6.14: Hilbert-Huang spectra

The HHS is capable to localize the reflections from both delaminations in the leftward propagating waves. The reflections produced carry enough energy to be extracted in the energy-time-frequency representations. The right edge reflection is not visible for the delaminated plate #2. The energy released by the delamination makes the right edge reflection too weak to be represented. The computation of the energy density measurement of the reflected energy bands from the delamination are summarized in the Table 6.2:

	Delamination diameter		
	Und.	1”	2”
Freq.	60KHz		
E	7.7e-7	0.0010	0.0018

Table 6.2: Energy density measurement of the reflected frequency band – Delamination experiment

The size of the delamination can therefore be inferred through the reflected energy released in the structure. This energy increases upon the defect growth. An interpolation trend to predict the extent of the damage would not be relevant since only two sizes of delamination were experimented. The Hilbert-Huang spectrum allows a better interpretation of the propagation in a composite plate with seeded delaminations. The quantification of the delamination extent is possible through the reflected energy.

6.4.6 The Hilbert phase

As described in the Chapter 4, the Hilbert phase is an interesting feature to investigate for damage detection purposes. The Hilbert phase is based on the instantaneous phase functions issued by the Hilbert transform of IMFs. The total instantaneous phase is the sum of the instantaneous phases corresponding to each IMF and is defined as,

$$\theta(t) = \sum_{i=1}^{n} \arctan\left(\frac{H[c_i(t)]}{c_i(t)}\right) \tag{6.15}$$

Because of the IMFs properties, the Hilbert phase monotonically increases as a function of time. The EMD is first applied to the transient middle sensor signal, gathered by the sensor array. The actuation frequency considered for this study is set at 40 kHz. The Hilbert phases are then computed for the unfiltered set of data and plotted in the Figure 6.15.

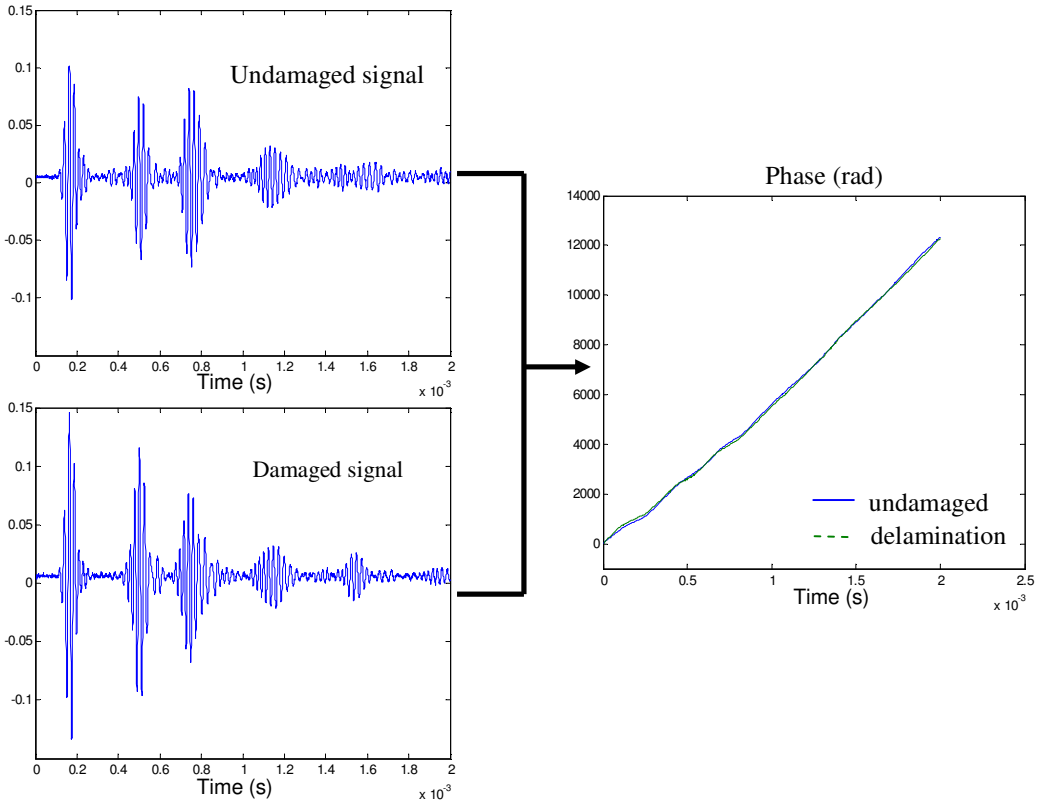

Figure 6.15: Hilbert phase of the unfiltered set of data

The Hilbert phases turn out to have the same behavior for both undamaged and delaminated cases. The presence of damage through the Hilbert phase appears as a slope change. In this case, the Hilbert phase does not detect any slope change and consequently cannot infer the presence of the delamination in the structure. The same analysis on the filtered set of data leads to the Hilbert phases in the Figure 6.16.

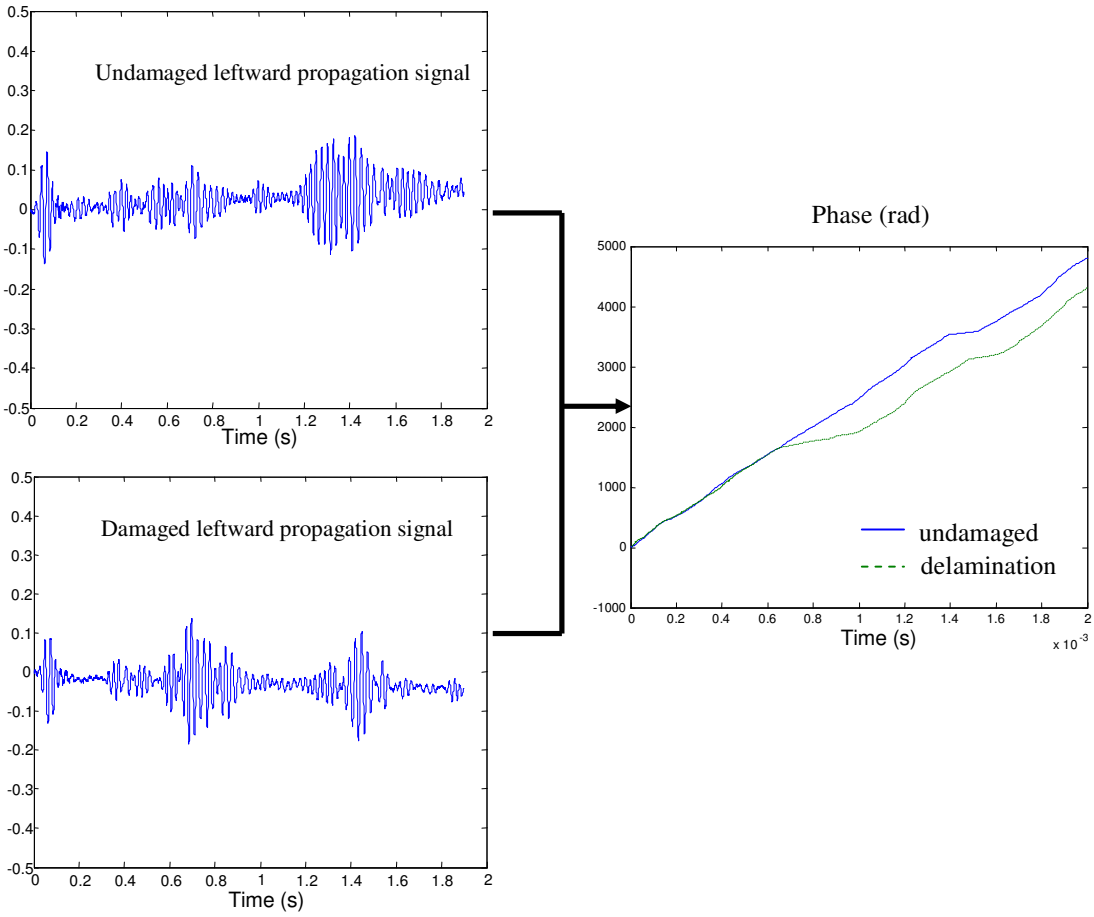

Figure 6.16: Hilbert phase of the directionally filtered set of data

The delamination is now detected in the Hilbert phase plot by the slope change that occurs 0.7 ms . The slope change happens at the moment where the traveling wave meets the left side of the delamination. Once the wave passed through the

delamination, the slope of the damaged phase behaves as the undamaged slope. The speed at which energy traverses the structure is altered by the delamination and is reflected as a slope deviation in the Hilbert phase. The sudden change of the energy propagation therefore allows the localization of the delamination in the composite plate. The next problem is to investigate if the Hilbert phase is able to track the increasing delamination in the structure. In this purpose, the Hilbert phase of the undamaged plate and the two delaminated plates are compared in the Figure 6.17.

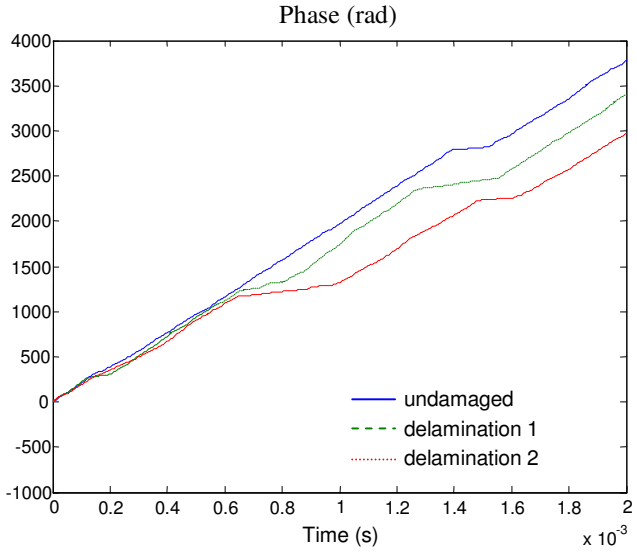

Figure 6.17: Hilbert phase

The 2 in. diameter delamination is also detected by the Hilbert phase and is characterized by a wider step than in the 1 in. delamination case. This longer slope deviation means that the wave needs more time to be transmitted through the delamination. As a result, the wave speed is reduced for a longer time than in the case of the smaller delamination. This behavior confirms the observations made by Hayashi and Kawashima [62]. When the A0 Lamb wave encounters a delaminated

region it transmits through the entrance of the delamination with little reflection. The transmitted wave splits into two independent waves which propagate at slower speeds then the incident wave. The Hilbert phase is not only able to detect the presence of the delamination but also to quantify its size. A mean phase error is proposed to evaluate the extent of the delamination and is defined as:

$$E = \sqrt{\frac{\sum_t \left[\theta_{dam}(t) - \theta_{und}(t)\right]^2}{\sum_t \theta_{und}(t)^2}} \tag{6.16}$$

where θ_{dam} represents the damaged phase and θ_{und} the undamaged phase. The results of the damaged index are shown in the Figure 6.18 and the interpolation trend based on the mean phase error seems to follow a parabolic curve. The estimation of the delamination size is therefore theoretically possible.

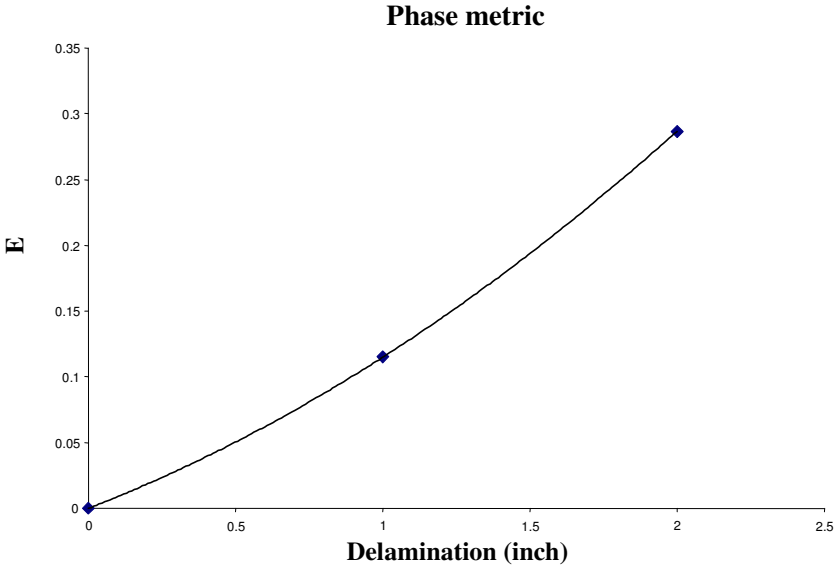

Figure 6.18: Mean phase error interpolation fit

The Hilbert phase turns out to be the best technique among the developed damage detection schemes for delamination detection in composite plate structures. The

Hilbert phase is able to accurately detect and quantify the presence and the extent of the seeded delaminations in the composite plates.

6.5 Mass loading

A common way to simulate defect interactions with the wave propagation is to locally modify the mass of the structure. Artificial damage can therefore be introduced, causing local loading. This damage simulation method allows to not physically damage the plate and makes it reusable for other experiments. Different sizes of damage can also be tested without having to manufacture other plates. A non-axis damage detection scheme could also be investigated since all the experiments so far were considering defects aligned with the sensor axis.

6.5.1 Experimental setup

A new experiment was set up and conducted with a 8 plies composite plate [0/90]s, the setup of which is shown in the Figure 6.19. The plate was instrumented with a piezoceramic actuator and a PVDF sensor array. A 1/4 in. × 1/4 in. PZT-5H patch actuator was bonded to the surface of the laminate at the left edge and used to excite the structure with interrogating A0 waves. A sensor array was bonded at a distance of 12 in. from the actuation element. The array contained 19 circular sensor elements with a diameter of 1/8 in. and a spacing of 1/4 in. Such array with bigger sensors than the previous experiment allows stronger response signals but a lower cut-off frequency. However, this experiment looks at the A0 actuation mode, which means low-frequency excitations. The plate was 35 inch long and 24 inch wide. A tone burst

signal of a maximum frequency of 60 kHz and 5 cycles was used to interrogate the plate and the resulting transient responses were observed and saved for each sensor of the array. Artificial damages were introduced in the form of bonded circular aluminum masses, causing local mass addition. These masses were glued on a plate and removed applying shear forces. Three different sizes of mass were tested as shown in the Figure 6.19.

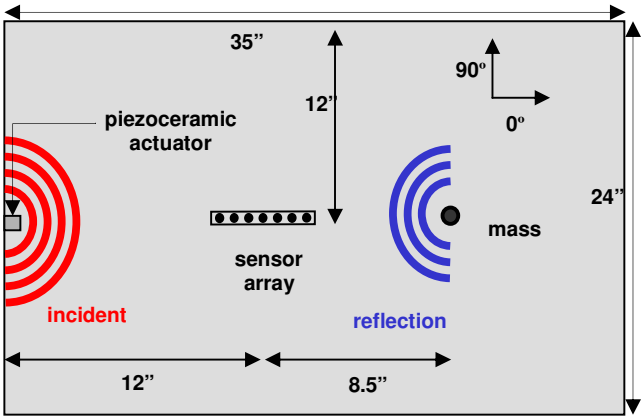

(a) Plate setup

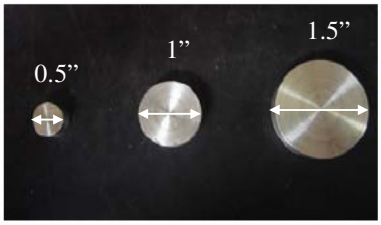

(b) Artificial damage

Figure 6.19: Experimental setup

6.5.2 Damage along the array axis

6.5.2.1 Transient analysis

The first configuration experimented is the one depicted in the Figure 6.19. The damage is located on the same axis as the array in order to get the reflection back from the mass. The set of data is gathered for an actuation frequency of 40 kHz. The sensor #6 response is shown in Figure 6.20 for the undamaged case and the three damaged cases. The A0 mode actuation wave is located at □.3 ms whereas the reflections from the top and bottom edges arrive at □.6 ms. The reflection from the right edge can also be seen at □1.0 ms.

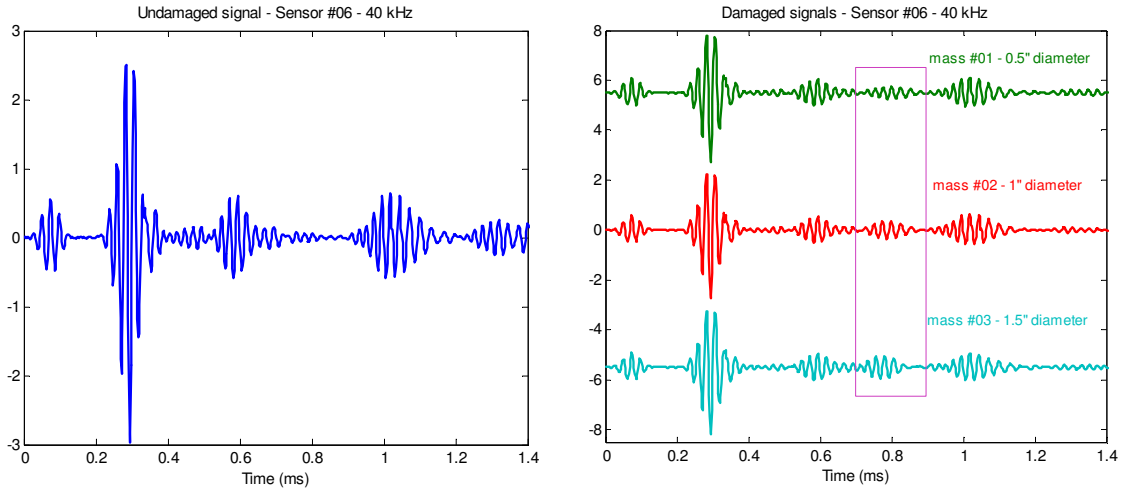

(a) Undamaged (b) Damaged

Figure 6.20: Sensor #06 response signals

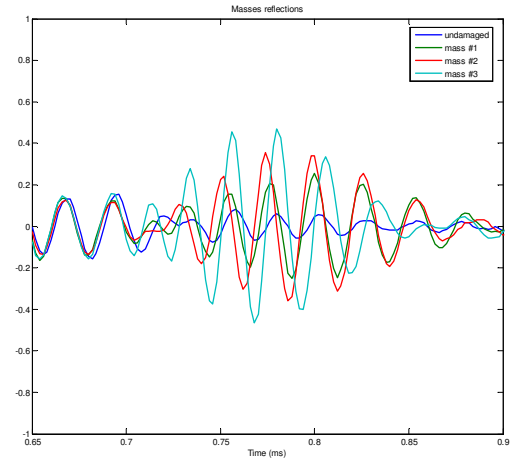

Figure 6.21: Reflections from the damage

If a reflection from the artificial damage is present in the signal, it should be visible between the top/bottom edge reflection and the right edge reflection. As seen in the Figure 6.20, waveforms corresponding to the damage reflections appear at 0.8 ms . The magnitude of these reflections increases with the size of the mass as shown in the Figure 6.21. The observation of the transient signals therefore indicates the presence of a discontinuity in the structure. The reflections from the masses are big enough to

be revealed in the transient signals. Larger sensor elements enable stronger response signals and thus a better distinction of the waveforms from the noise present in the signals.

6.5.2.2 Hilbert-Huang spectrum and Energy metric

The intrinsic mode functions provided by the EMD are not analyzed for this case study since the reflections from the damages are perfectly visible on the transient signal. The Hilbert-Huang spectra are plotted in the Figure 6.22 in order to quantify the amount of damage from the reflected energy bands.

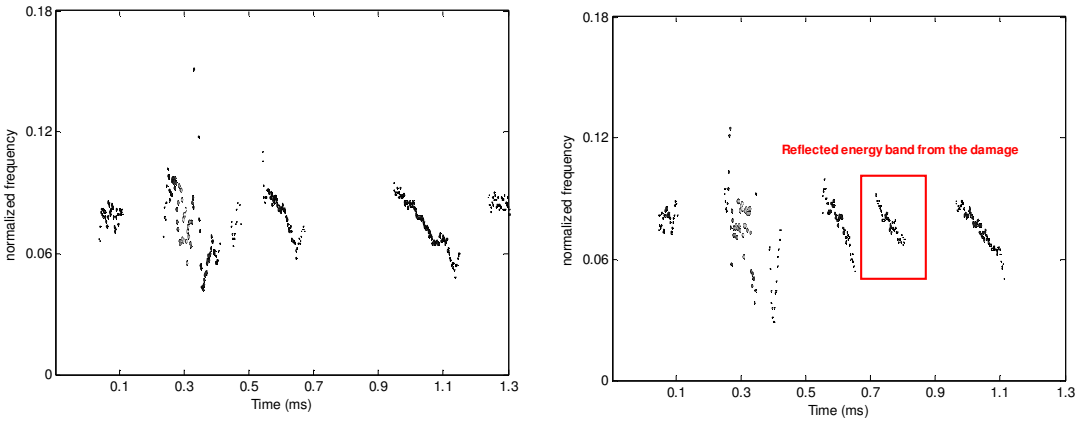

(a) Undamaged (b) Damaged

Figure 6.22: Hilbert-Huang spectra

The observation of the time-frequency responses of the transient signals revealed an extra frequency band in the damaged case. As expected, the reflection of the artificial damage seen in the transient signal is reported in the time-frequency representation. This reflection appears to happen between .7 ms and .9 ms . The maximum of the waveform corresponding to the reflection in the energy-time spectrum will give the

exact time of flight. The reflected energy band metric can now be applied to quantify the masses size.

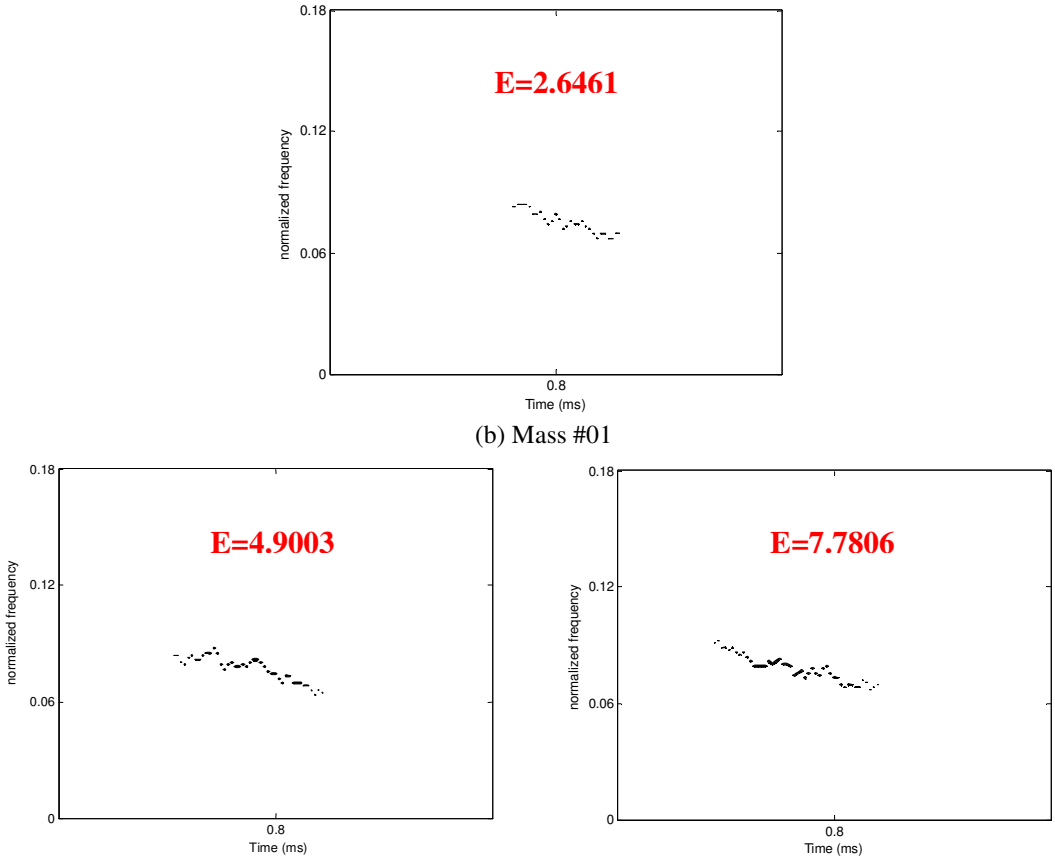

(b) Mass #01

(c) Mass #02

(d) Mass #03

Figure 6.23: Energy density measurement of the reflected frequency band

The energy released by the wave upon the damage growth increases with the size of the masses. These results are similar than for the isotropic plate with holes drilled in the structure. The energy increases linearly with the diameter of the masses as shown by the interpolation trend in the Figure 6.24. The prediction of the damage size from the released energy is therefore possible with the linear fit.

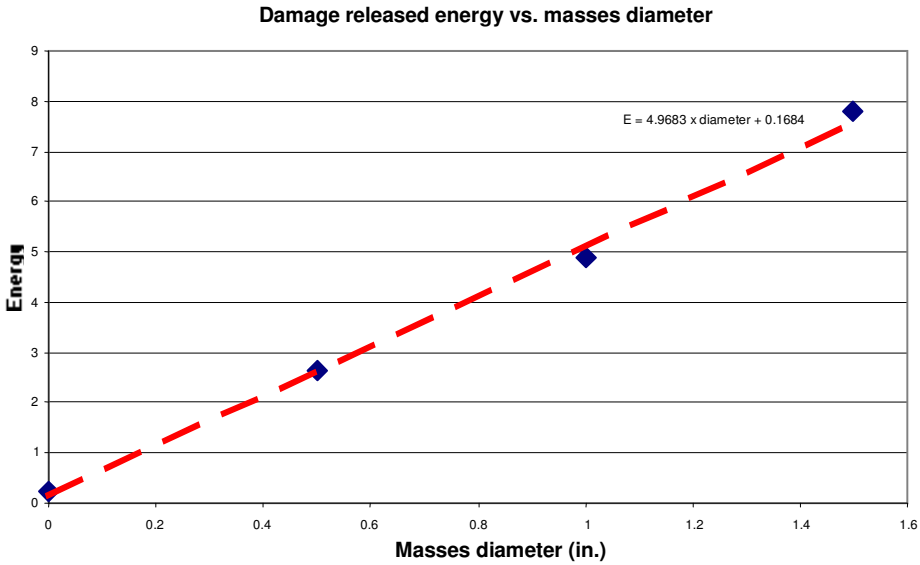

Figure 6.24: Prediction trend of the damage size

6.5.2.3 Energy-time spectrum and the Phase shift metric

The importance of the determination of the time interval between the actuation wave and the reflection waveform has been over-emphasized in the previous experiments. The best method to obtain the time of flight is to look at the energy peaks on the energy-time spectrum for the IMF component containing the highest energy. Thus, the energy-time spectrum for the first IMF is plotted in the Figure 6.25.

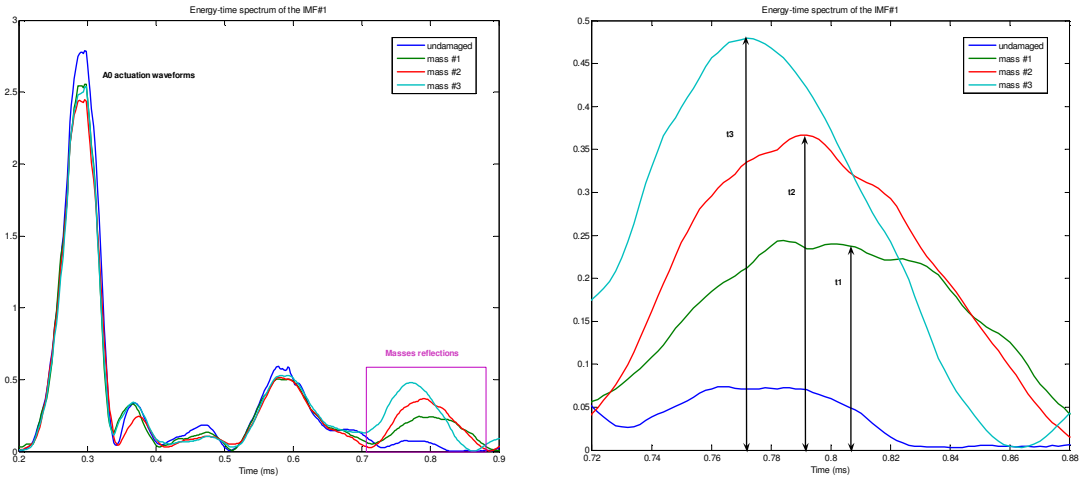

Figure 6.25: Energy-time spectrum of the IMF #01

From the time of flight and the A0 group wave velocity, the location of the damage can be inferred. However, the A0 group velocity is unknown for this new plate since the plate thickness is different. The wavenumber-frequency curves need to be reconstructed for the A0 mode along the 0° and the 90° fiber directions. The CLPT theory is retained to compute the wavenumber-frequency relationships since it has shown good correlation with the FEM model of Purekar [39] until the 40 kHz frequency. Above this frequency, the CLPT predictions are not accurate enough and the shear deformation must be taken into account. As demonstrated in the Section 6.2.1, the wavenumber-frequency relationship for the A0 bending mode is given by the CLPT theory and defined as

$$\begin{cases} \text{x-dir.: } \left(w(x,y) = w_0 e^{i(\omega t - kx)}\right) & \rightarrow \quad k = \sqrt{\omega}\sqrt[4]{\dfrac{m}{D_{11}}} \\ \text{y-dir.: } \left(w(x,y) = w_0 e^{i(\omega t - ky)}\right) & \rightarrow \quad k = \sqrt{\omega}\sqrt[4]{\dfrac{m}{D_{22}}} \end{cases} \tag{6.17}$$

with $D_{11} = \frac{1}{3}\sum_{k=1}^{N}[Q_{11}]_k \left(z_k^3 - z_{k-1}^3\right)$ and $D_{22} = \frac{1}{3}\sum_{k=1}^{N}[Q_{22}]_k \left(z_k^3 - z_{k-1}^3\right)$ for a 8 plies symmetric laminate $[90/0/0/90]_{8s}$. The different Q_{11}, Q_{22} and z_k are deducted from the material property given in Table 6.1 and from the layup configuration. The mass of the plate is determined from the material density and the volume of the plate. Once the bending stiffness coefficients and the mass are computed, the wavenumber-frequency curves are plotted as shown in the Figure 6.26. From this curve, the phase speed can be easily deducted from the relation $c_p = \frac{\omega}{k}$ and for the A0 mode $c_g = 2c_p$. Once the group velocity is determined, the location can be inferred. For the present

case, the estimation of the distance between the sensor #6 and the damage is 10.47 in.; the exact solution being equal to 10 in.

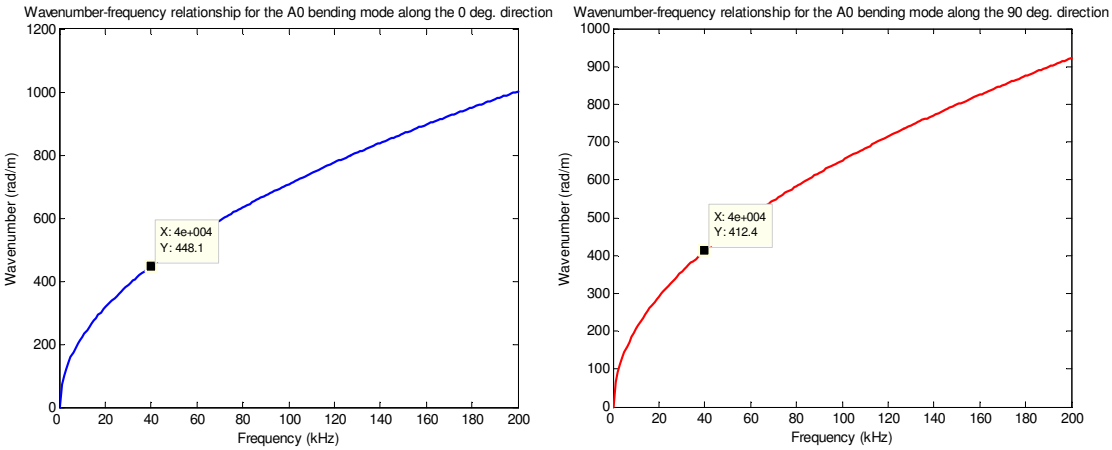

(a) A0 mode (0° direction) (a) A0 mode (90° direction)

Figure 6.26: Wavenumber-frequency relationships for the $[90/0/090]_{8s}$ layup

The quantification of the increasing damage is also possible using the same approach developed for the damage detection in isotropic plates. Assuming the knowledge of the size and shape of the initial damage, the formula $D2 = c_g \times \left(\frac{TOF\ 2 - TOF\ 1}{2} \right) + D1$ gives the diameter of the new extent damage.

6.5.2.4 The Hilbert phase

The Hilbert phase has shown promising results for the detection of seeded delamination in composite plates. The use of this technique for this experiment is thus investigated. The phases for the undamaged and damaged cases are plotted in the Figure 6.27.

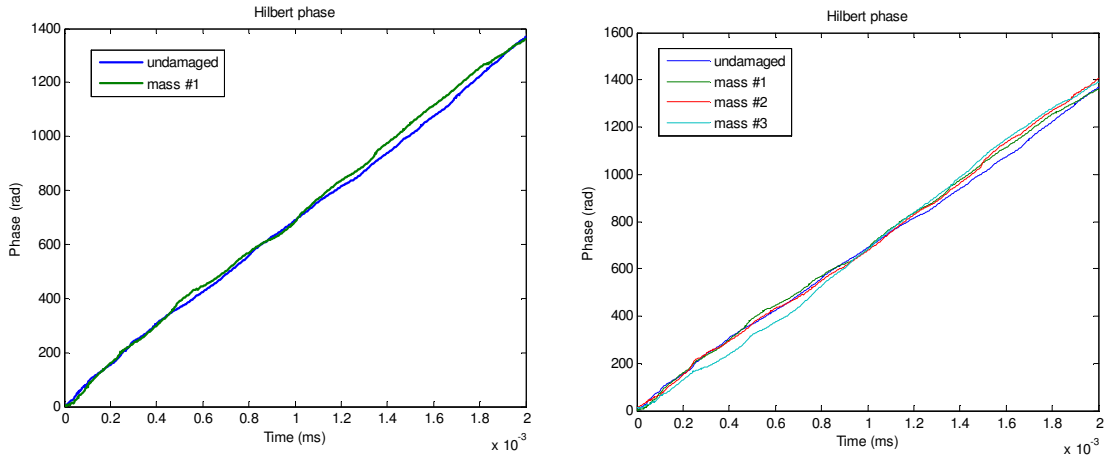

Figure 6.27: Hilbert phase

The results are less convincing than for the delamination experiment. Though a slope change is discernible, the presence of the damage is not obvious. The undamaged and damaged phases are really close even if a slope change occurs at 1. ms indicating the presence of damage. Such behavior can be explained by some reasons. First of all, the Hilbert phase is a very sensitive parameter. As proved by Salvino and Pines [34], the phase value varies with the structural parameters as mass, damping, stiffness. A slight change in one of these parameters will influence the phase behavior. Second of all, the type of windowing applied to the transient signals before the EMD analysis also affects the phase through the spline fitting. Third of all, the bonding of the mass on the plate is not perfect. The masses were mounted on the plate with M-Coat and then demounted. This operation was realized three times. Despite the efforts put to clean the plate after demounting a mass, some imperfections may have modified the wave propagation within the damage. The results of the mean phase error computation are given in the Table 6.3.

	Mass diameter (in.)		
	0.5”	1”	1.5”
E	0.0280	0.0344	0.0579

Table 6.3: Mean phase error results

Although the slope change is barely visible, the mean phase error metric increases with the size of the damage. The Hilbert phase is still able to locate and quantify damage in composite plate. However, the energy and phase shift metrics turned out to be more efficient for this experiment.

6.5.2 Non-axis damage detection

The different damage detection schemes have been applied with success to defects oriented along the array axis. This simple configuration allowed a direct interpretation of the gathered transient signals since the reflection from damage could be seen. A damage positioned at a certain angle with respect to the array axis is more difficult to locate. The same type of experiment than in the previous section is conducted. In this case, the mass is placed at 45° with respect to the array axis as shown in the Figure 6.28.

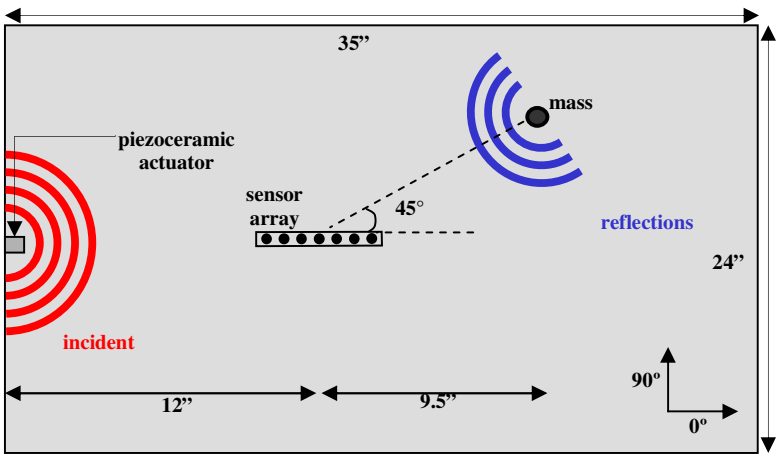

Figure 6.28: Non-axis damage detection setup

The transient signals obtained for this setup configuration are given in the Figure 6.29.

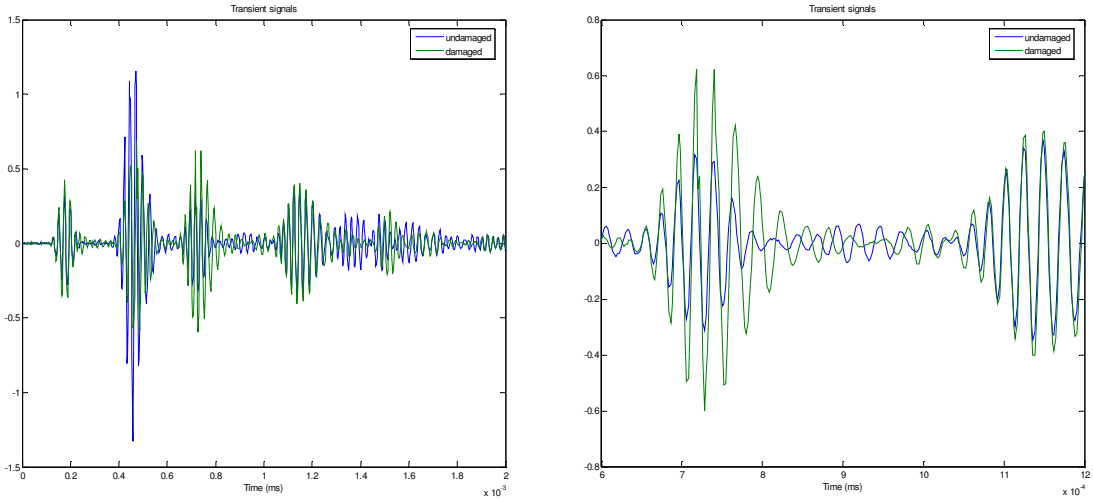

Figure 6.29: Middle sensor responses

The time-domain signals show no significant qualitative difference between the responses of the undamaged and damaged plates. The reflection from the artificial damage is not visible anymore. However the reflection from the top/bottom edge looks greater and longer in time for the damaged case as seen in the Figure 6.29. This observation leads to the assumption that the reflection from the damage and the reflection from the top/bottom edges might be superimposed. The empirical mode decomposition could confirm this supposition. The first two extracted IMFs are shown in the Figure 6.30. The comparison of the first IMFs does not bring any information for a damage detection purpose since it roughly corresponds to the original signal without noise. The second damaged IMF is more explicit with the presence of a new reflection that does not occur for the undamaged case. This

waveform turns out to have the same shape and number of cycles than the excitation signal.

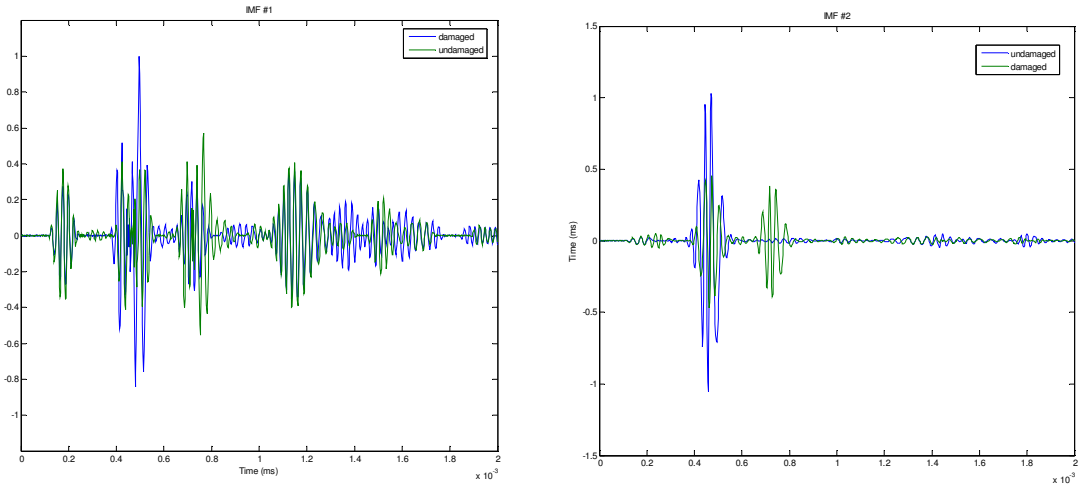

(a) IMF #01 (b) IMF #02

Figure 6.30: Extraction of the first two IMFs

Owing to dispersion and interaction with the damage, the measured signal is a combination of the scaled and shifted versions of the excitation waveform. As a result, the initial assumption is confirmed and the reflection from the damage was embedded in the top/bottom edges reflection. The different time scales allow the empirical mode decomposition to make the distinction between both reflections. In fact, the decomposition is based on the direct extraction of the energy associated with various intrinsic time scales. The reflection from the damage is therefore located in the second mode of the decomposition. The Hilbert-Huang spectra give a better description of the wave propagation and reflection in the plate as shown in the Figure 6.31.

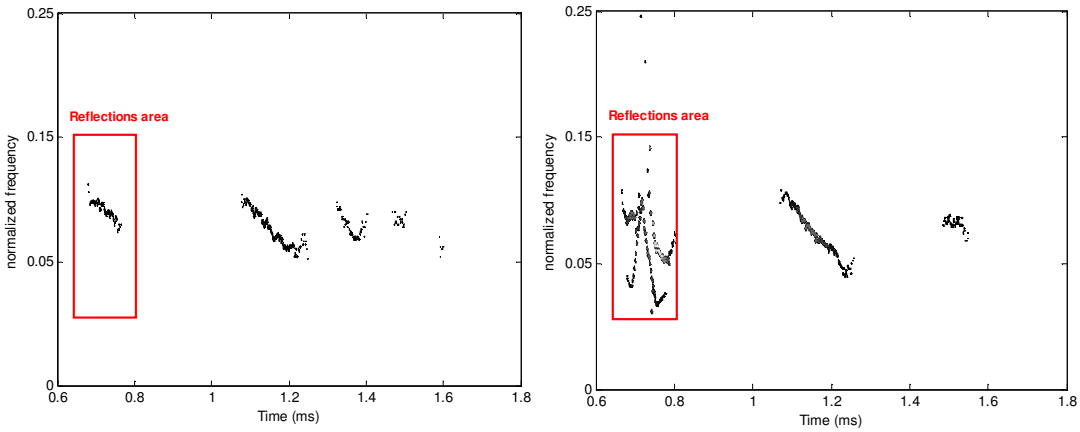

(a) Undamaged (b) Damaged (mass #2)

Figure 6.31: Hilbert-Huang energy spectra

The Hilbert spectrum of the damaged signal shows the summation of the different reflections between 0.6 and 0.8 ms as assumed. The presence of the damage can be inferred by the presence of the multi-reflection waveforms in the damaged cases. A bigger mass was then mounted on a plate and the corresponding time-frequency representation is plotted in the Figure 6.32.

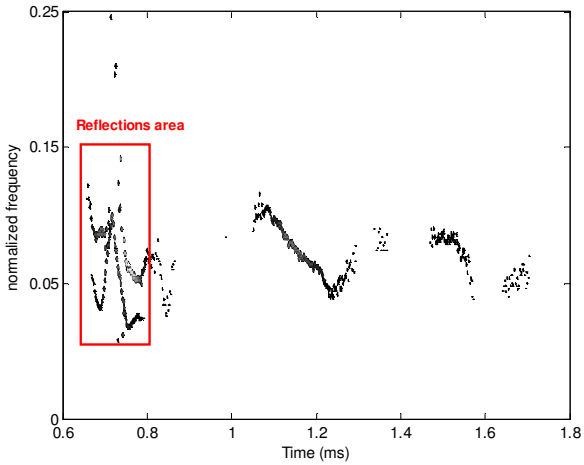

Figure 6.32: Hilbert-Huang spectrum corresponding to a bigger damage (mass #3)

The same behavior is observed. The energy-released measurement is applied in order to quantify the extent of the damage. As shown in the Table 6.4, the energy increases with the size of the damage even for a non-axis damage case.

	Mass diameter (in.)		
	0	1”	1.5”
E	10.1265	12.7428	14.5594

Table 6.4: Energy density measurement of the reflected frequency band – Mass experiment

Though the track of the increasing damage turns out to be possible, the determination of the position angle of the damage remains a problem. In this case, the time of flight technique cannot be used since the wave propagation characteristics along this angle are unknown. The Hilbert phase also localized the presence of the defect by a slope change around 0.6 ms, as seen in the Figure 6.33. The Hilbert phase looks thus consistent with the previous results.

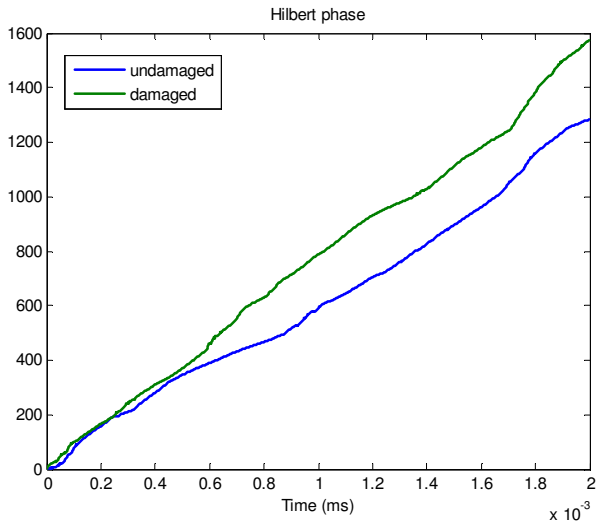

Figure 6.33 Hilbert phase

The different damage detection methods point out the presence of the damage through the reflection extracted in the second mode. However, more information is needed to figure out the exact location of the damage. A triangularization technique could be examined where elliptical loci of possible crack positions will be constructed based on the flight time of crack-reflected waves. This solution would imply at least 3 different sensors and the knowledge of the ellipses equations for the composite wave propagation. Such technique was used by Tua, et al. [32] for damage location in aluminum plates. The EMD associated with the Hilbert spectra analysis is capable of detecting and quantifying the damage with one sensor element for non-axis damage position. The location of the crack remains though unknown.

6.6 Low-velocity impact damage

The previous experiments aimed to validate the HHT as a damage detection tool and were based on seeded damage. The HHT shown promising results on seeded delamination and local mass loading detection. A real-world application is now investigated to confirm the real potential of the HHT for a structural health monitoring system. As mentioned earlier, the most commonly encountered type of damage is caused by impact due to the low interlaminar strength of composites. The mechanical properties can be severely degraded as a result of a low-velocity impact even for barely visible damage. An impact on the structure can induce different type of damage as matrix cracking, delaminations and broken fibers. Such impact can occur in the reality if a worker accidentally drops a tool or if a bird crashes into the aircraft during the take-off. A good way to experimentally simulate a low-velocity

impact is to build a swinging pendulum mechanism. The energy of the impact could therefore be quantified through the potential energy and related to the damage growth.

6.6.1 Experimental Setup

The same plate used for the previous experiment is instrumented and setup along with a basic pendulum system. The identical smart structures technologies to actuate and sense the structure are also used. The pendulum mechanism is shown in the Figure 6.34

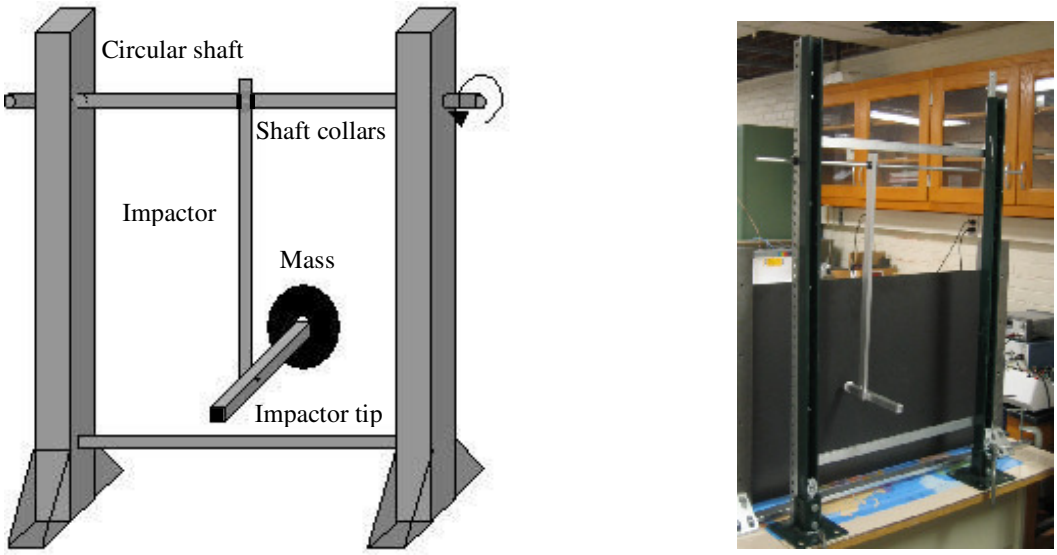

Figure 6.34: Swinging pendulum mechanism

A hammer type of impactor was conceived and was able to carry circular masses to increase the energy impact. The impactor was free to swing around a circular shaft introduced through the two columns. Shaft collars were used to avoid unwanted oscillations of the impactor instead of a bearing. Thus, some frictional effects are

neglected in this experiment and should be taken into account for a most accurate estimation of the energy released by the system. The experimental setup is pictured in the Figure 6.35. The horizontal position of the plate was chosen in order to avoid any bending after the impact.

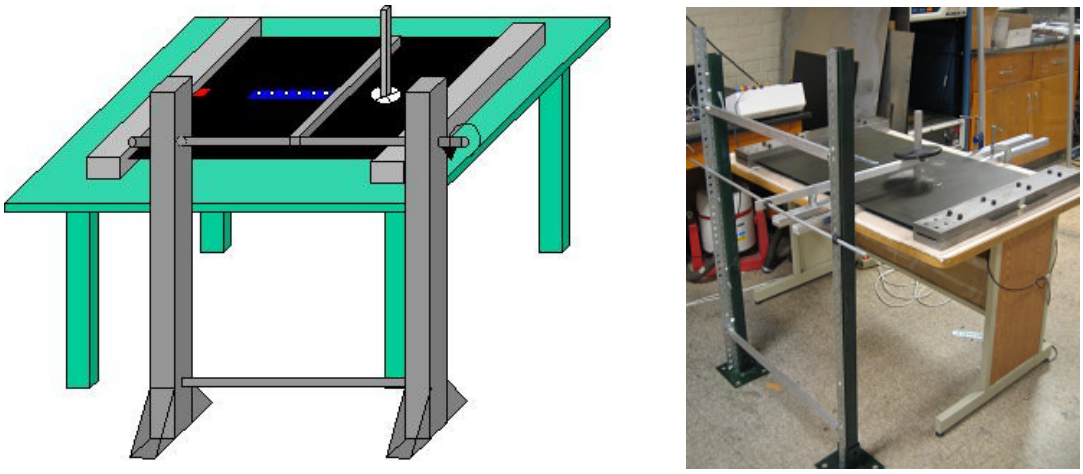

Figure 6.35 Low-velocity impact experimental setup

This experiment setup allows systematic impact as desired. For each impact, the response signals are gathered without removing the plate. The boundary conditions remain identical for every impact and thus will not influence the results. A picture of the impacted region is also taken after each impact. In this way, a correlation between the visual inspection of the plate and the signal processing results will be possible. Some damage could indeed occur between the plies without being visible at the surface of the structure. A preliminary study with a C-Scan system would allow to ensure that the impact produced damage and also to reveal the extent of this damage. Unfortunately the university does not own such equipment. Each impact starts at zero initial velocity and at a certain initial angle. The impact energy comes from the

gravitational potential energy. The experimental setup therefore makes pendulum impacts repeatable with only one varying parameter, the impact energy.

6.6.2 Impact energy quantification

The energy potential of a single mass pendulum is entirely from gravity and is given by the well-know formula:

$$E = mgL \tag{6.18}$$

where E is the gravitational potential energy, m the mass of the pendulum (the mass of the string is small enough to be neglected), L the pendulum length, and g the gravitational constant in the medium.

Let us take the zero of potential energy to be at a 90° angle of the swing, as shown in the Figure 6.36. When the pendulum is brought to a certain height before being released, the pendulum is higher than at the initial position of the swing, and the potential energy is equal to the weight of the pendulum multiplied by the change in height. If the pendulum has length *L*, the change in height is $L\sin\theta$ and the potential energy becomes:

$$E = mgL\sin\theta \tag{6.19}$$

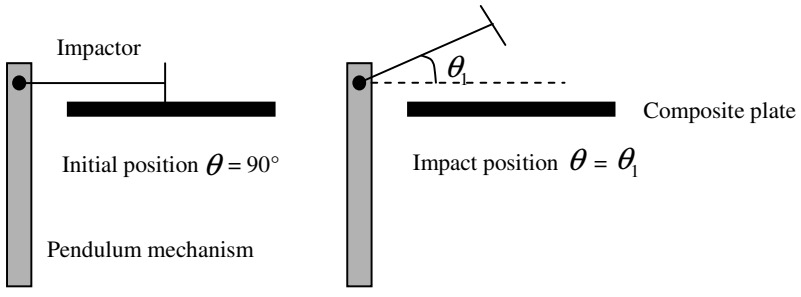

Figure 6.36: Potential energy calculation

In the study case, the pendulum is not limited at a single mass but at a hammer impactor with a significant weight. Thus, the impactor system will be replaced for the calculation by a single mass defined by its center of mass as shown in the Figure 6.37.

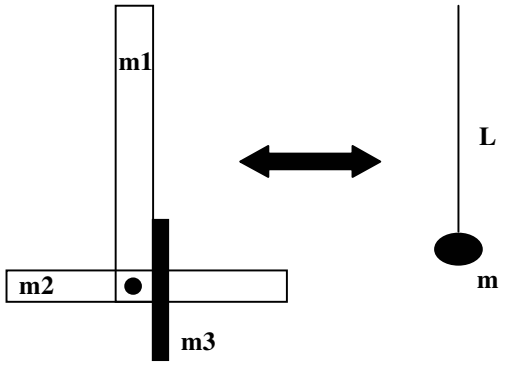

Figure 6.37: Impactor model

The center of mass is defined as the average of the constituting elements positions weighted by their masses. Each time a mass is added to the system, the center of mass changes. The values of the different parameters needed to compute the potential energy are summarized in the Table 6.5.

m1=0.562 kgs	m3 (kgs)	m (kgs)	L (m)
m2=0.225 kgs	0	0.787	0.424
	2.267	3.05	0.601
	4.536	5.32	0.625

Table 6.5: Potential energy parameters

The damage detection methodology follows these steps:

1. The plate is impacted. Each impact has more energy than the previous one. The initial angle is increased or a mass is added in this purpose.
2. A picture of the impacted region is taken.
3. The plate is interrogated by a tone burst at a 40 kHz frequency with 5 cycles. The response signals are observed and saved on a disk.
4. This set of data is processing with the HHT.
5. Repeat the process

The different impact cases with the corresponding potential energy are given in the Table 6.6.

Case #	Mass m (kgs)	Length L (m)	Initial angle θ (deg.)	Energy (J)
1	0.787	0.422	90	3.27
2	3.05	0.601	45	12.7
3	3.05	0.601	90	17.9
4	5.32	0.625	45	23.1

Table 6.6: Summary of the different impact cases

6.6.3 Transient signal analysis

A first undamaged set of data is taken as a baseline. The plate is then impacted and the middle sensor responses are examined in order to infer the presence of damage in the plate. A first impact of 3.27 J is applied and the middle sensor signals for the

undamaged and impacted plates are compared in the Figure 6.38. The location of the impacted region was chosen in order for the reflected waveform to be visible in the transient signals. The pendulum mechanism was therefore impacted the plate at a distance of 8.5 in. from the middle sensor as for the local mass loading experiment. If damage is created due to the impact, the reflected waveform should appear between the top/bottom edges and the right edge reflections. The observation of the transient signals in the Figure 6.38 does not give any information about the presence of damage due to the first low-velocity impact. The impact energy was then increased by adding a mass to the impactor and the middle sensor responses are plotted in the Figure 6.38. In this case, a difference can be seen between the undamaged and the impacted signals at .7 ms .

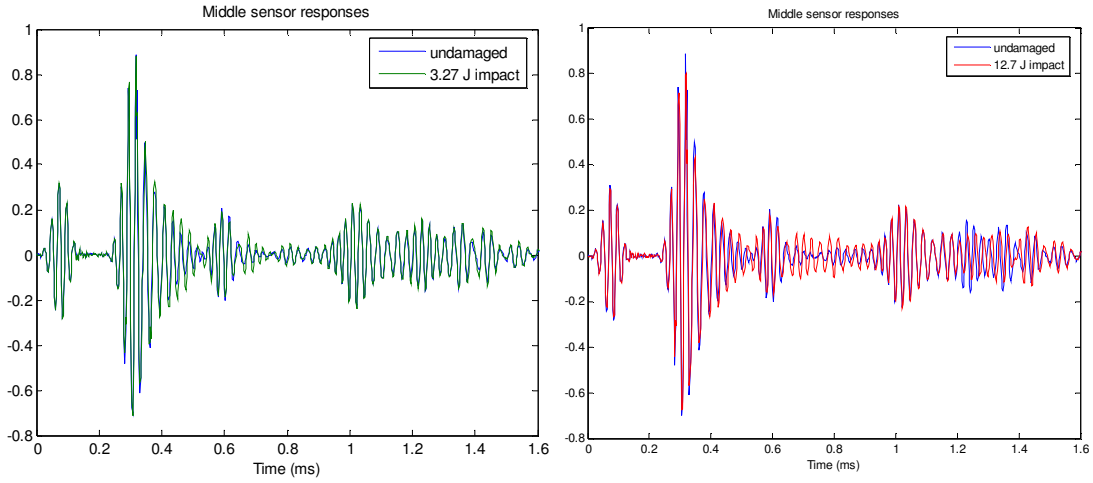

(a) Impact #1 (b) Impact #2

Figure 6.38: Middle sensor responses for the first two impact cases

A reflected waveform, though weak, shows up as expected in case of damage. The Lamb waves encounter a discontinuity through the thickness of the plate and part of the incident wavefront is reflected back. The middle sensor response is able to exhibit

this reflection. An impact of 12.7 J damaged the composite plate. A C-scan examination would precise the type of damage engendered by the impact. This NDE technique being not available, a visual inspection of the impacted region gives a good understanding of the impact consequence on the structure. A picture of both impacted region surfaces were taken and are shown in the Figure 6.39.

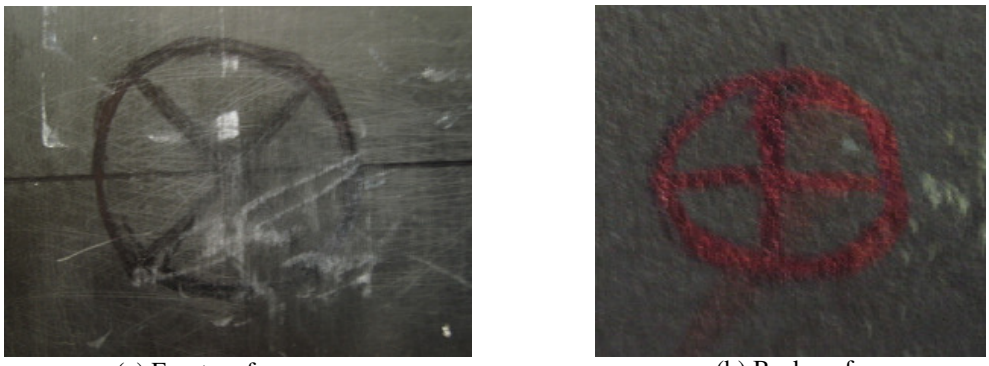

(a) Front surface (b) Back surface

Figure 6.39: Impacted region pictures

The observation of these pictures and a touch examination of the impacted region do not show the presence of any defects in the plate. The common visual inspection technique used for the structural health monitoring of composite structures would not detect the presence of damage in the plate. However, the transient response detects a discontinuity in the structure at the impact location. The reflected waveform localized by the sensor signal is nevertheless weak and needs to be effectively identified as a damage reflection. To accomplish this goal, the wavenumber filtering technique is applied to extract the leftward propagating waves. The damage reflection would be better characterized and quantified with this representation. The leftward propagating waves for the undamaged and the two first impacted cases are plotted in the Figure 6.40.

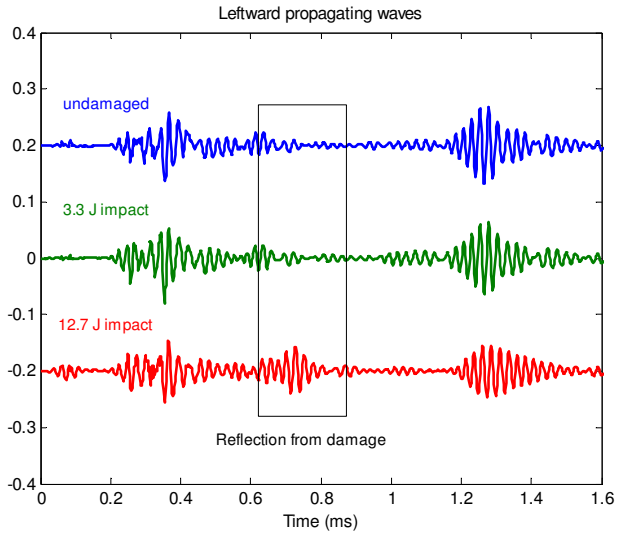

Figure 6.40: Leftward propagating waves – Impacted cases #1 and #2

The first impact does not affect the health of the composite plate. However, the leftward propagating waves for the impact of 12.7 J of energy confirm the presence of damage with a new waveform detected between 0.6 ms and 0.8 ms. Although invisible on both surfaces of the impacted region, damage is present in the structure. The source of impact damage may include delamination between plies, matrix cracking or broken fibers. The use of Lamb waves to interrogate composite structures enables subsurface damage that is invisible to the naked eye to be detected. A third impact is used to determine whether the damage region grows. The middle sensor response corresponding to this impact case #3 is plotted in the Figure 6.41 along with the picture of the impacted region. Again, a weak reflection is visible for the impacted case around 0.7 ms, that is not present for the undamaged case. In order to have a better idea of the magnitude of this reflection, the leftward propagation is also extracted and plotted in the Figure 6.42.

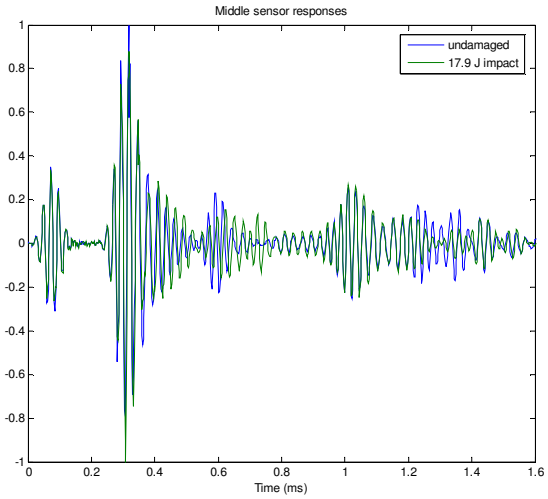

(a) Middle sensor responses

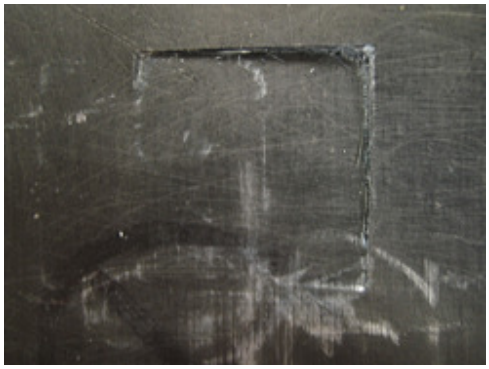

(b) Front surface picture

Figure 6.41: 17.9 J impact case

The picture of the front surface of the plate clearly shows that the composite structure is damaged. Broken fibers can be seen as well as matrix cracking. Compared to the previous impact, the damage is evident by visual inspection of the plate. However, the magnitude of the reflected waveform shown in the Figure 6.42 slightly increases from the 12.7 J impact to the 17.9 J impact whereas the difference between the shapes of the impacted region is obvious.

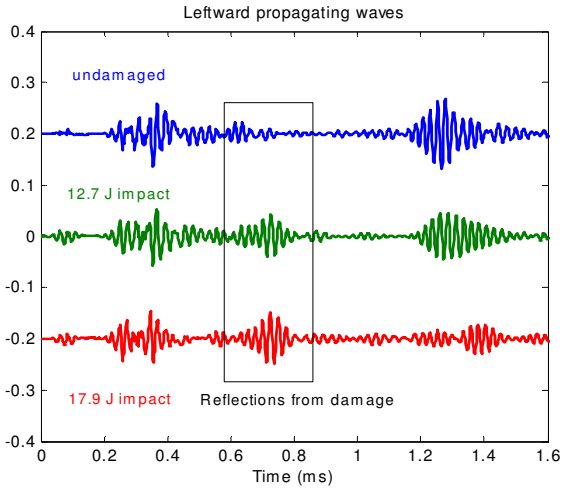

Figure 6.42: Leftward propagating waves – Impacted cases #2 and #3

From this observation, two theories can be assumed. The first one is that the Lamb wave is not able to track the increasing damage. The second one is that the structural properties of the plate have been equally affected by the impacts even though the visual inspection leads to different interpretations. A stronger impact analysis will confirm either of these assumptions. A mass of 10 lbs is adding to the hammer system and the swinging impactor is released at a 45° angle, producing a 23.1 J impact. The middle sensor response along with the leftward propagation are plotted in Figure 6.43

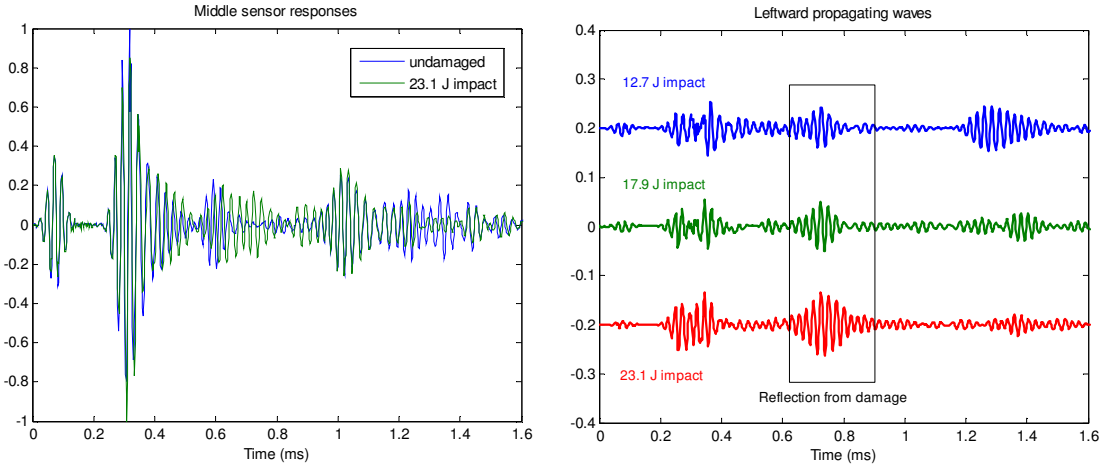

(a) Middle sensor responses

(b) Leftward propagation

Figure 6.43: Case #4 analysis

Both sensor signal and leftward propagating waves show that the magnitude of the damage reflection increases with the applied impact energy and thus with the size of the damage. The second assumption is therefore the right one. The reflections from the right edge also decay with the increasing energy impact. Before applying the Hilbert-Huang transform to these signals, several conclusions can be drawn from the transient analysis:

- The Lamb waves are able to detect damage in a composite plate that is invisible by the naked eyes.
- A composite structure can be seriously damaged without showing any physical signs on the surfaces.
- The physical marks of damage and the real loss in mechanical properties are not related.
- The amplitude of the reflection from damage increases with the impact energy and therefore with the size of the damage.

6.6.4 Hilbert-Huang spectrum and Energy metric

The empirical mode decomposition is then used to apply the Hilbert transform to the intrinsic mode functions extracted and to plot the time-frequency representation of the data. Once the Hilbert-Huang spectrum is obtained, the energy released by the damage can be quantified and linked to the impact energy and the size of the damage. The energy metric is applied to the unfiltered set of data. The Hilbert-Huang spectra for the unfiltered undamaged and damaged (12.7 J impact) are given in the Figure 6.44.

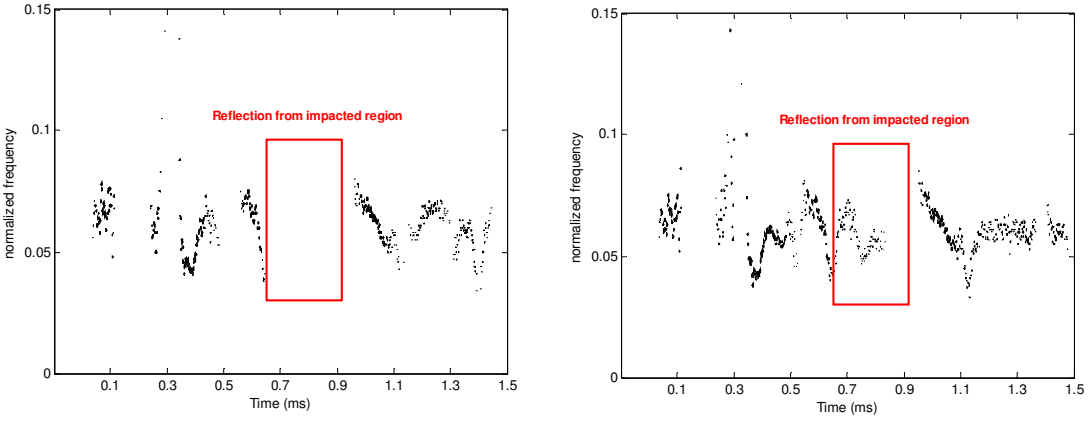

(a) Undamaged

(b) 12.7 J impact

Figure 6.44: Hilbert-Huang spectra – Unfiltered data

The results of the Hilbert energy measurement of the reflected frequency band are given in the Table 6.7.

Potential energy	0	3.3	12.7	17.9	23.1
Released energy	0.0182	0.1172	0.4946	1.1773	2.8956

Table 6.7: Energy metric results for the unfiltered data

Assuming that each impact weakens the plate and contributes to the creation of damage in the next impact, a cumulative energy impact approach seems to be more representative of the effective energy involved in damaging the plate. The energy metric results can therefore be plotted to describe the growth of damage with respect to the energy impact, as seen in Figure 6.45.

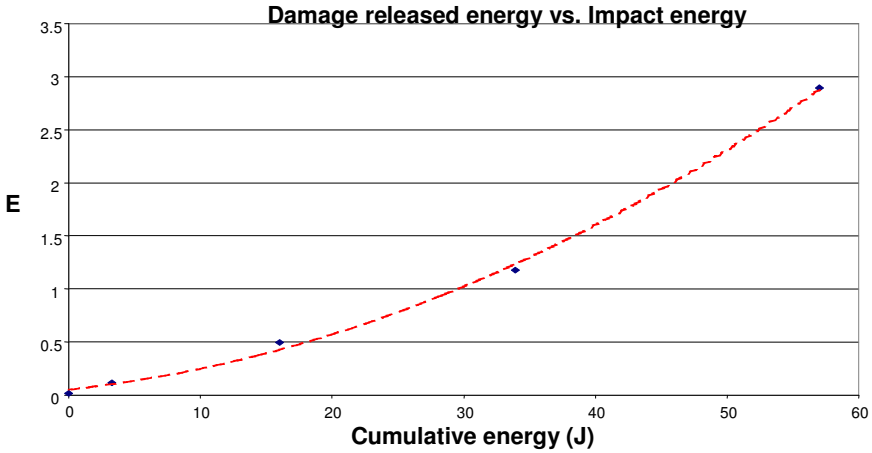

Figure 6.45: Growth of damage with impact energy

The energy released upon the damage growth perfectly fits a parabolic interpolation curve. In the case of the local mass loading experiment, the energy was shown to increase linearly with the size of damage. The track of increasing damage is therefore possible for this experiment through the energy released by the damage and using only one sensor.

6.6.5 Energy-time spectrum and the Phase shift metric

The energy-time spectrum aims to localize the damage through a precise determination of the time of flight and to quantify the size of the damage through the phase shift between the reflected waveforms. The energy-time spectrum for the low-velocity impact experiment described in the previous sections is given in the Figure 6.46. For a better visibility and readability, the results have been separated in two distinct plots.

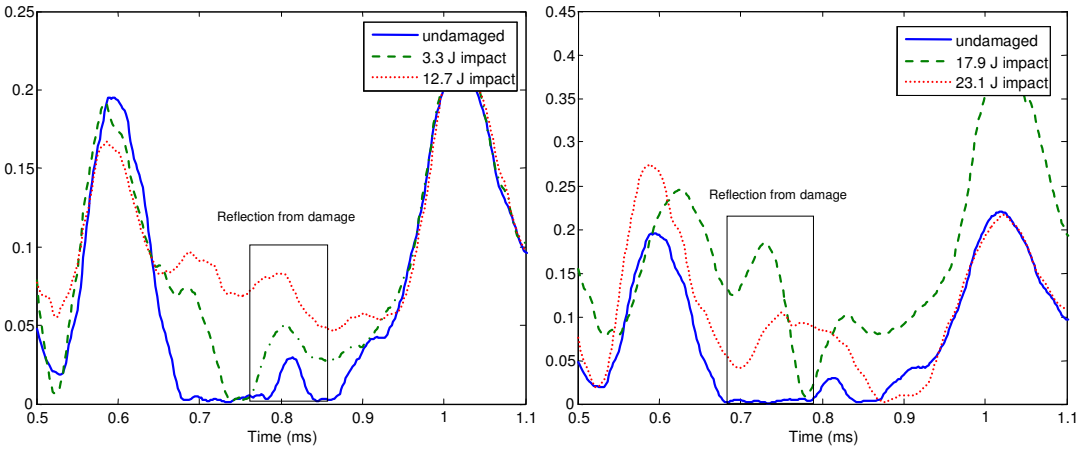

(a) Case #1 and #2 (b) Case #3 and #4

Figure 6.46: Energy-time spectra

As expected, the localization in time of the reflected waveform through the energy spectrum turns out to be very precise. A phase shift between the reflections from increasing damage can even be temporally quantified and related to the size of the damage. The amplitude of the reflected waveforms also increases with the energy impact. However, for the case #4 corresponding to the 23.1 J impact energy, the reflection is spread out in time, has a weaker magnitude and does not exhibit a clear peak. These characteristics can be explained by the fact that the addition of the 10 lbs mass to the system along with a large initial angle deviated the point of impact and

created a second damage in the plate. The reflected waveform represented in the energy spectrum therefore encloses two adjacent reflections. This assumption is confirmed by the picture of the impacted region in the Figure 6.47 that shows two damages in the plate.

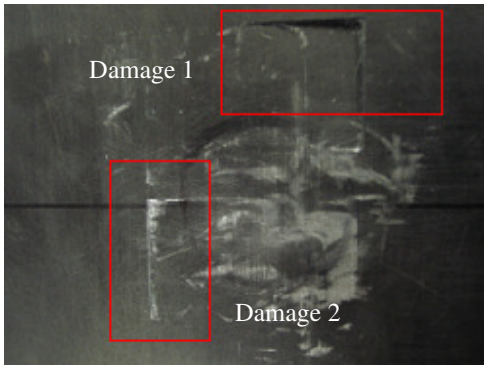

Figure 6.47: Front surface picture – Case #4

Using the group wave velocity and the time of flight given by the energy spectrum, the location of the damage can be inferred in the same way than for the previous experiments. In this case, we obtain the same results as for the local mass loading experiment of the Section 6.5.

In order to confirm the plate has effectively been damaged by the impact, a cross-section cut along the damage is realized. As we can see on the picture of the Figure 6.48, the different impacts created matrix crackings, broken fibers and a delamination.

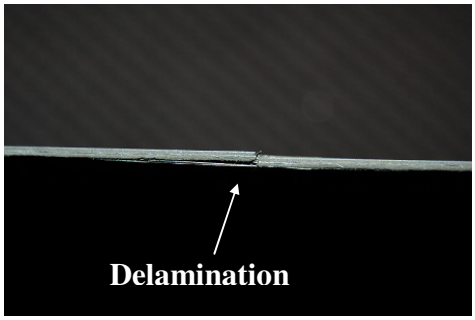

Figure 6.48: Cross-section picture of the impacted region

6.6.6 The Hilbert phase

So far, the Hilbert phase turned out to be the most promising feature for delamination detection in composite structures using the HHT but also the most sensitive and difficult to apply. This real world type of experiment aspires to confirm the capability of the Hilbert phase to describe the changes in the wave propagation speed energy. The Hilbert phase results are plotted in the Figure 6.49.

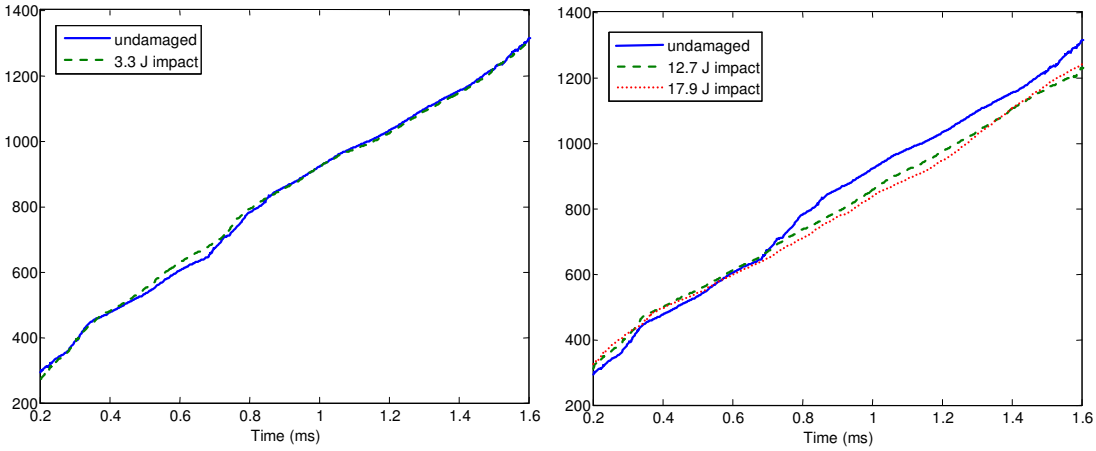

(a) Case #1

(b) Case #2 and #3

Figure 6.49: Hilbert phase plots

For the case #1, the transient analysis and the wavenumber filtering technique did not reveal the presence of damage even though the energy measurement showed a slight increase. The Hilbert phase confirms theses results. The phases for the undamaged case and the 3.3 J impact behave the same way, indicating that there is no discontinuity encountered by the wave. In the case of damage, the wave propagation is altered and results in a slope change in the Hilbert phase. The Hilbert phase of the cases #2 and #3 show these deviations. At around 0.7 ms, the undamaged and damaged phases start to diverge denoting the presence of damage in the composite

plate as seen in the Figure 6.49. The location of damage can be inferred from the time divergence and the amount of damage can be quantified by the mean phase error metric. The behaviors of both impacted phases are pretty close even if the 17.9 J impact appears to damage more the plate than the 12.7 J impact. The Hilbert phase is therefore consistent with all the previous conclusions and can perfectly describe the wave propagation and interaction with damage in the composite plate.

6.7 Summary

The CLPT theory was presented to model the dynamics of the composite plate. From the CLPT formulation, the wavenumber-frequency relationships were determined and computed for a symmetric layup $[90/0/0/90]_{8s}$. This theory was used to determine the wave group velocity of the A0 mode used to excite the structure. The most common encountered types of damage in composite structures were tested through a set of three experiments. The HHT as a damage detection tool was then used to process the data and to infer the presence of delamination and/or impact damage. The seeded delamination simulated by a Teflon patch and introduced between two adjacent plies was successfully detected by the Hilbert phase. The Hilbert phase accurately described the change in energy speed due to the delamination. Local mass loading was best identified by the Hilbert-Huang spectrum. The energy density of the reflection from the extra mass mounted on the plate increased with the size of the masses. A real world study case was then presented. A low-velocity impact experiment based on a swinging pendulum mechanism was setup. The data was processed with the EMD algorithm and the Hilbert spectra analysis. The damage detection schemes could detect and locate a damage that was not visible in the visual

inspection. The HHT was also shown to track increasing damage with increasing energy impact.

Chapter 7

Conclusion

7.1 Contributions

This chapter presents a summary of the important results and conclusions that can be drawn from this study. This thesis investigates a damage detection approach using wave propagation in thin plates and the Hilbert-Huang transform as a signal-processing tool. The study has focused on developing and validating damage detection schemes based on the features of the empirical mode decomposition and the associated Hilbert spectral analysis. Three damage detection techniques were developed based on the energy density, the time of flight and the energy speed propagation. The study was conducted for both isotropic and composite thin plates. For thin plates, wave propagation is described in terms of Lamb waves. The symmetric fundamental in-plane wave mode S0 was used for detecting damage in isotropic plates whereas the anti-symmetric fundamental transverse wave mode A0 was privileged to describe the damage interactions in composite plates. Two types of damage were investigated, impact damage and seeded delamination, for composite plates. Damage in the form of hole was examined in aluminum plate. The details of the major contributions resulting from this work are presented below:

2. The Hilbert-Huang transform was first implemented in Matlab 7.0. This method consisted in two parts in analyzing a given time series data. The first part is the empirical mode decomposition, which decomposes any

given signal into a set of simply oscillatory functions, defined as intrinsic mode functions. The IMF components were obtained by a sifting process algorithm. The second part of the implementation was the definition of the time dependent amplitudes and frequencies of the empirical modes using a Hilbert transform. The final result was represented by an energy-time-frequency representation, referred as the Hilbert-Huang spectrum.

3. The instantaneous phase can be used as a damage detection tool. A finite element model of a rod was used to show the effect of a stiffness loss on the phase behavior. The principle is that any damage in a structure alters the speed at which the energy traverses the structure. The phase reflects this speed change by a slope deviation. As a result, the Hilbert phase can not only detect the presence of the defect in the structure but also quantify the extent of the damage.
4. The Hilbert-Huang spectrum described the energy propagation in the structure. Any reflection is measurable by its energy density. The energy released upon defect growth can be therefore quantified and use to track the increasing damage. A larger reflection due to a larger damage will result in an increase of the energy in the Hilbert energy spectrum.
5. The time of flight between the actuation waveform and a damage reflection can be accurately extracted from the energy-time spectrum provided by the HHT. The peaks on the energy-time spectrum for the IMF component containing the highest energy give the wave arrival times of interest. The wave group velocity combined with the time of flight locate

the damage. If the initial shape and size of the damage is known, basic geometric considerations associated with time of flight and wave propagation characteristics provide a means to estimate the severity of the damage.

6. In a pulse-echo damage detection application, a piezoceramic actuator is used to actively interrogate a thin aluminum plate with damage in the form of a hole. The actuator sends out a transient interrogating excitation signal that is reflected from the damaged region. The response signals are gathered by the sensor array. The empirical mode decomposition was applied to the transient response signals and the reflection from the hole was revealed. Along with the knowledge of the wave propagation velocities, the location of the damaged could be placed. The energy of the reflected frequency band was used to quantify the size of the hole through the Hilbert energy spectrum. The prediction of the size of a hole was shown to be pretty accurate
7. The wavenumber filtering technique was used to separate the response of a delaminated composite laminate into a leftward and a rightward components. A reflection from the delamination, first invisible in the transient signals, showed up. Though weak, the reflection increased with the size of the delamination.
8. The reflection from the delamination also appeared in the second IMF after the decomposition of the transient signal. The empirical mode

decomposition was therefore able to extract weak reflections embedded in noise and other boundaries reflections.

9. The Hilbert phase turned out to be very efficient for delamination detecting in composite plates. The change in wave propagation speed due to the delamination was perfectly described by the phase behavior. The phase reacted by a slope deviation to the discontinuity. The time needed for the wave to pass trough the delamination gave the time span of the deviation.
10. Local mass loading was experimented on a cross-ply laminate in bonding masses on the plate surface. The wave experienced reflection from the mass. The reflection was visible in the transient signals. The extent of the artificial damage could be quantified with the energy release in the structure and by the time shift between reflections.
11. A low-velocity impact was successfully experimented and tested. The repetitive impact system allowed a correlation of the visual inspection of the impacted region with the potential energy and the HHT results. Invisible damage to the naked eyes was detecting in the leftward propagating waves as well as in the middle sensor responses. The energy-time spectrum could locate the damage whereas the energy density spectrum was used to quantify the damage. The increasing damage was shown to follow a parabolic trend. The Hilbert phase also gave consistent results with the other damage detection techniques and was able to detect and quantify the amount of damage created by the pendulum impactor

mechanism. This real world application showed all the Hilbert-Huang transform potential as a damage detection tool.

7.2 Limitations of Current Methods

Though the HHT appears to have a great potential for structural health monitoring purposes, there are certain issues which need to be addressed that could extend its use. A few of the limitations of the HHT and the damage detection methods developed are illustrated:

1. Concerning the empirical mode decomposition, some issues encountered during its implementation could be improved. The spline fitting influences a lot the decomposition. Overshoot and undershoot happen many times during the sifting process and corrupt the decomposition. The starting and ending points play a fundamental role in the extracting IMFs as well. An optimal windowing of the data must be found in order to avoid end effects and other types of unwanted behaviors. The stop criterion of the sifting process is also problematic. A good compromise between a too stringent and a too lax criterion must be found. All these implementation issues influence the quality of the decomposition and can be improved. Last but not least, the HHT is an empirical method. A mathematical formulation of the decomposition would probably help to resolve the problems enumerated above.
2. The Hilbert phase have sown some limitations for the local mass loading study case. The sensitivity of the phase to the structural elements limits its efficiency. Despite the outstanding results obtained for the delamination

case, a deeper investigation of the different parameters that influence the phase would allow a better understanding of this unique feature. The bonding conditions in the experiment may also have corrupted the phase behavior.

3. Damage detection techniques considered in this research were developed for damage oriented along the array axis. Non-axis damage detection has been inspected. The empirical mode decomposition was able to detect the presence of the damage. However, the different damage detection schemes did not provide a way to infer the location of the damage.

7.3 Recommendations for Future Work

The current study has tried to develop a new methodology in the field of signal processing for damage detection. In order to extend the use of the Hilbert-Huang Transform for practical implementation into an SHM system, there are several advancements in the current state of the art that need to take place. The most immediate are discussed as follows:

1. Improved wave propagation modeling of an anisotropic composite plate in order to get a better understanding of the way the waves propagate in the medium. A triangularization technique would then be possible and non-axis damage detection would be achievable with only three sensors, using the HHT.

2. Evaluated the ability of the damage detection techniques to detect multiple damages. This would enable to confirm the HHT as a potential damage detection tool.
3. Developed numerical simulations to confront with experimental results obtained in this work. A Reissner-Mindlin type of model would allow an accurate representation of the plate dynamics at high frequencies where transverse shear play a significant role.
4. Use of a C-scan system to qualitatively measure the amount of damage created by the impact of the swinging pendulum system. This would give a more physical interpretation to the HHT results.
5. Modified the actual empirical mode decomposition algorithm to obtain a spatial decomposition in terms of wavenumbers. Each IMF would correspond to a wavenumber present in the signal. As a result, the wave propagation would be entirely described and decomposed by the different mode functions. Each wavenumber present in the signal would be extracted with its occurring time. The spatial EMD would act as an adaptive wavenumber filter.

Bibliography

[1] Zumpano, G., Viscardi, M., and Lecce, L., "Structural Damage Analysis on a Typical Aeronautical Structure Using Piezoelectric devices", *42nd AIAA/ASME/ASCE/AHS/ASC Structures, Structural Dynamics, and Materials Conference and Exhibit*, Seattle, Washington, April 2001

[2] Staszewski, W., "Advanced data pre-processing for damage identification based on pattern recognition", *International Journal of Systems Science*, Vol. 31, No. 11, 2000, pp. 1381-1396.

[3] Speckmann, H. and Daniel, J.P., "Structural Health Monitoring for Airliner, from research to user requirements, a European view", *Conference on Micro-Nano-Technologies*, Monterey, California, November 2004.

[4] Speckmann, H. and Henrich, R., "Structural Health Monitoring (SHM) – Overview on Technologies under Development", *World Conference on NDT*, Montreal, Canada, September 2004.

[5] Steinke, S. and Grunder, M., "Airbus A380 construction advances", *Flug Revue* , November 2003, available online at http://www.flug-revue.rotor.com/FRheft/FRH0311/FR0311b.htm

[6] Staszewski, W., Boller, C., and Tomlinson, G., *Health Monitoring of Aerospace Structures*, John Wiley & Sons, 2004.

[7] Worden, K., Staszewski, W., and Tomlinson, G., "Smart systems – the role of signal processing", *Proceedings of CEAS, International Forum on Aeroelasticity and Structural Dynamics*, Rome, Italy, July 1997.

[8] Fourier, J., *Theorie Analytique de la Chaleur*, 1822.

[9] Melhem, H. and Kim, H., "Damage Detection in Concrete by Fourier and Wavelet Analyses", *Journal of Engineering Mechanics*, May 2003, pp. 571-577.

[10] Nag, A., Roy, D., and Gopalakrishnan, S., "Identification of Delamination in a Composite Beam Using a Damaged Spectral Element", *Structural Health Monitoring*, 2002, Vol. 1, pp. 105-126.

[11] Lee, B.C., and Staszewski, W., "Modelling of Lamb waves for damage detection in metallic structures Part II. Wave interactions with damage", *Smart Materials and Structures* 12, 2003, pp. 815-824.

[12] Loewke, K., Meyer, D., Starr, A., and Nemat-Nasser, S., "Structural Health Monitoring of Composite Materials Using the Two Dimensional Fast Fourier transform", submitted to: *Smart Materials and Structures*

[13] Alleyne, D. N. and Cawley, P., "The measurement and prediction of lamb wave interaction with defects", *Ultrasonics Symposium,* pp. 855–857, 1991.

[14] Debnath, L., Wavelet Transforms and Their Applications, Birkhauser, 2002

[15] Ihn, J., and Chang, F., "Detection and monitoring of hidden fatigue crack growth using a built-in piezoelectric sensor/actuator network: I. Diagnostics", *Smart Materials and Structures* 13, 2004, pp. 609-620.

[16] Valle, C., and Littles, J., "Flaw localization using the reassigned spectrogram on laser-generated and detected Lamb modes", *Ultrasonics* 39, 2002, pp. 535-542.

[17] Kim, I., Lee, H., and Kim, J., "Impact Damage Detection in Composite Laminates Using PVDF and PZT Sensor Signals", *Journal of Intelligent Material Systems and Structures*, Vol. 16, November/December 2005.

[18] Wait, J., Park, G., Sohn, H., and Farrar, C., "An Integrated Active Sensing System for Damage Identification and Prognosis", *Structural Dynamics and Materials Conference, Palm Springs*, California, April 2004.

[19] Paget, C., Grondel, S., Levin, K., and Delebarre, C., "Damage assessment in composites by Lamb waves and wavelet coefficients", *Smart Materials and Structures* 12, 2003, pp. 393-402.

[20] Kessler, S., Spearing, S., and Soutis, C., "Damage detection in composite materials using Lamb wave methods", *Smart Materials and Structures* 11, 2002, pp. 269-278.

[21 Kim, H., and Melhem, H., "Damage detection of structures by wavelet analysis", *Engineering Structures* 26, 2004, pp. 347-362.

[22] Lemistre, M., Gouyon, R., Kaczmarek, H. and Balageas, D., "Damage Localization in Composite Plates Using Wavelet Transform Processing on Lamb Wave Signals", *2nd International Workshop on Structural Health Monitoring*, Stanford, California, September 1999.

[23] Ip, K., and Mai, Y., "Delamination detection in smart composite beams using Lamb waves", *Smart Materials and Structures* 13, 2004, pp. 544-551

[24] Salehian, A., Hou, Z., and Yuan, F.G., "Identification of location of a sudden damage in plates using wavelet approach", *16th ASCE Engineering Mechanics Conference*, Seattle, Washington, July 2003.

[25] M. Z. Silva, R. Gouyon, and F. Lepoutre, "Hidden corrosion detection in aircraft aluminum structures using laser ultrasonics and wavelet transform signal analysis," *Ultrasonics* 41, pp. 301–305, 2003.

[26] Quek, S., Wang, Q., Zhang, L., and Ong, K.H., "Practical issues in the detection of damage in beams using wavelets", *Smart Materials and Structures* 10, 2001, pp. 1009-1017.

[27] Okafor, A., and Dutta, A., "Structural damage detection in beams by wavelet transforms", *Smart Materials and Structures* 9, 2000, pp. 906-917.

[28] Sohn, H., Farrar, C., Hemez, F., Shunk, D., Stinemates, D., and Nadler, B., "A Review of Structural Health Monitoring Literature: 1996-2001", Los Alamos National Laboratory Report, 2003

[29] N. E. Huang, Z. Shen, S. R. Long, M. C. Wu, H. H. Shih, Q. Zheng, N.-C. Yen, C. C. Tung, and H. H. Liu, "The empirical mode decomposition and the Hilbert spectrum for nonlinear and non-stationary time series analysis", *Proceedings of R. Soc. Lond*. A 454, pp. 903–995, 1998.

[30] Lin, S., Yang, J., and Zhou, L., "Damage identification of a benchmark building for structural health monitoring", *Smart Materials and Structures* 14, 2005, pp. 162-169.

[31] Quek, S., Tua, P., and Wang, Q., "Detecting anomalies in beams and plate based on the Hilbert–Huang transform of real signals", *Smart Materials and Structures* 12, 2003, pp. 447-460.

[32] Tua, P., Quek, S., and Wang, Q., "Detection of cracks in plates using piezo-actuated Lamb waves", *Smart Materials and Structures* 13, 2004, pp. 643-660.

[33] Yang, L., Lei, Y., Lin, S., and Huang, N., "Hilbert-Huang Based Approach for Structural Damage detection", *Journal of Engineering Mechanics*, No. 1, January 2004.

[34] L. W. Salvino and D. J. Pines, "Structural damage detection using empirical mode decomposition and HHT", *Journal of Sound and Vibration* 294, January 2006, pp. 97-124.

[35] Jha, R., Xu, S., and Ahmadi, G., "Health Monitoring of a Multi-Level Structure Based on Empirical Mode Decomposition and Hilbert Spectral Analysis", *Fifth International Workshop on Structural Health Monitoring* (Editor: Fu-Kuo Chang), September 12–14, 2005, Stanford University, CA

[36] Bernal, D., and Gunes, B., "An Examination of Instantaneous Frequency as a Damage Detection Tool", 14th Engineering Mechanics Conference, Austin, Texas.

[37] Yu, D., Cheng, J., and Yang, Y., "Application of EMD method and Hilbert spectrum to the fault diagnosis of roller bearings", *Mechanical Systems and Signal Processing* 19, 2005, pp. 259-270.

[38] Quek, S., Tua, P., and Wang, Q., "Comparison of Hilbert-Huang, wavelet and Fourier transforms for selected applications", *Mini-Symp. On Hilbert-Huang Transform in Engineering Applications*, Newark, November, 2003.

[39] Purekar, A.S., *Piezoelectric phased array acousto-ultrasonic interrogation of damage in thin plates*. PhD thesis, University of Maryland, Department of Aerospace Engineering, 2006.

[40] Purekar, A.S., Pines, D.J., Sundararaman, S., and Adams, D.E, "Directionnal piezoelectric phased array filters for detecting damage in isotropic plates", *Smart Materials and Structures* 13, 2004, pp. 838-850.

[41] Ville, J., "Theorie et applications de la notion de signal analytique", Cables et Transmissions, vol. 2A, 1948, pp. 61-74.

[42] Abbate, A., DeCusatis, C. M., and Das, P. K., *Wavelets and Subbands Fundamentals and Applications*, Birkhauser, 2002

[43] Matlab Help

[44] Bendat, J., and Piersol, A., *Random Data*, Wiley Series in Probability and Statistics, 2000.

[45] Cohen, L., "Time-frequency distributions - A Review", *Proceedings of the IEEE*, vol. 77, no. 7, pp. 941-981, 1989.

[46] Boashash, B., "Estimating and interpreting the instantaneous frequency of a signal - Part 1: Fundamentals", *Proceedings of the IEEE*, vol. 80, no. 4, pp. 520-537, 1992

[47] Cohen, L., *Time-frequency analysis*, Englewood Cliffs, NJ: Prentice-Hall.

[48] Gabor, D., "Theory of communication", *Proceedings of the IEEE,* vol. 93, pp. 429-457, 1946

[49] Rilling, G., Flandrin, P., and Goncalves,P., "On Empirical Mode Decompoistion and its Algorithms".

[50] Blakely, C. D., "A Fast Empirical Mode Decomposition Technique For Nonstationary Nonlinear Time Series", Preprint submitted to Elsevier Science, October, 2005

[51] Rytter, A., *Vibration based inspection of civil engineering structure,* Ph.D. dissertation, Department of Building Technology and Structural Engineering, 1993, Aalborg University, Denmark.

[52] Jha, R., Cross, K., Janoyan, K., Sazonov, E., Fuchs, M., and Krishnamurthy, V., "Experimental evaluation of instantaneous phase based index for structural health monitoring", *Proceedings of SPIE 6173, Smart Structures and Integrated Systems*, April, 2006.

[53] Graff, K. F., *Wave Motion In Elastic Solids*, Dover Publications, Inc., New York, 1975.

[54] Website http://www.glenbrook.k12.il.us/gbssci/phys/CLass/waves/u10l2c.html

[55] Alleyne, D. N., and Cawley, P., "The interaction of Lamb waves with defects", *IEEE Trans. Ultrason. Ferroelectr. Freq. Control* 39, 1992, pp. 381–97.

[56] Giurgiutiu, V., Bao, J., and Zhao, W., "Piezoelectric wafer active sensor embedded ultrasonics in beams and plates," *Experimental Mechanics* 43(4), 2003, pp. 428–449.

[57] Viktorov, I., *Rayleigh and Lamb Waves: Physical Theory and Applications,* New York: Plenum, 1967.

[58] Achenbach, J.D., *Wave Propagation in Elastic Solids*, North-Holland, New York, 1984.

[59] Chang, Z., and Mal, A., "Scattering of Lamb waves from a rivet hole with edge cracks" *Mech. Mater.* 21, 1999, pp. 197–204.

[60] Wang, C. S., and Chang, F.K., "Built-in diagnostics for impact damage identification of composite structures", *Proc. 3rd Int. Workshop on Structural Health Monitoring*, Stanford, California, 1999, pp. 612–621.

[61] Jones, R. M., *Mechanics of Composite Materials*, Hemisphere Publishing Company, New York, 1987.

[62] Hayashi, T., and Kawashima, K., "Multiple reflections of Lamb waves at a delamination", *Ultrasonics* 40, 2002, pp. 193-197.

[63] Berlincourt, D., Krueger, H. H. A. , and Near, C.,"Properties of piezoelectricity ceramics," Tech. Rep. TP-226, Morgan Electro Ceramics.

[64] Measurement Specialities, Inc., Sensor Products Division, 960 Forge Avenue, Norristown, PA 19403, Piezo Film Sensors Technical Manual.

.